INTERACTION BETWEEN THE FUNDAMENTAL TORSIONAL GUIDED WAVE MODE AND COMPLEX DEFECTS IN PIPES

by

Rosalba Carandente

A thesis submitted to Imperial College London for the degree of

Doctor of Philosophy

Department of Mechanical Engineering

Imperial College London

London SW7 2AZ

October 2011

Ai Miei Genitori

Declaration of originality

The material presented in the thesis "Interaction Between the fundamental torsional guided wave mode and complex defects in pipes" is entirely the result of my own independent research under the supervision of Professor Peter Cawley. All published or unpublished material used in this thesis has been given full acknowledgement.

Name: Rosalba Carandente   11/10/2011

Signed:

"The larger the island of knowledge, the longer the shoreline of mystery. "

Mary B. Yates

Abstract

The presence of defects in pipelines is a concern especially in petrochemical applications where the service integrity of pipes is a fundamental requirement to avoid process interruptions and to fulfil safety standards. Guided wave inspection is now routinely used in industry for screening long lengths of pipe for corrosion, any suspect areas then being followed up with conventional ultrasonic thickness gauging. However, this is difficult in cases where the suspect area is inaccessible (e.g. buried pipelines or pipes passing though walls), so it would be very useful to apply guided wave techniques for sizing as well as the detection and location of defects. This target is challenging due to the complexity of the profiles encountered in practice.

The present work aims to improve the understanding of the scattering of the fundamental torsional mode T(0, 1) from complex shaped discontinuities and to determine the controlling parameters of this phenomenon. The overall analysis starts with a study of the reflection from axi-symmetric tapered steps and notches in pipes. After that the scattering from three dimensional (3D) defects with different shapes has been studied. Firstly, flat-bottomed defects with different surface profiles have been analyzed, and then the study of the reflection behavior from 3D defects with varying depth profile has been carried out. All of the work presented here uses the T(0,1) mode for inspection.

It is revealed that the reflection coefficient maxima from axi-symmetric tapered defects decrease with increasing frequency as the slope of the taper becomes more gradual, this effect being more pronounced when the ratio of the average defect length to the wavelength increases. Tapered defects are therefore expected to be more difficult to detect at higher inspection frequencies; this effect is more evident for shallower tapers. It is also found that at a given maximum depth of a finite discontinuity, the peak of the reflection coefficient from a defect is linearly dependent on the circumferential extent of the defect, and is independent of its shape. The results from these analyses have been used to propose a practical approach to determine the maximum depth of a complex discontinuity from the reflection coefficient

behavior, provided that the external circumferential extent of the defect is known. This method has been applied to real corrosion patches and the results validated with experiments. Its main limitation is on defects with a gradual corrosion section profile, but with a sudden change of the depth over a small circumferential region. It is shown then that a possible way to diagnose sharp circumferential profile changes is to measure the reflection coefficient spectrum at frequency higher than usually used in long range guided wave inspection.

Acknowledgements

I would like to express my deepest gratitude to Prof. Peter Cawley for his great supervision and constant support. His ability to choose a course of action by considering the bigger picture of a problem has been an incredible lesson that I will carry throughout my future professional and personal life. I am grateful to Dr Jian Ma (Ken) for his valuable advices and support that was needed to get started with my research. Credit goes also to Prof. Mike Lowe and Dr. Francesco Simonetti for creating a stimulating and fruitful research environment in the Non-Destructive Testing Group.

Most of the analysis on complex defects would have not been done in a such productive and enjoyable way without the daily collaboration by skype with Dr. Løvstad, a friend and inspiring colleague from the Norwegian University of Science and Technology.

I would also like to thank all the present and past members of the NDT group, which have been not only inspiring scientists but also great traveling companions on our worldwide conference adventures and thanks also for having make me feel like a "queen" in a mostly male-lab.

Many thanks to Mr. David Tomlin and to Mr. Guljar Singh of the Mechanical Engineering workshop for timely and flawless help in keeping machining 'weird' defects in pipes. Also I would like to thank the people at Guided Ultrasonics Limited, especially Dr. Jimmy Fong without whom the experiments would have not been so successful. I would like also to acknowledge Mr. Harminder for having helped me to solve CAD issues and the project collaborators Prof. Wilcox and Dr. Moreau at the Bristol University NDT group.

All my gratitude goes to those who made me feel at home during this incredible scientific experience: Remino my acquired brother, for his invaluable support in every stage of this PhD. Andrea, a good partner for trips, ballet, opera and theatre nights, for his professional support and friendship. Michela, a great friend and

perfect shopping partner, for giving an unbreakable friendship. Sara, the metal rock manager, thanks especially for making me attend one concert of "the Doors". Alessandro for our deep speeches, Marchino for having always helped me to be in a party mood, and Tim for helping to improve my English in exchange of some deep knowledge of my Italian traditions. A special thanks goes also to all the other people made this "London experience" a great school of life.

None of this would have ever happened without the support and love of my big Italian family who have kept celebrating my visits every time. A huge thank you to Mami, Babbo, Polpi, Tetta, Nonne and to my older brother Michele, who keeps holding my hand throughout every experience of my life.

Contents

List of Figures

List of Tables

Chapter 1

Introduction

There is a considerable economic incentive to avoid unscheduled outages and to extend operation beyond the design lifetime of infrastructure systems such as refineries, power plants and pipelines. In particular, the interest is to avoid unscheduled outages because the failure of even a minor component can result in the complete shutdown of a facility. For example, the shutdown for 4 days of a pipeline carrying 630,000 barrels of oil per day in Alaska in January 2011 pushed the price of oil up by $4 a barrel [4], and an unscheduled shutdown of a 1,000-MW nuclear power plant may cost the operator between $1 million and $3 million per day [5]. Corrosion is a major cause of component failure and therefore its detection and control is a key issue in order to avoid unscheduled downtime in complex industrial systems. Guided ultrasonic wave techniques are employed worldwide to detect defects in different structures, especially in pipelines. Their main advantage is the capability to screen the entire structure over a range of up to 50 meters or more from a single location along the length of the inspected component [6]. The replacement of a corroded component is expensive so it is important to estimate whether the depth of the defect is sufficient to affect severely the integrity of the structure. Guided waves are usually applied for screening with only a rough estimate of the severity of the discontinuity; this procedure is to follow up with conventional local ultrasonic inspection. Typical guided wave instrumentation [7] applied to an overground pipeline is shown in Fig 1.1a. Unfortunately corrosion discontinuities often occur in
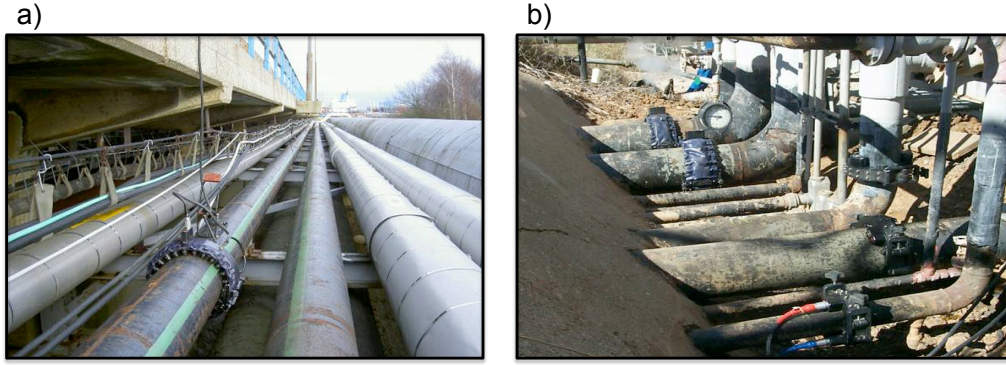
Figure 1.1: *Representation of guided waves equipment applied for screening a) overground pipelines b) buried pipes.*

areas of the structure that are not accessible (e.g. buried pipelines or pipes passing though walls); an example is shown in Fig. 1.1b. It then becomes very difficult to estimate the size of the detected defect, and especially its depth. The development of effective methodologies not only to define the location of the discontinuity but also to size the corrosion remotely is therefore crucial. The capacity of guided ultrasonic waves to size real corrosion defects remains challenging due to the complexity of the corrosion profiles encountered in practice. A deep understanding of the effect of different shape of defects on the incident ultrasonic wave is therefore required.

1.1 Forms of corrosion

As mentioned above, the complexity of the corrosion profiles encountered in practice makes more challenging the sizing of these discontinuities with guided ultrasonic waves. In the literature many scientists and engineers have recognized similarities in the forms the corrosion manifested in practice, therefore these types of discontinuities can be classified in specific groups by similarity of the mechanism of attack [8] or appearance of the corroded metal [9]. Other authors have discussed the more typical forms of corrosion related to specific metals and alloys [10, 11]. However, as with any classification system, the classification of these corrosion types is not distinct or all-inclusive since more than one mode of attack may occur.
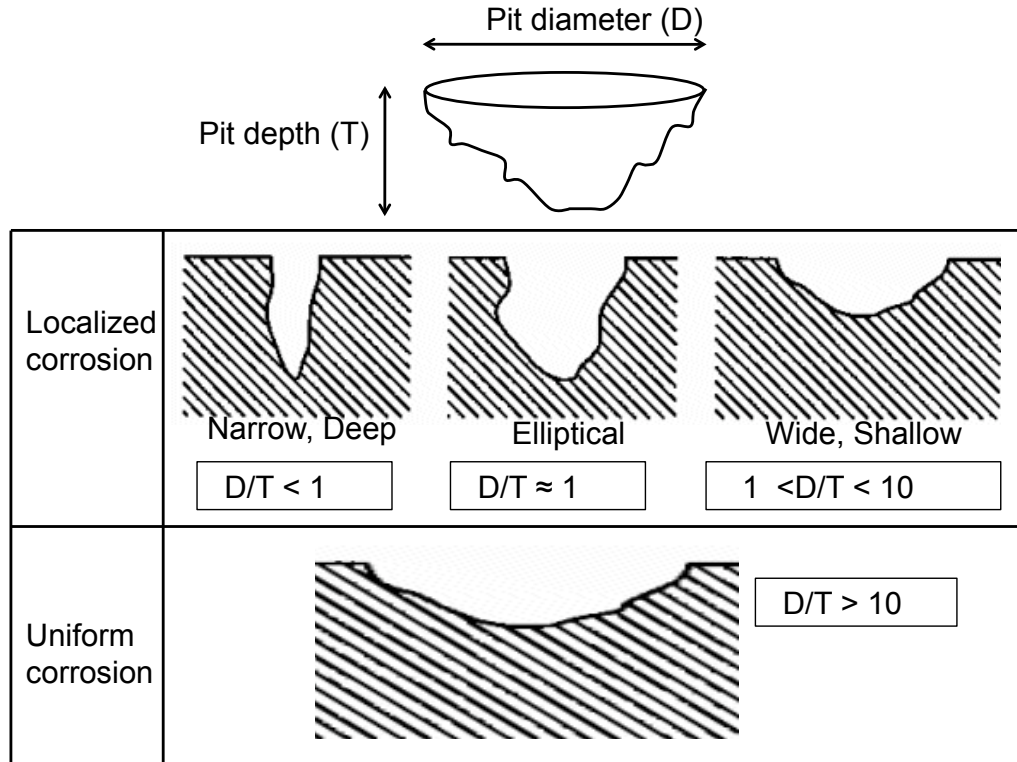
Figure 1.2: *Schematic of a general pit defect. The transition from the localized to uniform corrosion morphology is defined by the ratio of the pit diameter (D) and pit depth (T) [1].*

1.1.1 Morphology of corrosion

The morphology of corrosion defects can be divided in two big groups: general corrosion and localized corrosion. *General* (or uniform) *corrosion* occurs when an uniform thinning process proceeds without localized attack [8]. Copper alloys and weathering steels are typically subject to this kind of attack, whereas passive materials such as stainless steel and nickel-chromium alloys are generally attacked by localized corrosion. *Localized corrosion* happens when the corrosion damage is localized rather than spread uniformly over the exposed metal surface [8]. This means that instead of dealing with a slow, uniform loss of metal thickness the damage involves high rates of metal penetration at specific sites. These forms of attack are very dangerous since they can lead to premature failure of the structure caused by the rapid penetration with little overall weight loss.

Sometimes when pitting occurs on a freely accessible clean metal surface, a slight
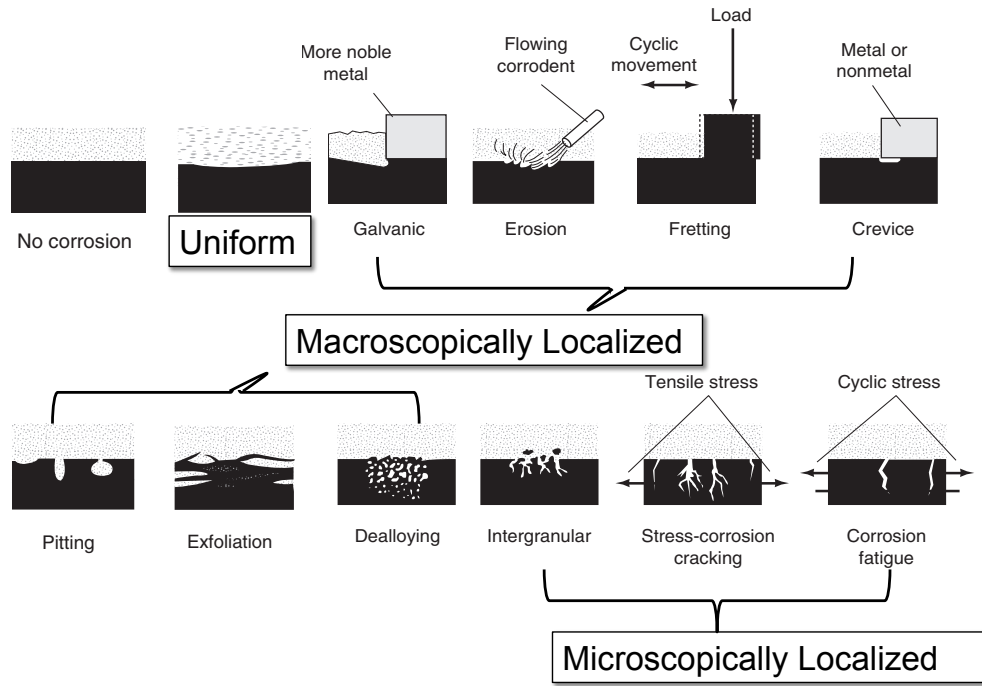
Figure 1.3: *Schematic of common forms of corrosions. Figure taken from [2]*

increase of the corrosivity of the environment will cause a more uniform corrosion. The physics behind the transition from highly localized attack to uniform corrosion is not clearly understood [8]. However, an empirical way to determine this transition based on the morphology for various pipe diameters and wall thickness was proposed in [1] and shown in Fig. 1.2. In this work a generic pit defect is defined by two parameters: the depth of the pit (T) and the diameter of the defect (D). It assumed that D is the axial extent of the defect as well as the extent along the circumferential direction. Uniform corrosion occurs when this ratio (D/T) is higher than 10. If not, localized corrosion happens and in particular:

a) $D/T < 1$. Localized pit is narrow and deep,

b) $D/T = 1$. Ellipsoidal shaped pit in the cross sectional direction,

c) $1 < D/T < 10$. Wider and shallower localized defect.

The most common forms of corrosion are clearly distinct as presented in [2] and shown Fig. 1.3. In this figure the difference between uniform corrosion profile and localized defect is shown. The localized corrosion defects are also classified in mi-

croscopic and macroscopic forms.

As mentioned above, the shape of a corrosion patch can be more complex than the ones just classified. In carbon steels and low-alloy steels in relatively mild corrodents, for example, pits are often generally distributed over the surface. If they blend together, the final result is a rough surface but generally uniform reduction in the cross section. If the pits do not blend together, the result is a rapid penetration of the metal at the sites of pits and little general corrosion. Little data are available on the real corrosion type defects; the availability of these data would have allowed a more precise statistical analysis and therefore a better understanding of the phenomenon. In this thesis, the focus is on corrosion profiles taken from pipes in operation which include both of these cases. Examples of corrosion patches are presented in the following section.

1.1.2 Examples of corrosion

The material of the structure and the environmental conditions are two fundamental parameters to take into account when discussing about corrosion. The corrosivity of a material cannot be described unless the environment in which the material is to be exposed is identified and *vice versa*. The general relationship between the rate of corrosion, the corrosion resistance of the material and the corrosivity of the environment is [2]

$$\frac{corrosivity\ of\ environment}{corrosion\ resistance\ of\ metal} = rate\ of\ corrosive\ attack \tag{1.1}$$

Usually in practice the acceptable rate of corrosion is fixed and the challenge is to choose the corrosion resistance of the metal and the corrosivity of the environment to be at or below the specific corrosion rate. Carbon steel pipelines are generally used in the petrochemical industry and are considered in this work. Carbon steels are by their nature of limited alloy content, usually less than 2% by weight for total of additives; this level of additives does not generally produce any significant changes in general corrosion behavior. The rate of corrosion of the material would change
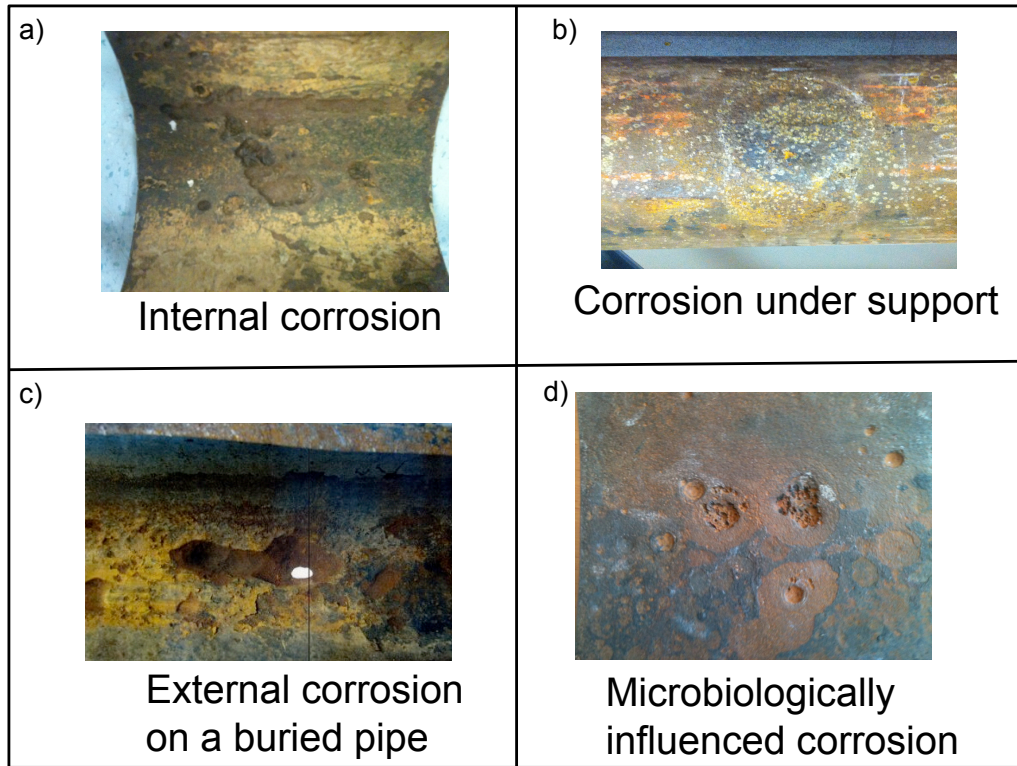
Figure 1.4: *Examples of real corrosion defects. a) internal corrosion; b) corrosion under support; c) corrosion on a buried pipe and d) microbiologically influenced corrosion.*

with small additions of copper, chromium, nickel, and phosphorus.

Corrosion of the pipe wall can occur either internally or externally. *Internal corrosion* occurs when corrosive liquids or condensates are transported through the pipelines. Depending on the nature of the corrosive liquid and the transport velocity, different forms of corrosion may occur, including uniform corrosion, pitting/crevice corrosion, and erosion-corrosion. Figure 1.4a shows an example of a generally uniform internal corrosion defect. A common type of external surface corrosion in pipelines happens at the interfaces with supports. The main causes of the initiation of *corrosion under support* are [12]:

1. Crevice Forming - caused mainly by the formation of a crevice at the pipe surface.
2. Water Trapping - caused by support types that allow water to be trapped and held in contact with the pipe surface.
3. Galvanic Couple Forming - caused by supports that may develop bi-metallic con-

tact. Even though both the pipe and support are steel, the metallurgical differences can still provide a small potential difference to drive a corrosion cell.

A uniform corrosion profile found under a support of an 8 inch schedule 40 pipe is shown in Fig. 1.4b. The defect profile is very gradual, its maximum depth reaching 60% of the thickness.

In *buried* pipelines several different modes of external corrosion have been identified. The primary mode of corrosion is a macro-cell form of localized corrosion due to the heterogeneous nature of soils, local damage of the external coatings, and/or the disbonding of external coatings. Fig. 1.4c shows an example of external corrosion on a buried 6 inch pipe taken from [1]. In the case of carbon steel buried pipes, the weight loss and maximum pit depth in soil corrosion are dependent on the time of exposure (t) as follows

$$Z = at^m, \tag{1.2}$$

where a and m are constants dependent on the specific soil corrosion situation and Z is either the weight of loss or the maximum pit depth.

Another factor that influences the growth rate of corrosion in pipelines is the presence of microorganisms, including bacteria and fungi. *Microbiologically influenced corrosion* (MIC) is therefore defined as corrosion that is influenced by the activities of these microorganisms. It has been estimated that 20 to 30% of all corrosion on pipelines is MIC-related [13]. Usually a growing microbiological colony accelerates the corrosion process by either: (1) reducing the effect of the corrosion products that should inhibit further corrosion, or (2) providing an additional reduction reaction that accelerates the corrosion process. An example of MIC attack on an external pipe surface is shown in Fig. 1.4d.

1.2 Literature background and motivation

A deep understanding of the effect of different shapes of defects on the incident guided waves is required in order to develop a method not only to be able to define the location of the defective area but also estimate its size remotely.

Many studies of the interaction of Lamb waves with discontinuities have been done in the past in plates with symmetric (S) and antisymmetric (A) waves [6, 14–23] and shear horizontal (SH) polarized waves [24–28]. The majority of the past work on plate structures has adopted a plane strain assumption in order to focus on part depth but infinite length defects [6, 14–25, 27, 28]; a plane stress assumption has been made by Rajagopal and Lowe [26] in order to understand the impact of the length of a finite defect on the interaction of an incident mode with the defect. Furthermore the scattering from 3D-circular holes has been analyzed with Lamb waves in [21–23]. In pipes the fundamental torsional mode T(0,1) and longitudinal L(0,1) and L(0,2) modes interacting with defects have been analyzed [29–47]. The reflection of cylindrically guided waves from axi-symmetric discontinuities, such as thickness changes, cracks and notches has been studied [29–32]. Much work has also focused on the scattering from 3D part-circumferential cracks and notches in pipes [32–47]. In these studies, the notches had simple flat-bottomed geometries; however, as discussed above, real corrosion defects normally have a much more gradual change of thickness, and therefore have a varying depth profile, which will affect the characteristics of the reflection. In the past little attention has been give to this problem. Zhu *at al* in 1998 [48] considered the effect of hidden corrosion on mode cut-off, group velocity and transmission and reflection amplitudes for the detection of thinning in structures with guided waves. They used a shallow half-ellipse model to simulate numerically the corrosion defect. Subsequent work of Zhu [32] presented a numerical analysis of the guided wave reflection from axi-symmetric and non axi-symmetric corrosion defects in hollow cylinders. The scattering of SH and Lamb modes from defects with an elliptical depth profile in plates was then analyzed by Zhao and Rose [27].

More recently there have been several theoretical [49], experimental and numerical [50–53] studies on the propagation of symmetric (S_0) and antisymmetric (A_0) Lamb waves in varying section waveguides. It has been observed that the local phase velocity of guided waves inside a varying thickness section is the same as in a waveguide of constant thickness, which is equal to the local thickness at the measurement point. This observation has been used for thickness determination in plate structures with a Gaussian variation of the section [50, 51] and in the presence of a linear variation of the thickness in a limited region [51–53]. These studies showed numerically and experimentally that when the excited Lamb mode is dispersive, its speed varies with the local thickness and thus gives information on the local thickness.

Lately, a few works started focusing on the reflection of guided waves from more complex defects. Ma and Cawley [54] analyzed the reflection from elliptical and circular 3D defects with linear variation of the depth through the thickness in plates. Further work looked at the scattering of bulk waves from multiple spherical and elliptical inomogenities [55–58]. Moreau *et al* [59] discussed of the scattering of guided waves from through-thickness cavities with irregular shapes and Løvstad and Cawley [60] analyzed the effect of the interaction of multiple flat-bottomed circular holes on the reflection coefficient in pipes in order to study the pitting corrosion. However real corrosion defects can have much more complex profiles which may affect the magnitude and frequency dependence of the reflection. The aim of this work is to analyze the effect of defects with more realistic shapes on the reflection coefficient (RC) in pipes. The target here is also to determine the main parameters that affect the reflection coefficient spectrum in order to define a practical method to size a corroded area remotely.

1.3 Thesis outline

This thesis follows the structure outlined below.

The second chapter presents a general introduction on guided ultrasonic waves. An overview of the theory of ultrasonic waves propagating in structures such as plates

and pipes is presented. Most emphasis is given to the propagation of SH waves in plate and torsional guided waves in pipes which are used in this work. The analogy between the propagation of guided waves in plates and pipes is highlighted and the choice of the mode and frequency range for practical inspection of pipelines is discussed.

A complex corrosion defect can be considered as a succession of tapered steps with different slopes and lengths. Therefore the third chapter of this work starts with the understanding of the nature of the fundamental torsional guided wave mode T(0, 1) scattering from axi-symmetric tapered up- and down- steps in pipes. The scattering characteristics of these tapers were then used to predict the reflection from tapered notches with different depths and varying slope angles. These numerical results have been validated by experiments. This preliminary analysis is limited to axi-symmetric defects and therefore addresses the effect of complex profile of the defect in the axial direction. The material of this Chapter is the basis of an article published in the Journal of the Acoustical Society of America ([P2] in the List of Publications).

Chapter 4 analyzes the effect of defects with more realistic depth and surface profiles on the reflection of the fundamental torsional mode T(0, 1) in pipes. A numerical study of the reflection of T(0, 1) from three dimensional (3D) defects in pipes with different shapes is carried out. Firstly, simple flat-bottomed defects with different surface profiles are analyzed, and then the reflection from 3D defects with varying depth profile is studied. The influence of the depth profile of a more complex defect in the axial and circumferential directions on the reflection coefficient is also analyzed. The results from the above analyses are then used to propose a practical approach to determine the maximum depth of a complex discontinuity from the reflection coefficient behaviour. This method is applied to real corrosion patches and the limitations of the method are determined. An experimental validation of the numerical simulations is presented in the last section of the chapter. The material of this Chapter is the basis of an article published to NDT&E International ([P4] in the List of Publications).

In Chapter 5 a discussion on an approach to diagnose the presence of a sharp change

in depth within a small region around the circumference of the pipe surrounded by a generally corroded area is presented. The idea is determine whether there is a correlation between the spatial components of a defect and the reflection coefficient spectrum from the defect itself. This study starts with the analysis of a 2D shaped defect decomposed with Fourier transform analysis. This decomposition approach in the spatial frequency domain is then applied to finite 3D defects: firstly ellipsoidal defect and then complex corrosion patches. The findings from the FE simulations are validated with test measurements in the last part of the chapter. The material of this Chapter are part of articles submitted to NDT&E International and to *Review of Progress in Quantitative NonDestructive Evaluation* in August 2011([P5] and [P6] in the List of Publications).

Finally, the main results of this work are summarized in Chapter 6 and suggestions for future work are given.

Chapter 2

Guided waves background

2.1 Introduction

Ultrasonic waves are an established technique for the inspection of structures. It is necessary to understand the way waves propagate in structures before proceeding to analyze more complex scattering phenomena. This chapter introduces the basic principles of ultrasonic wave propagation in media such as plates and pipes. Bulk waves refer to wave propagation in infinite structures (e.g. waves traveling inside the material) and are dependent only on the material properties. Only two kind of bulk waves can propagate (shear and longitudinal), their propagation being uncoupled and their velocity being constant with the frequency (non-dispersive). At the boundaries of the material the bulk waves interact with the boundaries and reflection, refraction and mode conversion between the shear and longitudinal waves occur. It is this interaction of the bulk wave with the boundaries that leads to the development of the guided waves which propagate at the boundaries (*Rayleigh* surface waves [61]) or between the boundaries (*Lamb* waves [62]). Guided waves are then dependent on the properties of the material and of the material boundaries. The solution of any guided wave problem requires the wave propagation equations (which are the same for bulk waves) and some physical boundary conditions to be satisfied. In practice the difficulty of using guided waves is due to the complexity

of the solution since there are an infinite number of modes associated with a given partial differential equation solution.

In this chapter, a brief description of the equations of motion in isotropic media is shown in the next section (sec. 2.2) followed by the analysis of guided wave propagation in stress-free plates (sec. 2.3) and hollow cylinders (sec. 2.4). Section 2.5 discusses the relationship between waves propagating in plates and pipes. A brief discussion on the choice of modes and frequency range used for practical inspection is presented in sec. 2.6. Section 2.7.1 then provides details of the finite element meshing and time stepping rules required to simulate guided wave propagation in pipes.

2.2 Equations of wave propagation in Isotropic media

As mentioned above bulk waves and guided waves are governed by the same set of partial differential equations, but guided waves require boundary conditions to solve the mathematical problem. Wave propagation in infinite elastic media is well-documented in literature e.g. [63–65] and is briefly summarized here.

Applying Newton's second law and the conservation of the mass within an arbitrary volume of an linearly elastic solid and neglecting any external body forces, Euler's equation of motion can be derived as

$$\rho \frac{\partial^2 \mathbf{u}}{\partial t^2} = \nabla \cdot \sigma \tag{2.1}$$

where ∇ is the vector operator $(\hat{x}\frac{\partial}{\partial x}, \hat{y}\frac{\partial}{\partial y}, \hat{z}\frac{\partial}{\partial z})$, $\mathbf{u}$ is the particle displacement vector in a material as a function of the time t and position vector $\mathbf{r}$. In addition, ρ is the constant density and σ is the stress tensor that can be expressed also in terms of the strain tensor ϵ using Hooke's law

$$\sigma = \mathbf{C} \cdot \epsilon \tag{2.2}$$

where **C** is the stiffness tensor with 21 possible components. In a isotropic, homogeneous, linear elastic material the theory of elasticity says that it is possible to reduce the components of the elastic stiffness tensor to two material constants (λ, μ) called Lam$\acute{e}$ constants [64]. Expressing the stress tensor in terms of displacements, Hooke's law becomes:

$$\sigma = \lambda \mathbf{I} \nabla \cdot \mathbf{u} + \mu(\nabla \mathbf{u} + \mathbf{u} \nabla^T) \tag{2.3}$$

where I is the identity matrix. Combining the equation 2.1 with 2.3 gives

$$\mu \nabla^2 \mathbf{u} + (\lambda + \mu) \nabla \nabla \cdot \mathbf{u} = \rho \frac{\partial^2 \mathbf{u}}{\partial t^2} \tag{2.4}$$

Equation 2.4 is Navier's differential equation of motion for an isotropic elastic medium. In this equation the symbol ∇^2 is the scalar operator ($\frac{\partial^2}{\partial x^2}, \frac{\partial^2}{\partial y^2}, \frac{\partial^2}{\partial z^2}$). The expansion of this vector equation in its three spatial components (x, y, z) gives a set of scalar linear equations, so the superposition of two or more valid solutions will still be a solution. This set of equations cannot be integrated directly so depending on the application an appropriate solution must be assumed [64].

Using the Helmotz decomposition, the displacement **u** can be split as

$$\mathbf{u} = \nabla \phi + \nabla \times \mathbf{\Psi} \tag{2.5}$$

where ϕ is a compressional scalar potential so the term $\nabla \phi$ is an irrotational component and Ψ is the vector potential. Therefore $\nabla \times \mathbf{\Psi}$ is a rotational component for which $\nabla \mathbf{\Psi} = 0$. The substitution of this expression for $\mathbf{u}(\mathbf{r}, t)$ into the Navier's equation 2.4 gives

$$\nabla[(\lambda + 2\mu)\nabla^2 \phi - \frac{\partial^2 \phi}{\partial t^2}] + \nabla \times [\mu \nabla^2 \mathbf{\Psi} - \rho \frac{\partial^2 \mathbf{\Psi}}{\partial t^2}] = 0. \tag{2.6}$$

This equation is satisfied if both terms in the square brackets are equal to zero. This means that the equation of motion can be separated into two different equations

where the two unknown variables are the two potentials

$$
\begin{aligned}
\frac{\partial^2 \phi}{\partial t^2} &= c_L^2 \nabla^2 \phi \\
\frac{\partial^2 \mathbf{\Psi}}{\partial t^2} &= c_S^2 \nabla^2 \mathbf{\Psi}
\end{aligned}
\tag{2.7}
$$

These equations are usually called Helmotz differential equations; the first one governs the longitudinal waves with phase velocity c_L, whereas the second one governs the shear waves with phase velocity c_S. These phase velocities are given by

$$
\begin{aligned}
c_L &= (\frac{\lambda + 2\mu}{\rho})^{1/2} \tag{2.8} \\
c_S &= (\frac{\mu}{\rho})^{1/2} \tag{2.9}
\end{aligned}
$$

The equations 2.7 are independent from each other this means that only two kind of waves can propagate in an unbounded isotropic medium without interaction. The general solutions for the propagation of the two waves are

$$
\begin{aligned}
\phi &= \phi_0 e^{i(\mathbf{k_L} \cdot \mathbf{z} - \omega t)} \tag{2.10} \\
\mathbf{\Psi} &= \mathbf{\Psi_0} e^{i(\mathbf{k_S} \cdot \mathbf{z} - \omega t)} \tag{2.11}
\end{aligned}
$$

where z is the spatial coordinate of the wave, t is the time variable, ϕ_0 and $\mathbf{\Psi_0}$ are arbitrary initial constants and $\mathbf{k_L}$ and $\mathbf{k_S}$ are respectively the longitudinal and shear wavenumber vectors given by

$$
\mathbf{k_{L,S}} = \frac{\omega}{c_{L,S}}
\tag{2.12}
$$

where ω is the angular frequency ($\omega = 2\pi f$).

2.3 Guided waves in unbounded stress-free plates

In this section the solutions of the unbounded stress-free plate case (shear horizontal and Lamb waves) are briefly detailed. The two most used methods of solution are
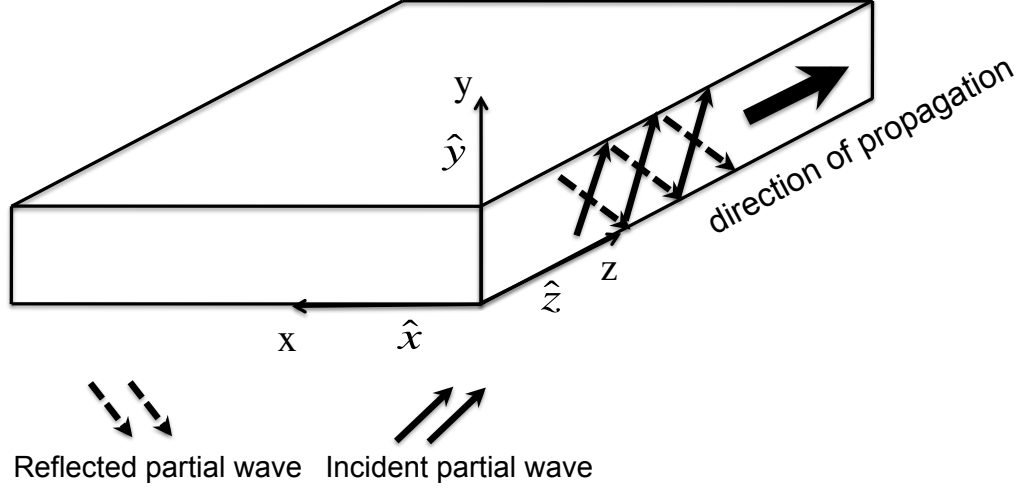
Figure 2.1: *Schematic of isotropic plate and its coordinate system. A scheme of its internal reflecting waves is also shown.*

the method of potentials (documented for example in [66]) and the partial wave technique [64, 67].

Fig. 2.1 shows the geometry of an isotropic plate of thickness t, $\hat{z}$ is direction of propagation of the waves and the planes at $y = 0, t$ are the traction free boundary surfaces. In order to solve a guided wave propagation problem we need to couple the equations with the physical boundary conditions. The method of potentials can be adopted to solve this problem [66] , which solves the equations 2.7 with ϕ and $\mathbf{\Psi}$ as unknown variables. If the particle displacement in the $\hat{y}$ direction ($\mathbf{u}_y$) is assumed equal to zero and only rotations around the y axis ($\mathbf{\Psi}_z = \mathbf{\Psi}_x = 0$) are allowed, the Helmotz differential equations are simplified as

$$\frac{\partial^2 \phi}{\partial t^2} = c_L\left(\frac{\partial^2 \phi}{\partial x^2} + \frac{\partial^2 \phi}{\partial z^2}\right) \tag{2.13}$$

$$\frac{\partial^2 \mathbf{\Psi}}{\partial t^2} = c_S\left(\frac{\partial^2 \mathbf{\Psi}}{\partial x^2} + \frac{\partial^2 \mathbf{\Psi}}{\partial z^2}\right) \tag{2.14}$$

The solution of these equations are the *Lamb* waves.

Whereas if the displacement component in the $\hat{x}$ and $\hat{z}$ directions are assumed equal to zero ($\mathbf{u}_x = \mathbf{u}_z = 0$) and considering the solution for which the scalar potential ϕ vanishes ($\phi = 0$) the equations 2.7 can be reduced to one vector equation in the

variable $\mathbf{\Psi}$,

$$\frac{\partial^2 \mathbf{\Psi}}{\partial t^2} = c_S(\frac{\partial^2 \mathbf{\Psi}}{\partial x^2}) \tag{2.15}$$

The waves that satisfy this equation are called Shear Horizontal (SH) waves. The particle motion of longitudinal waves is entirely in the direction of propagation and the wave motion consists of a change of volume (dilatation) only. The vibration of the SH waves is perpendicular to the direction of wave propagation and the motion consists of rotation if the medium without change of volume. Lamb waves are the combination of vertically polarised shear waves (SV) and longitudinal waves (P); these wave packets are coupled so they cannot exist individually. The solution is consequently more complex due to the nature of the waves. Their dispersion relations (which are the solutions to the modal wave propagation problem) are transcendental and in general need to be solved numerically. All the modes are dispersive (their velocity changing with the frequency). For a more detailed description of the properties of *Lamb* waves see [68] . A brief analysis of the SH wave propagation problem in a unbounded free plate is presented in the next subsection.

2.3.1   The solution for Shear Horizontal waves

The geometry of a plate shown in Fig. 2.1 is considered in this section. The general solution of the bulk wave propagation problem (see equation 2.11) is applied to SH waves traveling in plates, so a simple solution of the equation 2.15 can be obtained

$$\mathbf{\Psi} = \mathbf{\Psi}_0(y)e^{i(k_z z - \omega t)}; \tag{2.16}$$

where $\mathbf{\Psi}_0$ is the amplitude of the displacement, i is $\sqrt{-1}$ and k_z is the wavenumber in the direction of propagation $\hat{z}$, and ω is the circular frequency($\omega = 2\pi f$). Substituting this solution in the second equation of 2.7 yields an equation for the

unknown vector potential in terms of through-thickness sinusoids

$$\mathbf{\Psi}_0(0) = \mathbf{A}sin(k_y y) + \mathbf{B}cos(k_y y) \tag{2.17}$$

where k_y is the through-thickness wavenumber. This is related to the bulk shear wavenumber, k_S by

$$k_y^2 = k_S^2 + k_z^2 \tag{2.18}$$

$$k_S = \omega/c_S \tag{2.19}$$

where c_S is the shear velocity defined by equation 2.9. Hooke's law is used to express the stresses in terms of strain, then the strain-displacement relations are used to express the strain in terms of the unknown vector potential $\mathbf{\Psi}$. In this problem the boundary surfaces are considered traction free; therefore at the plane $y = 0, t$ the equation to be satisfied is

$$(\lambda + \mu)\frac{\partial u_x}{\partial y} = (\lambda + \mu)\frac{\partial}{\partial y}(\frac{\partial \Psi}{\partial y} + ik_z \Psi_y) = 0 \tag{2.20}$$

A full analysis of this is presented in [67].

The substituition of the potential 2.17 into the boundary equation 2.20 shows that this is satisfied if

$$k_y = \frac{l\pi}{t} \tag{2.21}$$

where l is an integer that can assume values from zero to infinity. The dispersion relation can then be obtained substituting this condition into the equation 2.18

$$k_z^2 = (\frac{\omega}{c_z})^2 = (\frac{l\pi}{t})^2 - (\frac{\omega}{c_S})^2. \tag{2.22}$$

This equation can be expressed in terms of phase velocity (c_p) and frequency-thickness product by knowing that $k_z = \omega/c_p$ like so

$$c_p(ft) = \pm 2c_s(\frac{ft}{\sqrt{4(ft)^2 - l^2 c_s^2}}). \tag{2.23}$$
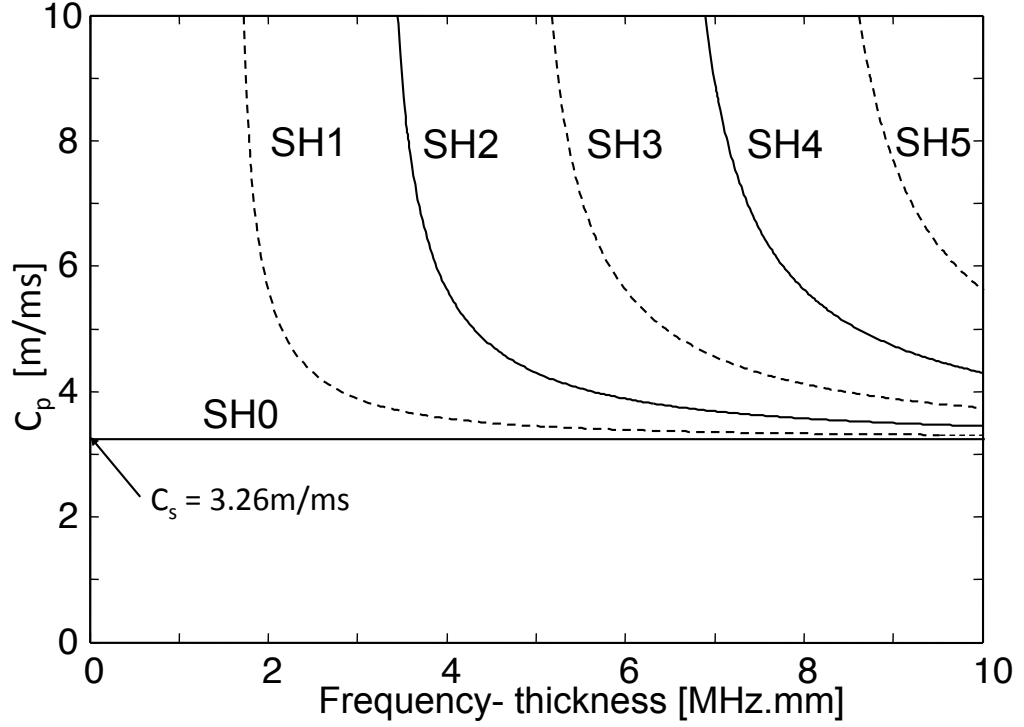
Figure 2.2: *Phase velocity dispersion curves for the SH modes in a steel plate ($c_s = 3260m/s$). Symmetric modes are plotted in solid lines and anti-symmetric modes in dotted lines.*

Fig. 2.2 shows the plot of the phase velocity and the frequency-thickness product for a steel plate ($c_s = 3260m/s$). These curves were calculated using the program Disperse, developed at Imperial College by Lowe and Pavlakovic [69,70]. In the figure are highlighted the first few SH modes present in a steel plate in a range of frequency-thickness from 0 to 10 MHz-mm. These modes are generated by using equation 2.23 varying the order of the integer l. The modes can be symmetric or antisymmetric and are represented in the figure by an even or odd counter respectively. For $l = 0$ the solution is the zeroth-order SH symmetric mode (SH_0) which is the only mode whose velocity $c_p = c_S$ and whose velocity does not change with the frequency (non-dispersive mode). For $l > 0$ the phase velocity varies with the frequency as it can be noted from Fig. 2.2; these modes are dispersive so the shape of a wave packet containing multiple frequencies is distorted as the wave propagates. All the modes showed in Fig. 2.2 converge to the value of the $c_p = c_s$ for high values of the frequency-thickness product. The SH modes exist at all frequencies (as expressed
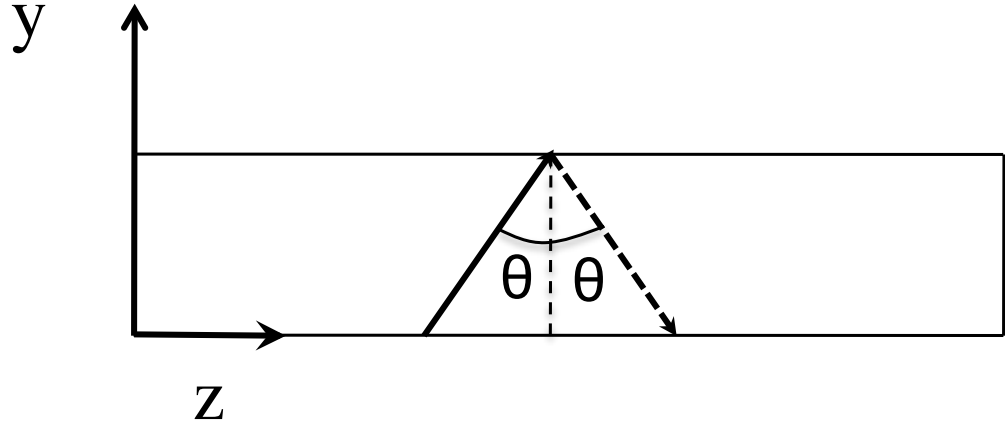
Figure 2.3: *Schematic of partial wave solution. Snell's law.*

by equation 2.23) but they propagate only at frequencies higher than their cut-off frequency, whose value can be calculated for the zero of the denominator of equation 2.23. The cut-off frequency-thickness product of the lth mode for example is

$$ft_l = \frac{lc_L}{2}. \tag{2.24}$$

At frequencies lower than the cut-off the mode has a non-propagating solution. The partial wave theory gives more physical information about this phenomenon [67]. This theory uses simple exponential waves in the form of the waves expressed by equation 2.16 that are reflected from the boundaries of the plate (up and down waves represented in Fig. 2.3). The solution to the free plate problem is therefore obtained by superposing the up and down waves. The reflection at the boundaries is governed by Snell's law [67]. At the cut off frequency the angle of incidence of the waves is equal to zero, so the wave just reflect back and forth across the thickness of the waveguide not causing any change of the stress and displacement field along the direction of propagation. The non-propagating modes are only a local disturbance so they do not carry any energy. The significance of the non-propagating modes in the reflection from discontinuities has been analyzed in [71].

Fig. 2.4 represent the group velocity (c_g) dispersion curves for the steel plate. The
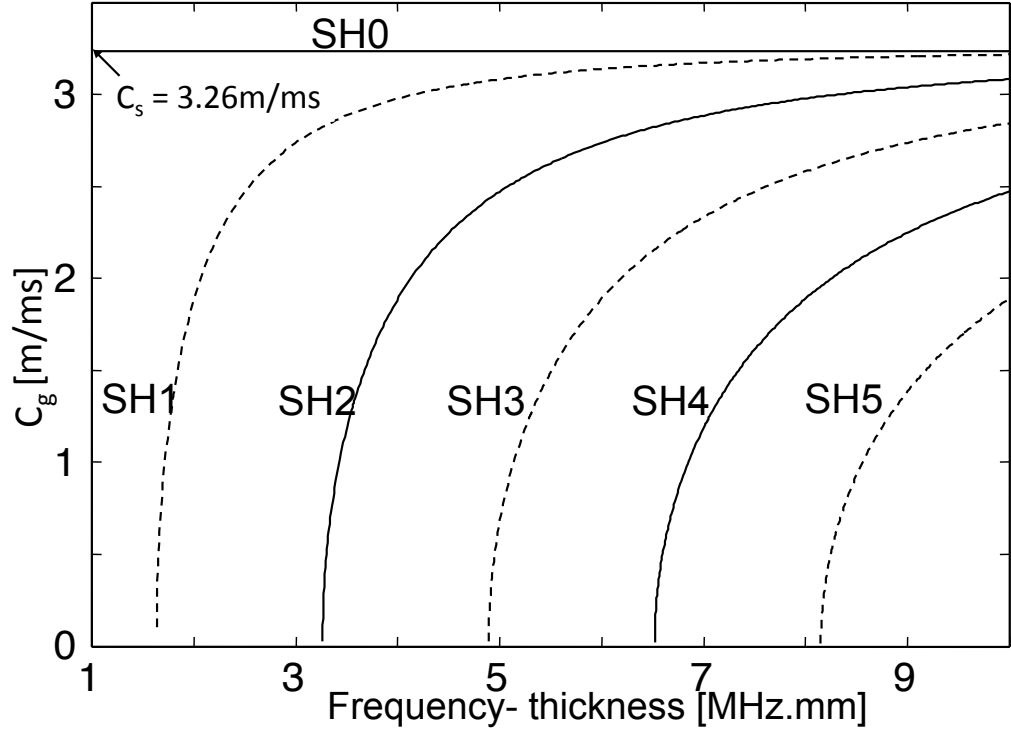
Figure 2.4: *Group velocity dispersion curves for the SH modes in a steel plate ($c_S = 3260 m/s$). Symmetric modes are plotted in solid line and antisymmetric modes in dotted line.*

group velocity represents the velocity at which the energy of a multi-frequency wave packet is traveling. The group and phase velocities are related by the following formula that can be deduced by the equation 2.22 after some algebra illustrated in [65].

$$c_g(ft) = c_s\sqrt{1 - \frac{(l/2)^2}{(ft/c_s)^2}}. \tag{2.25}$$

2.4 Guided waves in hollow cylinders

The study of the propagation of guided waves in hollow cylinders or pipes was intensively studied in the past, for example [72–74]. Pochhammer [75] and Chree [76] started to focus on this subject at the end of the 1800s, the solution of the set of governing equations was found and documented in textbooks like [65, 67]. Gazis
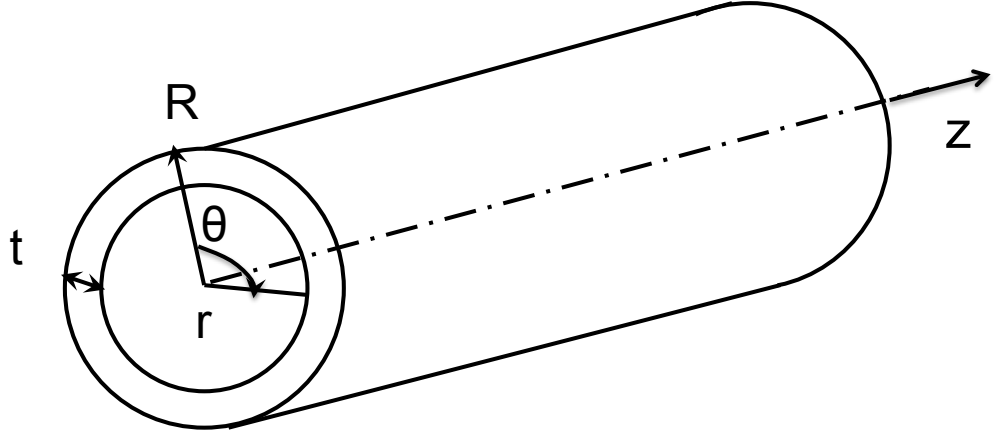
Figure 2.5: *Schematic representation of pipe geometry and cylindrical coordinate set (r,θ, z)*

in [72] presented a general analytical solution for the propagation of the waves in three-dimensional hollow circular cylinders of infinite extent in 1959. This solution was validated empirically by Fitch [77] in 1963. This technique is similar to the method of potentials presented for the free plate case in the section 2.3. In the case of hollow cylinders, a cylindrical coordinate system needs to be introduced and it is shown in Fig. 2.5. Two potential functions, the scalar ϕ and vector $\mathbf{\Psi}$ (defined in equations 2.11) are used. If a harmonically oscillating source is considered, the general solution (equation 2.11) of the Helmotz differential equations becomes

$$\phi, \mathbf{\Psi} = \Upsilon_{\phi,\mathbf{\Psi}}(\mathbf{r})\Upsilon_{\phi,\mathbf{\Psi}}(\theta)\Upsilon_{\phi,\mathbf{\Psi}}(z)e^{i(\mathbf{kr}-\omega t)} \tag{2.26}$$

where $\Upsilon_{\phi,\mathbf{\Psi}}(r, \theta, z)$ indicates the variation for each of the coordinates (r, θ, z) and $\mathbf{r}$ is the radial position vector. In the case of no wave propagation in the radial direction, the displacement field varies only in the $\hat{z}$ and $\hat{\theta}$ direction, and the solution can be simplified as

$$\phi, \mathbf{\Psi} = \Upsilon_{\phi,\mathbf{\Psi}}(r)e^{ik_\theta \theta}e^{i(k_z z - \omega t)}; \tag{2.27}$$

where k_z is the component of the complex wavenumber vector along the axial direction $\hat{z}$ and k_θ is the component of the wavenumber in the $\hat{\theta}$ direction. This angular wavenumber must be an integer in order to have an unique solution. Gazis in [72]

suggests different forms for the scalar potential ϕ and for the component of the vector potential $\boldsymbol{\Psi}_R$, $\boldsymbol{\Psi}_\theta$ and $\boldsymbol{\Psi}_z$ as follows

$$\phi = f(\mathbf{r})e^{i(n\theta+k_z z-\omega t)} \tag{2.28}$$

$$\boldsymbol{\Psi}_r = -g_{\mathbf{r}}(\mathbf{r})e^{i(n\theta+k_z z-\omega t)} \tag{2.29}$$

$$\boldsymbol{\Psi}_\theta = -ig_\theta(\mathbf{r})e^{i(n\theta+k_z z-\omega t)} \tag{2.30}$$

$$\boldsymbol{\Psi}_z = -ig_z(\mathbf{r})e^{i(n\theta+k_z z-\omega t)}. \tag{2.31}$$

In these equations n expresses the circumferential order. A general solution has been presented in sec. 2.2, the substitution of the equations 2.28 - 2.31 into the equation 2.7 gives a solution for the unknown variables $f(\mathbf{r})$, $g_{\mathbf{r}}(\mathbf{r})$, $g_\theta(\mathbf{r})$ and $g_z(\mathbf{r})$ which all satisfy the Bessel differential operator as discussed in [72]. A full discussion on the choice of arguments of the Bessel functions is presented in [78].

Recalling the equation 2.5 and the vector operations in cylindrical coordinates [78], the displacement field at an arbitrary location in the medium can be expressed as

$$u_r = \frac{\partial \phi}{\partial r} + \frac{1}{r}\frac{\partial \boldsymbol{\Psi_z}}{\partial \theta} - \frac{\partial \boldsymbol{\Psi}_\theta}{\partial z} \tag{2.32}$$

$$u_\theta = \frac{1}{r}\frac{\partial \psi}{\partial \theta} + \frac{\partial \boldsymbol{\Psi_r}}{\partial z} - \frac{\partial \boldsymbol{\Psi_z}}{\partial r} \tag{2.33}$$

$$u_r = \frac{\partial \phi}{\partial z} + \frac{1}{r}\frac{\partial}{\partial r}(r\boldsymbol{\Psi}_\theta) - \frac{1}{r}\frac{\partial \boldsymbol{\Psi_r}}{\partial \theta}. \tag{2.34}$$

These displacement components can be expressed also in terms of the four unknown variables ($f(\mathbf{r})$, $g_{\mathbf{r}}(\mathbf{r})$, $g_\theta(\mathbf{r})$ and $g_z(\mathbf{r})$) by substituting the equations 2.28-2.31 in the above expressions. More details in [78].

Since the cylindrical structure has no contact with any other media at the interfaces, the boundary conditions of this free motion pipe problem require that the normal and tangential stresses must vanish at the interfaces. This means that at r = R and r = R- t the following components of the stress tensor must be equal to zero;

$$\sigma_{rr} = \sigma_{r\theta} = \sigma_{rz} = 0. \tag{2.35}$$

In this section the propagation of the guided waves in cylindrical pipes in vacuum is discussed; in practice the presence of liquid or gas flow would introduce more boundary conditions and complexity to the problem. Using the strain-displacement ($\epsilon = func(\mathbf{u})$)and Hooke's equation for cylindrical structures (that relates the stress to the strain in the cylindrical coordinates) it is possible to write the stress tensor as function of the displacement field ($\sigma = func(u)$). For more details about the mathematical procedure to obtain this relationship see [78].

2.4.1 Modal properties

There are an infinite number of mode solutions of the wave propagation problem in a hollow cylinder as mentioned in the last section. Silk and Bainton [46] determined a conventional way to track the different modes by type, circumferential order ($n = 0, 1, 2....$) and consecutive order ($m = 1, 2, 3...$); the same notation is used in this thesis. A dual index system (n, m) identifies the modes uniquely. The modes with $n = 0$ are axially symmetric, whereas the value of $m = 1$ is associated with the fundamental modes. Higher 'n' order modes exhibit increased complexity around the circumference of the pipe whereas higher values of the counter 'm' means increased complexity of the vibration through the thickness of the pipe. m Three types of modes are identified (see Fig. 2.6):

a) Longitudinal modes ($L(0, m)$): longitudinal axially symmetric modes.
Their displacement field is $u_r \neq 0$, $u_\theta = 0$ and $u_z \neq 0$. They are similar to the Lamb modes in plates discussed in sec. 2.3.

b) Torsional modes ($T(0, m)$): rotational axially symmetric modes, their displacement is primarily in the circumferential direction. Their displacement field is $u_r = 0$, $u_\theta \neq 0$ and $u_z = 0$. They are similiar to the SH waves presented in the section 2.3.1.

c) Flexural modes ($F(n, m)$): non axially-symmetric modes. Their displacement field is $u_r \neq 0$, $u_\theta \neq 0$ and $u_z \neq 0$.
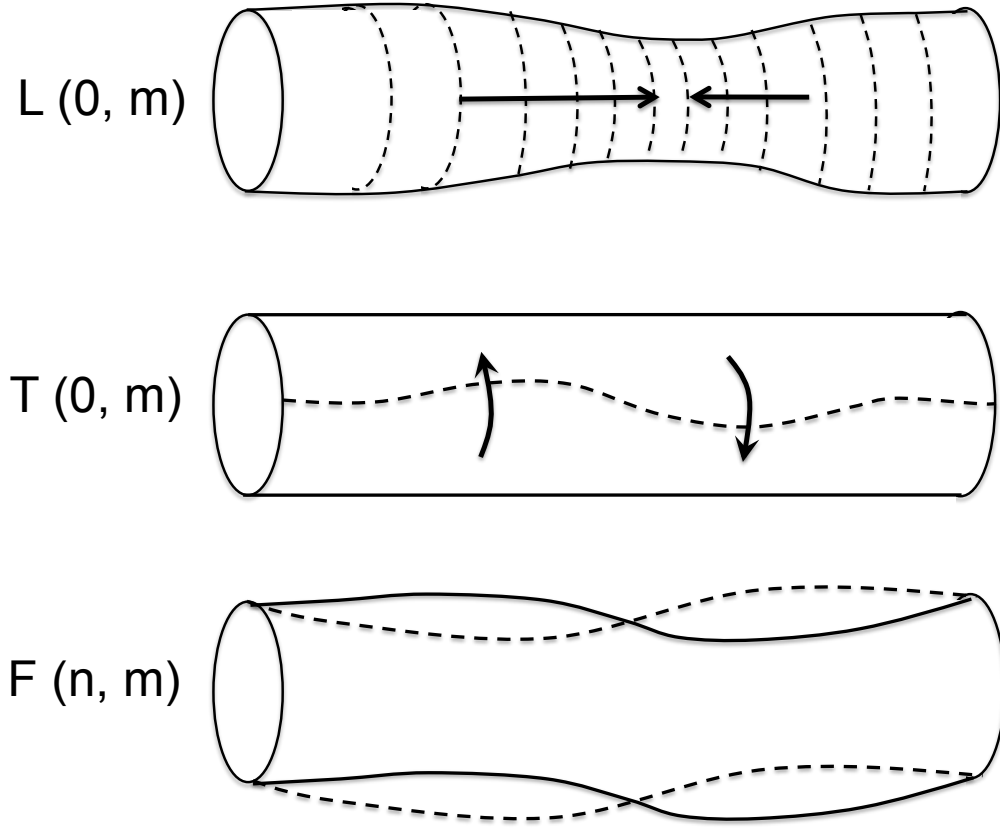
Figure 2.6: *Schematic representation the three types of modes present in pipes*

Figure 2.7 shows the dispersion curves in terms of phase velocity versus frequency-thickness produce for a 3 inch steel pipe in vacuum; these curves were calculated with Disperse [69, 70]. The most used longitudinal, torsional and flexural modes are highlighted in this figure.

2.5 Relationship between guided waves in plates and pipes

In the last two sections the solutions for wave propagation in free plates (sec. 2.3) and in cylindrical structures (sec. 2.4) have been discussed and some analogies between them have been found. In the past, several studies focussed on the similarities between the modes propagating in these two structures [79, 80]. It was shown that longitudinal $L(0, m)$ correspond to Lamb waves in plates, while torsional modes
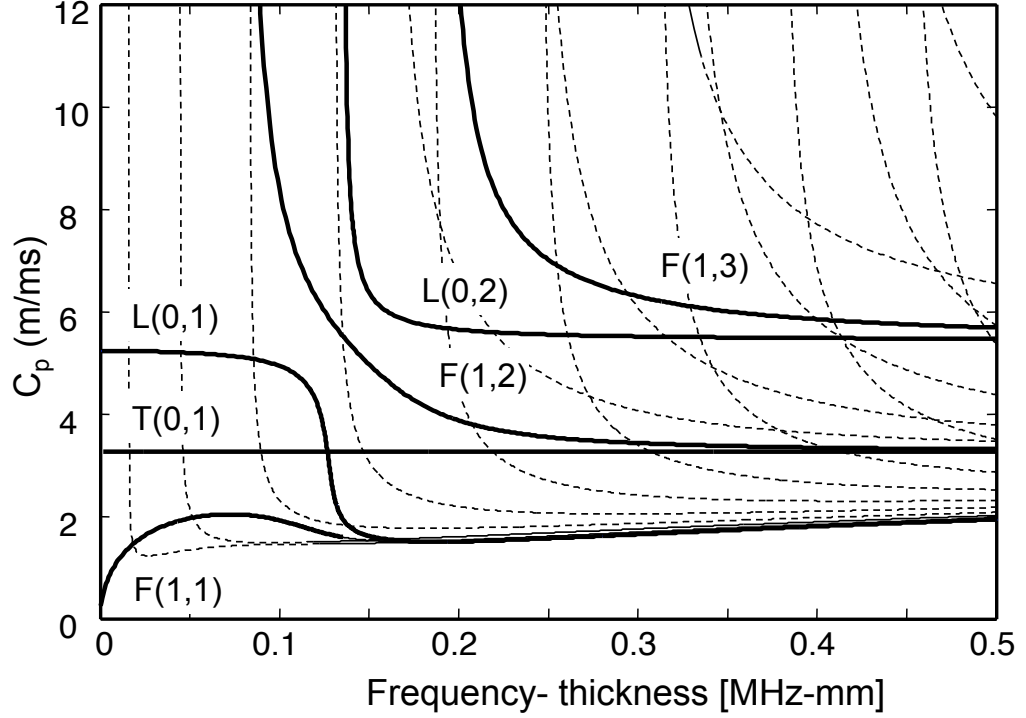
Figure 2.7: *Dispersion curves in terms of phase velocity versus frequency-thickness product for a 3 inch steel schedule 40 pipe in vacuum.*

T(0, m) in pipes correspond to SH waves in plates [67, 79]. This means that the $T(0, 1)$ mode corresponds to SH_0, and $L(0, 2)$ corresponds to the S_0 Lamb mode in a range of frequency-thickness product from about 0.2 MHz-mm (for a 3 inch schedule 40 steel pipe) to the L(0, 3) cut off frequency-thickness value; whereas $L(0, 1)$ corresponds to S_0 below the value of 0.03 MHz-mm and to A_0 above about of 0.2 MHz-mm for the same pipe size. In the same way for a 8 inch schedule 40 steel pipe, $L(0, 2)$ corresponds to the S_0 Lamb mode in a range of frequency-thickness product from about 0.075 MHz-mm to the L(0, 3) cut off frequency-thickness value; whereas $L(0, 1)$ corresponds to S_0 below the value of 0.02 MHz-mm and to A_0 above about of 0.075 MHz-mm for the same pipe size. Figure 2.8 shows the longitudinal L(0, 1) and L(0, 2) dispersion curves in terms of phase velocity versus frequency-thickness product for 3 and 8 inch schedule 40 steel pipes; these curves are compared with the dispersion curves of A_0 and S_0 Lamb modes in steel plates. It is clear that on increasing the pipe diameter the modes in the pipe become more similar to the ones in plates. Lately Velichko and Wilcox in [81] analyzed the relationship between
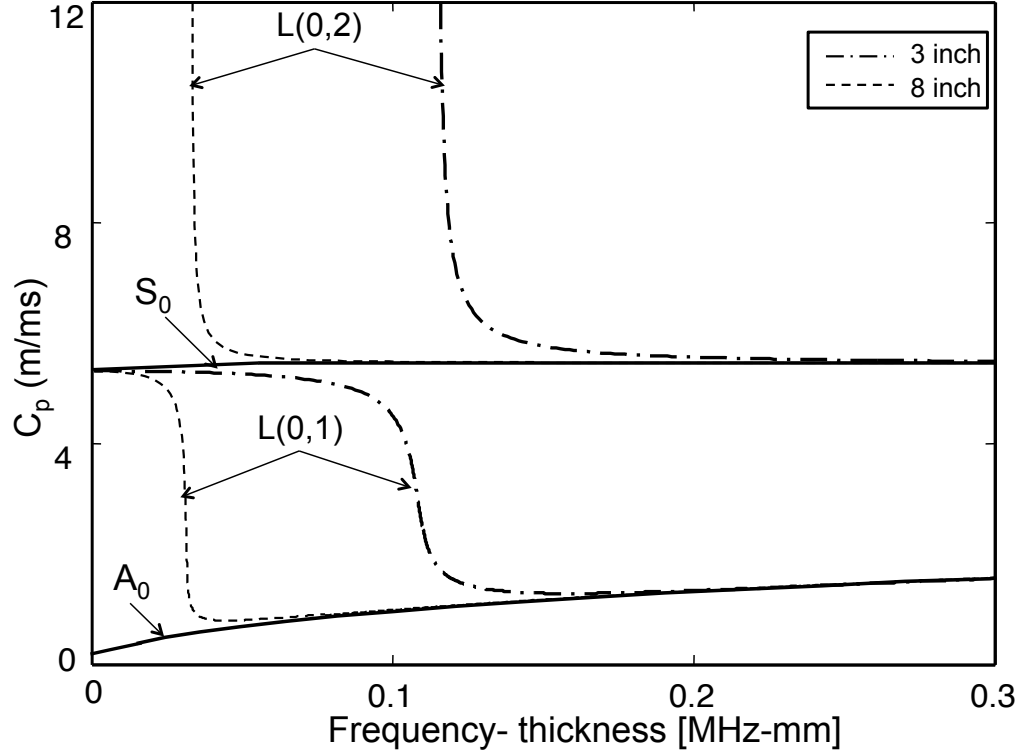
Figure 2.8: *Comparison between longitudinal mode L(0, 1) and L(0, 2) dispersion curves expressed as phase velocity versus frequency-thickness product in 3 inch and 8 inch schedule 40 steel pipes and dispersion curves of A_0 and S_0 Lamb modes in steel plates.*

plate and pipe solutions which is briefly presented below. Figure 2.9 shows a hollow cylinder and its corresponding unrolled plate with the cylindrical coordinates (θ, y, z) in both geometries. The physical solution of the wave propagation problem must be periodic in the angular direction θ, the period being 2π so that the displacement fields of the pipe can be expressed as a superposition of displacements in the unbounded structure in the θ direction like so

$$\mathbf{u}(\theta, y, z) = \sum_{n=-\infty}^{+\infty} \mathbf{u}_{unb}(\theta + 2\pi n, y, z) \tag{2.36}$$

where n is an integer and $\mathbf{u}_{unb}$ is the solution to the problem of excitation of guided waves in unbounded media due to excitation forces that are nonzero only for values of θ in the interval $[0, 2\pi]$. Velichko and Wilcox [81] and Li and Rose [80] stated that if the curvature of the pipe is negligible then the pipe problem can be approximated as an unrolled plate. The effect of the curvature can be neglected if the following
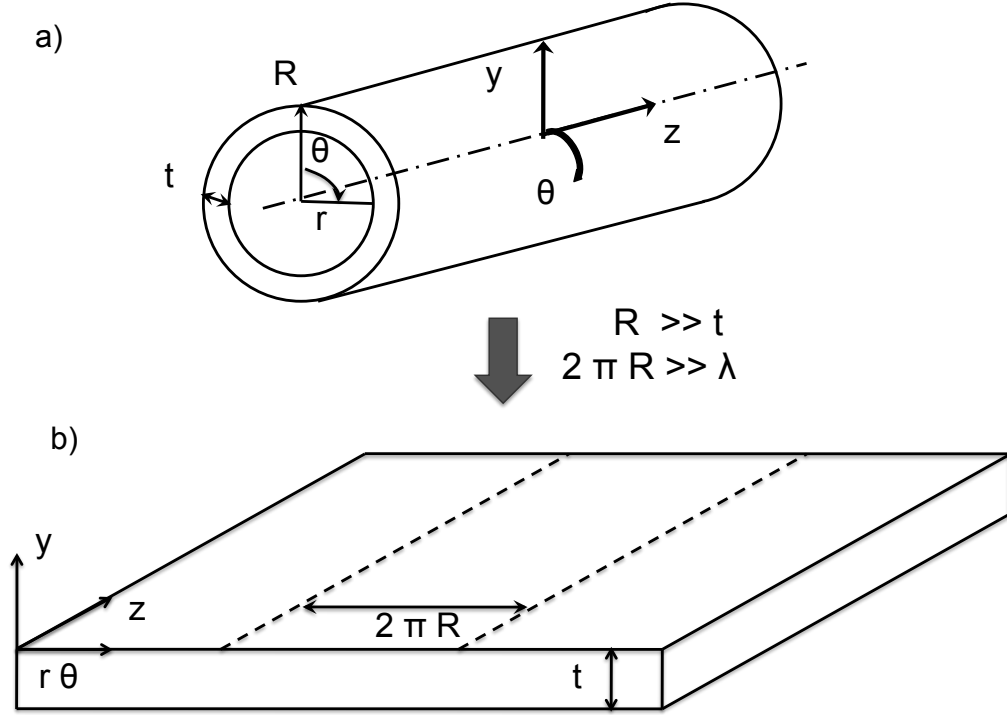
Figure 2.9: *Schematic representation of pipe (a) unrolled and replaced by an infinite plate (b) if the the effect of the curvature can be neglected. Cylindrical coordinates (θ, y, z) in both geometries are also shown.*

two condition are satisfied:

$$R >> t \tag{2.37}$$

$$2\pi R >> \lambda. \tag{2.38}$$

The first condition implies that the curvature of the pipe is approximately constant through the thickness of the pipe. The second condition implies that the wavelength is much less than the pipe circumference so that the curvature has a negligible effect on the wave propagation. Again the detailed analysis can be found in [81] as well as a quantitative analysis of the limitations of this analogy. The formula proposed to convert the scattered field from a plane wave excitation in a plate (S_{plate}) to a axi-symmetric excitation in a pipe (S_{pipe}), provided that the equations 2.37-2.38 are satisfied, is
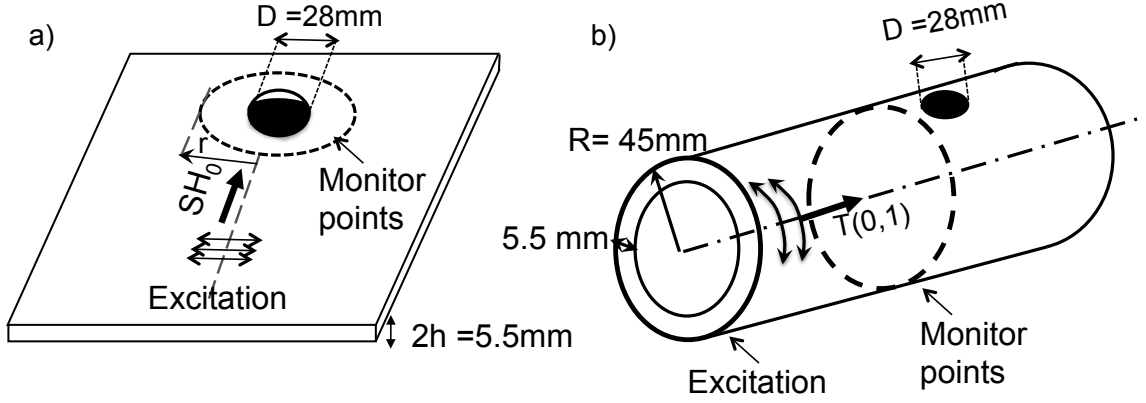
Figure 2.10: *Schematic of the geometries used for the FE simulations of the scattering field from a through-thickness circular hole with diameter of 28 mm in a) a plate and b) a 3 inch schedule 40 pipe.*

$$S_{pipe} = \frac{\sqrt{\lambda}e^{i\pi/4}}{2\pi R}S_{plate},\qquad(2.39)$$

where the scattering matrix S_{plate} is defined as the ratio of the amplitude of the reflected signal measured in the far-field of the scatterer and the amplitude of the incident wave at the centre of the defect. S_{pipe} is also defined as the ratio of the scattered field and the amplitude of the incident signal calculated at the monitoring distance from the scatterer. This matrix S_{pipe} is independent of the monitoring distance since there is no beam spreading in the pipe case from the scatterer [22,82].

2.5.1 Application of the plate-pipe analogy to a through the thickness circular hole

In this section an application of the method detailed in sec 2.5 is presented. The scattering (RC_{plate}) from a through thickness circular hole (28 mm diameter) in a steel plate (E = 210GPa, $\rho = 8100$ kg/m^3 and Poisson's ratio = 0.3) of dimensions
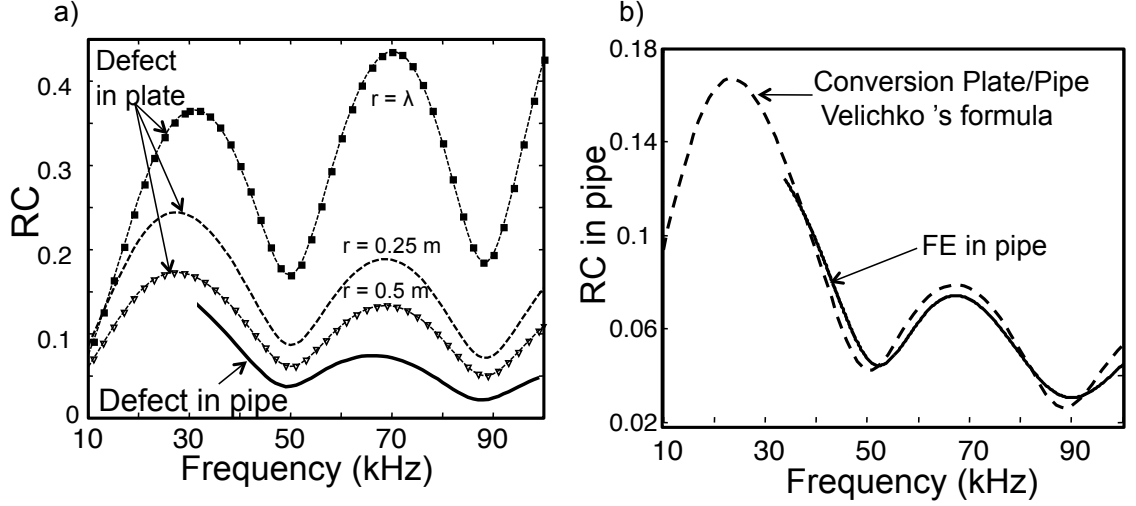
Figure 2.11: *a)Reflection coefficient (RC) spectrum from a circular defect in a plate measured at r = 0.25 m (−−) , 0.5 m (−▽−)and at r = λ (−■−) and in 3 inch schedule 40 pipe with 5.5mm wall thickness (solid line) b) Comparison of the FE results of the RC spectrum from a circular defect in pipe(solid line) and from a circular defect in plate using Veilichko formula 2.39 (−).*

1.6 x 1.6 m and with a thickness of 5.5 mm was simulated with the finite element software, Abaqus. Then, the reflection RC_{pipe} from the same circular hole created in a 3 inch schedule 40 (5.5 mm wall thickness) pipe was calculated. The SH_0 mode was excited in the plate and the T(0, 1) mode in the pipe, the geometric configurations are shown in Fig. 2.10. The results from these simulations are shown in Fig. 2.11a. The three RC spectrum curves from the hole in the plate shown in Fig. 2.11a were obtained measuring the reflected signal at 0° incidence angle and at three different distances from the centre of the defect: r = 0.25 m, 0.5 m and at r = λ. It is evident that the RC values decrease with increasing distance from the scatterer and in particular the RC is proportional to $\sqrt{h/r}$, where h is half of the plate thickness as shown in Fig. 2.10. These results agree with past work such as [22, 82]. In addition, it is interesting to note that the overall RC spectrum curve calculated at $r = \lambda$ increases with frequency, since the wavelength decreases. In contrast, as mentioned in the section 2.5 the reflection from the defect in the pipe RC_{pipe}, which is plotted with a solid line in Fig. 2.11a, is independent of the distance between the monitoring point and the scatterer. Figure 2.11b shows the comparison

between the RC spectrum from the hole in pipe shown already in Fig. 2.11a, and the RC spectrum obtained using the RC_{plate} field and applying the formula 2.39 at several frequencies. The value of R used in the equation is the radius in the middle of the pipe wall thickness (R = 41.75 mm for a 3 inch pipe) as suggested in [81]. It is clear that the two curves match well, confirming the validity of the formula.

2.6 Inspection with guided waves: choice of excitation modes and frequency range

The main goal of using guided waves in NDT is to locate and possibly size discontinuities in structures. The dispersion curves presented in sec. 2.4.1 are used in practice to determine the best test conditions. They mainly describe the properties of the guided waves in terms of phase velocity, group velocity and mode shape which are very useful to interpret the test results.

One big concern in the choice of the guided wave modes for practical testing is the *dispersion* of the waves i.e. variation of the velocity with the frequency. The group velocity c_g of cylindrical waves as function of frequency-thickness (ft) product in a 3 inch in a vacuum is shown in Fig. 2.12. In this figure torsional, flexural and longitudinal modes are shown in ft range 0-0.5 MHz-mm. It is clear that, as was mentioned for plates in section 2.3.1, cylindrical waves are generally dispersive so the shape of the wave packet is distorted. The fundamental torsional mode T(0, 1) is the only non-dispersive mode at all frequencies, as is the SH_0 mode in plates. This distortion generally causes a reduction of the amplitude of the signal and increases the length of the signal in the time domain. More quantitative investigation on dispersion and the way to optimize the tests is given in [83–85]. The effect of dispersion increases with the propagation distance so it is particularly important in long range testing. It is this therefore usual to use a non-dispersive mode [86,87] to avoid the distortion effect.

The guided wave packet traveling along the length of a pipeline is reflected by

changes in the structure; the geometry of the feature will lead to different reflected modes depending on its size, shape and location and on the nature of the input signal. If an axi-symmetric mode is incident on an axi-symmetric feature, only axi-symmetric features will be reflected, whereas flexural modes will occur if the discontinuity is non-symmetric. This physical principle helps in practice to distinguish between a corroded area (typically non-symmetric) and a weld (typically symmetric) in a pipeline [42]. Figure 2.13 shows a typical time trace signal numerically predicted in a 3 inch schedule 40 steel pipe (outer radius 44.5 mm, wall thickness 5.5 mm) with a flat bottomed rectangular defect (axial and circumferential extent of 0.06m and 0.03m respectively) its depth being 50% of the wall thickness. The fundamental torsional mode T(0, 1) mode was excited as a tonebust signal centred at 70kHz and with 2 cycles. This mode is reflected from the defects as plotted with a dotted line in Fig. 2.13. Since the discontinuity is non axi-symmetric the mode is converted into both symmetric and non-symmetric modes which exist in the bandwidth of the excitation signal (in this case from 30 to 100 kHz). In this figure the first order flexural modes $F(1, m)$ are shown but higher modes can be extracted and plotted as well. These modes are extracted using the method proposed by Lowe *et al.* in [42]. The more similar is the particle motion between the modes, the stronger the mode conversion. In the example only T(0, 1) is excited which has only tangential displacements at all the frequencies. F(1, 2) also has a dominant tangential displacement in this frequency range, so its reflection is strong. In contrast, F(1, 3) which is faster than F(1, 2), has a dominant longitudinal displacement so its reflection is weaker.

In the literature, studies on axi-symmetric [30, 33, 34, 41, 42, 88–90] and non axi-symmetric [91–98] *excitation* of guided wave modes for inspection have been carried out. Axi-symmetric modes are typically deployed in commercial equipment for long range inspection [34, 88–90]; this is basically because it is easy to excite axially symmetric waves using equally spaced transducers located around the pipe circumference. These commercial systems are used worldwide for screening pipelines from a single location over a range of tens of meters. Two axi-symmetric modes are mainly used, L(0, 2) and T(0, 1). Since they are axi-symmetric and they show a
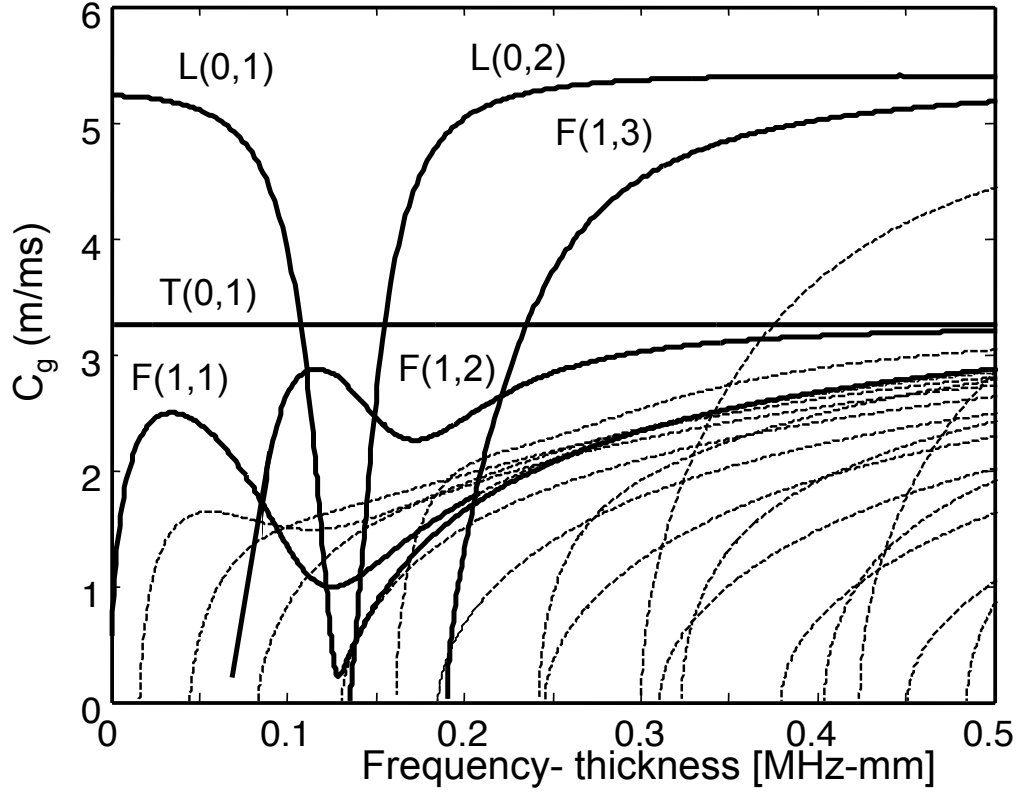
Figure 2.12: *Dispersion curves in terms of group velocity for a 3 inch schedule 40 steel pipe (outer diameter 89 mm, wall thickness of 5.5 mm).*

near constant mode shape through the wall thickness, they achieve a full pipe-wall coverage in the frequency range generally used for inspection [30]. The axial location of the defect is usually defined by the arrival time of the signal reflected from the defect. In the literature, the L(0, 2) mode was firstly adopted for inspection of structures [33, 41, 42]. However, more recent applications have preferred to employ T(0, 1) for several reasons. First of all L(0, 2) is non-dispersive in a limited range of frequency (from 0.275 to 0.55 MHz-mm for a 3 inch steel pipe as shown in Fig. 2.12), whereas T(0, 1) is entirely non-dispersive, so making the post-processing of the signals less complex than L(0, 2) mode. The excitation of L(0, 2) is also more complex since the transducers have to be carefully designed to suppress the unwanted excitation of the L(0, 1). The key advantage of T(0,1) mode is that, since liquids cannot support shear waves, its propagation characteristics are not affected by the presence of liquid in pipes [30]; in contrast with L(0, 2) that leaks energy into the liquid. This means that T(0, 1) can be used for testing the majority of pipelines
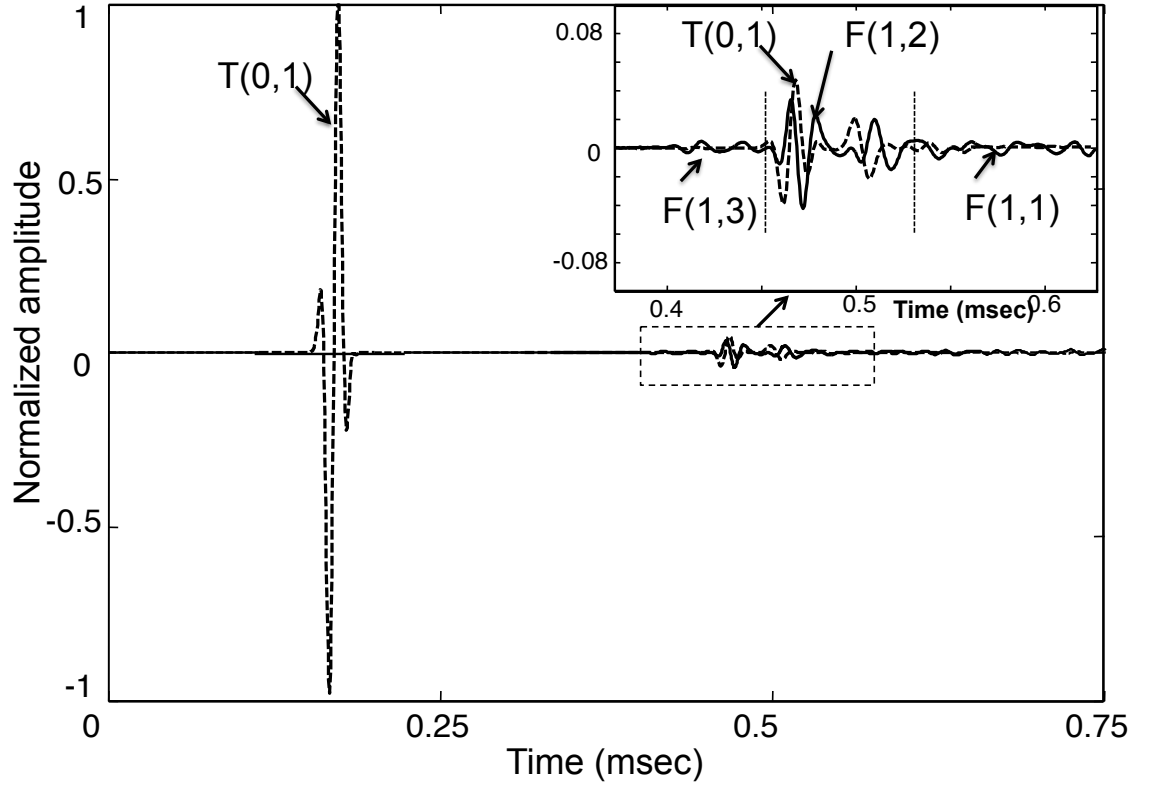
Figure 2.13: *Time trace and mode converted by a flat bottomed rectangular defect (axial extent of 0.06m and circumferential extent of 0.03m), its depth being 50% of the wall thickness simulated with Abaqus in a 3 inch schedule 40 steel pipe. T(0,1) mode is plotted in dotted line, first order flexural converted modes are plotted in solid line.*

in operation.

The scattered field from features present in the structure contains signatures of the feature itself and this is helpful to estimate its severity. The information present in a scattered wave packet changes with the *frequency* at which the wave packet is excited. At low frequencies for example the reflected signal from a finite defect is proportional to the cross sectional area removed [37, 42]. If sizing a defect is also a goal then testing becomes more challenging. Low frequencies of operation give long wavelengths of the input signal which are therefore not able to detect and size small defects. Figure 2.13 shows FE predictions of axially symmetric modes such as T(0, 1) converted to non axi-symmetric modes related to the circumferential extent of the defect [33, 42, 99]. Demma *et al* in [37] proposed a method to size the circumferential

extent of the defect by looking at the ratio of the reflected first order flexural mode to that of the excited axi-symmetric mode. However, this technique does not work at low frequencies (e.g. $f < 24kHz$ for a 3 inch schedule 40 steel pipe) since the excited axi-symmetric mode T(0, 1) does not convert to the flexural reflected component F(1, 2) because the F(1, 2) mode does not have a predominant torsional behavior in this frequency range, see [30] for more details. Frequency range higher than the one used in practices could be used for sizing a discontinuity since the waves have a shorter wavelength and therefore the inspection could become more sensitive to detect small defects; however, the use of higher frequencies of inspection means also propagation of multiple dispersive modes. Several parameters need then to be taken in account when choosing the frequency range for rapid screening of structures with guided waves. As mentioned above, T(0, 1) is naturally non-dispersive at all the frequencies; however frequency limits occur when exciting T(0, 1) due to the transducer design, mode conversion and excitation of unwanted modes at higher frequencies such as T(0, 2) [37]. The range of frequency commonly used when either L(0, 2) or T(0, 1) modes are used for rapid screening in commercial applications is from 10 to 65kHz [34].

In most practical pipe inspection cases and in this thesis the fundamental torsional mode T(0, 1) is used mainly for screening of pipes [30,100]. As mentioned above, the main advantage of the choice of this mode is its insensitivity to liquids which allows the application of T(0, 1) for the inspection of most of the pipelines in operation. In addition, it is axially symmetric ($n = 0$) and non-dispersive at all the frequencies therefore easier to control, post-process and interpret the results. The goal here is to determine whether the scattering of this mode from a complex defect carries enough information to determine the maximum depth of the defect once it has been located.

2.7 Finite element simulations of guided waves

The scattering of guided waves from defects is usually divided in regimes defined by the parameter ka where k is the wavenumber and a is the characteristic dimension of the defect [30, 101–103] . The regimes are divided as follows:

1) $ka < 0.1$ (or $ka << 1$). The wavelength of the input signal is longer compared with the extension of the defect, in this case Born [58, 104–106] and quasi static [107, 108] approximations can be adopted to solve the problem analytically if the shape of the defect is simple.

2) $ka > 1$. The wavelength is smaller than the defect characteristic dimension and the Kirchhoff approximation [109, 110] and geometrical diffraction theory [111] are adopted. Rajagopal in [112] gives a good review of the different approaches and approximations used in this case.

3) $1 > ka > 0.1$. The dimensions of the scatterer are comparable with the wavelength of the input signal and/or the shape of the discontinuity is complex. In this case numerical methods are adopted such as finite elements (FE), finite difference (FD) or boundary elements (BE). In this thesis the FE method is mainly used with ABAQUS/Explicit v.6.7 [113] and v.6.9 [114]. In FE, the structure is divided into a finite number of elements of finite size, they are connected with the rest of the structure at the boundaries of each element. The governing wave motion equation 2.7 is therefore expressed in a finite form (see equation 2.40) and solved in terms of field variables at the nodal points. The equation of dynamic equilibrium can be expressed as

$$[\mathbf{M}]\ddot{\mathbf{u}} + [\mathbf{C}]\dot{\mathbf{u}} + [\mathbf{K}]\mathbf{u} = [\mathbf{F_{ext}}], \tag{2.40}$$

where $\mathbf{u}$ is the dispacement vector and therefore $\dot{\mathbf{u}}$ and $\ddot{\mathbf{u}}$ represent velocity and acceleration vectors respectively. The matrix $[\mathbf{M}]$ is a diagonal mass matrix dependent on the density of the material used, $[\mathbf{C}]$ is the viscous damping matrix determined by Rayleigh damping, the matrix $[\mathbf{K}]$ is the static stiffness matrix defined by the Young's modulus and Poisson's ratio. $[\mathbf{F_{ext}}]$ are the external forces applied to the

system. In this thesis no damping in the system is included since propagation in elastic materials is considered ($[\mathbf{C}] = 0$). The wave propagation equation is implemented by applying forces or displacement constraints to a selected set of nodes. Usually these forces are applied in the form of a tone bust. The explicit direct time stepping method is based on a central difference operator that links the values of $\mathbf{u}$, $\dot{\mathbf{u}}$ and $\ddot{\mathbf{u}}$ as below [115]

$$
\dot{\mathbf{u}}^{(i+1/2)} = \dot{\mathbf{u}}^{(i-1/2)} + \frac{\mathbf{\Delta t}^{(i+1)} + \mathbf{\Delta t}^{i}}{2} \ddot{\mathbf{u}}^{(i)} \tag{2.41}
$$

$$
\mathbf{u}^{i+1} = \mathbf{u}^{(i)} + \mathbf{\Delta t}^{(i+1)} \dot{\mathbf{u}}^{(i+1/2)} \tag{2.42}
$$

where Δt is the time increment and i is the time increment counter.

One advantage of this scheme is that the procedure advances by using the known values of the variable at the previous step. This is a more efficient procedure than the implicit one, where the dynamic equilibrium is satisfied at the end of each time step and to determine the displacement field $\mathbf{u}$ it is necessary to invert the mass matrix of the equation 2.40. In contrast, the explicit central-difference scheme implies that the mass matrix $[\mathbf{M}]$ is diagonalized so the accelerations are calculated simply by multiplying the mass matrix and the difference between the applied load vector, $[\mathbf{P}]$ and the internal force vector $[\mathbf{I}]$ [78].

For the FE simulations to converge and in order to solve properly the propagating waves, the values of Δt and Δx must be carefully chosen especially when simulating complex features. Δt in equation 2.42 has to be smaller than the time for the fastest wave to propagate between nodes. As reported in the Abaqus manual [114] the time step has to be

$$
\Delta t \approx \frac{x_{min}}{c_d \sqrt{G}}, \tag{2.43}
$$

where x_{min} is the smallest nodal distance in the mesh, c_d is the velocity of the fastest wave and G is the dimensional order of the model.

The size of the elements Δx (which is not always the same as x_{min} e.g. in the case of triangular elements [115]) has to be chosen to solve the propagating waves. In the

past Alleyne et al. [116] suggested that at least 10 nodes per wavelength for a uniform square mesh have to be employed ($\Delta x = \frac{\lambda_{min}}{10}$). Moser et al. in [117] suggested that 20 nodes per shortest wavelength are necessary. It is clear that all these rules depend on the complexity of the geometry to be analyzed and on the accuracy required. Lately, Drozdz [115] analyzed the effect of the mesh parameters on the results of different wave propagation problems and proved that a refinement of the mesh is necessary when complex geometries are present. The Δt and Δx necessary for the FE models to converge for a variety of element types were also assessed; he concluded that with regards to the mesh density, it is difficult to provide a general rule. Nevertheless, he stated that using triangular elements a mesh density of 30 element per wavelength generally provides excellent qualitative and quantitative results but depending on the complexity of the defect, a local refinement may also be needed. It is therefore down to the modeller to decide what mesh density to use for a particular model based on what is required from the model. In this thesis the analysis of complex shaped defects in pipes is presented; an average element size of about 20 element per wavelength was used for the solution to converge. For each model type used throughout this thesis convergence tests were run to refine the mesh and time stepping. The models were also validated with experiments.

2.7.1 General procedure for FE simulations

Finite element (FE) models have been successfully applied by previous workers to simulate the interaction of guided ultrasonic waves in structures such as pipes and plates with defects [6, 17, 21, 23, 26, 28, 30, 32–34, 36, 37, 40–43, 47]. In this thesis the interaction of the T(0, 1) mode with axi-symmetric and 3D discontinuities is analyzed. In principle an axi-symmetric defect in a pipe may be simulated by an axi-symmetric FE model; this approach would reduce the simulation to a 2D analysis which can deal with defects that remove part of the wall thickness all around the pipe. Although this approach is very convenient, it is not possible to represent torsional modes travelling along axi-symmetric models in the time domain in the commercial FE software Abaqus, due to a limitation of the software. A full three

dimensional (3D) solid finite element (FE) model in Abaqus is therefore adopted to study the interaction between the T(0, 1) mode and both axi-symmetric and finite defects [40–43]. The T(0,1) mode was produced in the FE models by assigning displacements to the nodes around the outside of the pipe at the excitation end. When both the excitation and the features in the pipe are axi-symmetric, only the T(0,1) mode is present, while the existence of a non-symmetric discontinuity generates other modes by mode conversion, but only the T(0,1) reflection is considered in this thesis. This can be extracted by summing the responses at a set of uniformly distributed monitoring points around the pipe circumference [42]. In most of the cases the pipe was meshed with first order tetrahedral elements; the average element size (Δx) varied from $\frac{\lambda}{15}$ to $\frac{\lambda}{22}$ depending on the complexity of the defect. Consequently the formula 2.43 was adopted to determine the first guess of Δt for the simulations. As mentioned in the last section, convergence tests are run for each model type used throughout this thesis to refine the starting guess of parameters controlling the simulations; experimental measurements also were used to validate the FE results. In each of the models presented in the following chapters the input signal was a 2 cycle Hanning windowed tonebust with a centre frequency of 70 kHz, resulting in a frequency range of 20-100 kHz.

2.8 Guided waves conclusion

The fundamental concepts of bulk and guided waves propagating in structures such as plates and pipes have been introduced. In isotropic plates two kinds of waves can propagates, SH and Lamb waves. The solution of the SH waves traveling in a stress-free isotropic plate has been investigated. Three different guided wave modes are present in hollow cylindrical structures: longitudinal, torsional and flexural modes; their properties have been studied. The analogy between guided waves propagating in plates and in pipes has been analyzed and applied to a simple case.

A brief discussion on the choice of the guided wave modes and frequency range for inspection has been also given. In addition a brief overview on the rules applied for the modeling of guided waves with the finite element (FE) technique has been given

and the details of the FE simulations discussed in next chapters of this thesis have been presented.

Chapter 3

Scattering from axi-symmetric defects with varying depth profile

3.1 Introduction

In this chapter the reflection of the fundamental torsional mode T(0, 1) from tapered axi-symmetric defects in pipes is discussed. Finite element (FE) analyses of the reflection from axi-symmetric tapered down- and up- steps and from tapered notches with different depths and varying slope angles are presented in section 3.2. In section 3.3, the reflection coefficients at tapered steps are used to simulate the reflection coefficient from a defect with a tapered depth profile using a superposition approach. These FE results are validated by experiments in section 3.4.

3.2 Finite Element Predictions

In this chapter three different discontinuities were modelled:

(1) The tapered step model (Figs 3.1a and 3.1b) was used to analyze the scattering behaviour when there was a gradual change of thickness in a restricted region of the pipe, the taper. Initially this model was used to understand whether there

was a continuous reflection inside the taper or if the reflection was produced only at its extremities. Both the cases in which the thickness increases (tapered step-up, see Fig. 3.1a) and decreases (tapered step-down, see Fig. 3.1b) were modelled. In both cases the thickness of the pipe at excitation was 5.5 mm. The reflection and transmission behaviour from a tapered step with two slopes of taper was then studied. The information derived from this model was used to reproduce semi-analytically the reflection from a tapered defect. In addition a 50% depth cosine taper shaped step model was created in order to understand the difference in the reflection behaviour between tapered steps with sharp and smooth slope changes.

(2) A tapered defect was defined as a discontinuity composed of two tapered steps, -down and -up, separated by a flat-bottomed zone (Fig. 3.1c). Two different depths of defect were analysed; for each of them the slopes of the two tapered regions were changed in order to study the effect of this change on the reflection coefficient be-
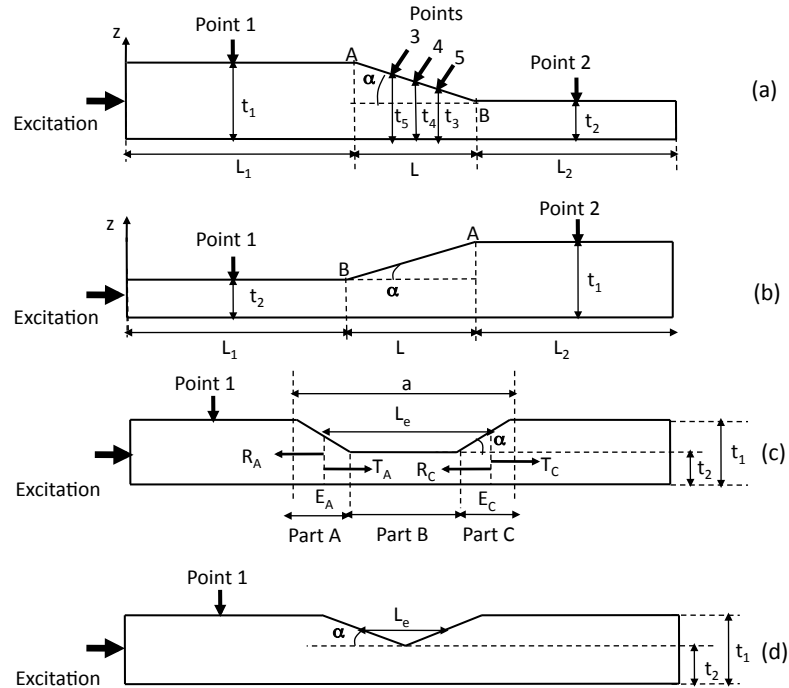
Figure 3.1: *Schematic of (a) tapered down-step, (b) tapered up-step, (c) tapered defect, and (d) V-notch.*

haviour. Numerical results from this model were used to validate the semi-analytical prediction of the reflection coefficient.

(3) The V-notch (Fig. 3.1d) is the extreme case of the tapered defect when the length of the flat-bottomed zone is reduced to zero. This model was employed to study the difference between the reflection coefficient from a tapered defect with a flat-bottomed zone and a tapered defect without it (V-notch).

As mentioned in section 2.7.1, 3D solid FE models were adopted in Abaqus to study the interaction between the T(0,1) mode and tapered steps, tapered defects and V-Notches. In the next section the details of these FE predictions are presented. The defects were modelled in pipes with outer diameter of 76.2 mm and wall thickness of 5.5 mm. Linear elements with Δx of 1.8 and 2 mm were used for these FE simulations, which converged with a time step Δt between 0.05 - 0.1 μsec depending on the complexity of the geometry of the defect. In each of the following models the excitation was at the left hand end of each of the model as shown in Fig. 3.1. The reflected wave was monitored at point 1 of each sketch of Fig. 3.1, which is located half way between the excitation end and the start of the discontinuity. The transmission of the T(0,1) through the tapered down- and up- steps was monitored at point 2, half way between the far end of the pipe and the second end of the tapered step (see Fig.s 3.1a and 3.1b). Three additional monitoring points were also set in the taper region of the tapered down-step in order to monitor the signal traveling inside the taper (Fig. 3.1a).

As mentioned in section 2.7, a parameter frequently used in scattering problems is the product ka, where a is the characteristic dimension of the defect, that in this study is its axial length (L), and k is the wave number. In this work the phase velocity c_p is not dependent on the frequency because T(0,1) is non-dispersive; thus the parameter used in the following scattering analyses is the ratio L/λ, where λ is the wavelength. The analyses on tapered defects are based on an equivalent length of the defect (L_e) expressed as the geometric average axial extent of the defect as shown in Fig. 3.1c. L_e represents the length of an equivalent rectangular notch with the same maximum depth of the tapered defect.

3.2.1 Tapered step

A tapered step was modelled in a pipe by creating two different thickness regions joined by a taper. The first model was a 0.86 m long pipe with a tapered region located 0.4 m from the left end of the pipe. This tapered step decreased the thickness by 50% over 0.06m with a slope of 2.62°; it was designed to study in detail the reflection characteristics inside the taper.

Figures 3.2a and 3.2b show the predicted signals received at point 1 for both down- and up- step cases. The first signal seen in each case is the T(0,1) incident wave travelling from the excitation end followed by two signals which are reflected from the two ends of the taper (A and B). The insets show that in each case the reflections from the two ends of the taper are out of phase. The reflection from the thicker end (A) is in phase with the input, while the reflection from the thinner end (B) is out of phase with the input.

The reflection coefficient (RC), which is defined as the ratio of the amplitude of the total reflection from the discontinuity (i.e. from the two ends together) to that of the incident signal, was calculated in the frequency domain. Figure 3.3 shows how the modulus of the reflection coefficient from different shaped steps varies with the length of the taper (L) expressed as a percentage of the wavelength (λ). Two linear tapers with different slopes (2.62° and 20°) and a cosine tapered step were studied; the reflection from a sharp step is also presented for comparison. The RC from a sharp step is constant in the frequency range before the T(0,2) cut-off frequency [30] and its value is dependent on the ratio of the cross section area at the notch location (A_2) to the cross section before the notch (A_1). Assuming that the mode shapes are constant through the thickness and the radius of the pipe is much greater then the thickness, the RC from a sharp step is given by [30]:

$$RC = \frac{1 - \alpha}{1 + \alpha} \qquad (3.1)$$

where α is $\frac{A_2}{A_1}$. For a 3 inch pipe with wall thickness of 5.5mm and a 50% sharp step the RC is 0.395.
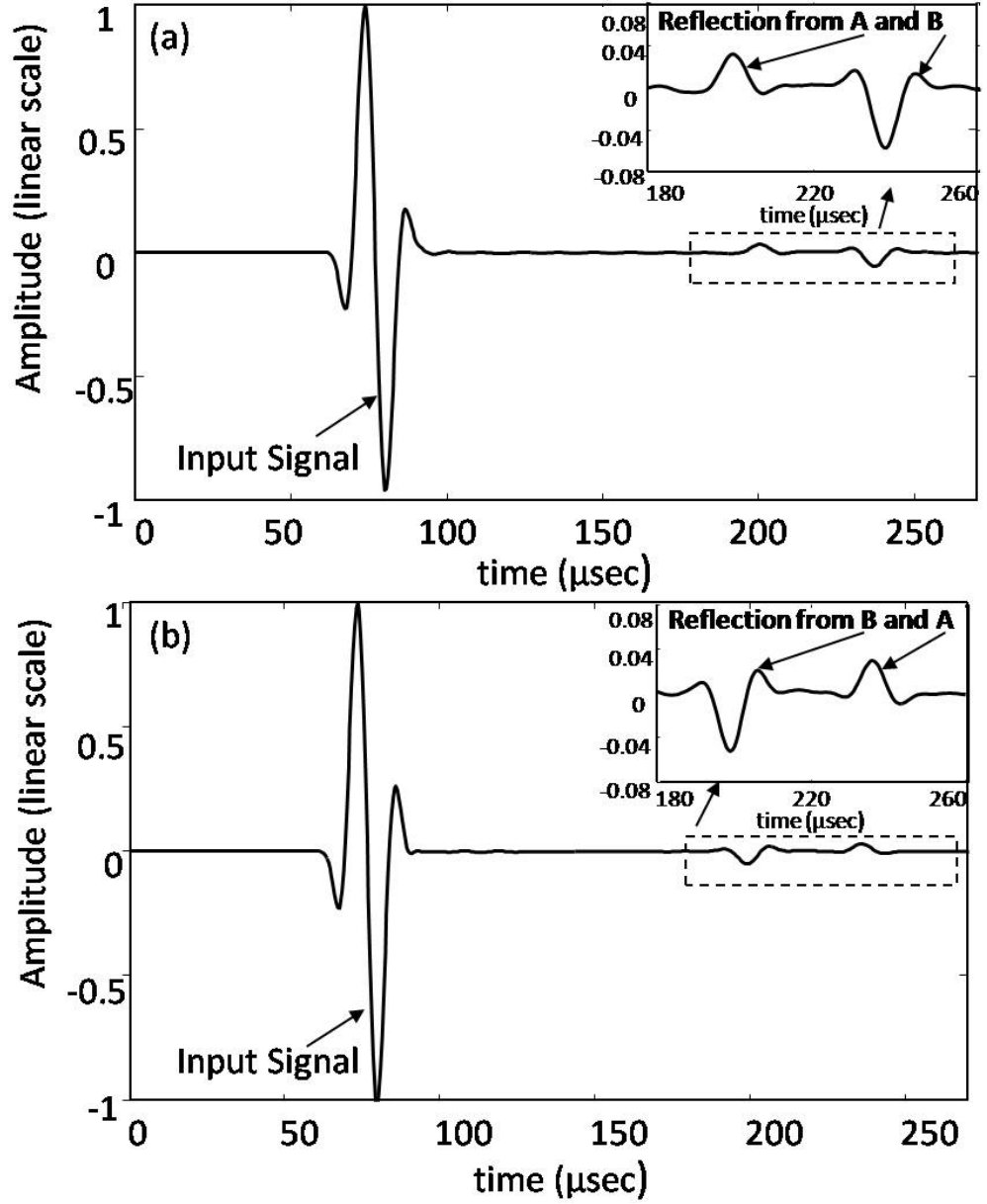
Figure 3.2: *Time domain signal for a 5.5mm wall thickness- 76.2mm outer diameter steel pipe with 50% thickness tapered step-down (a) and step-up (b) - Centre frequency is 70kHz; the taper is 0.06m long and the slope of the taper is 2.62°.*
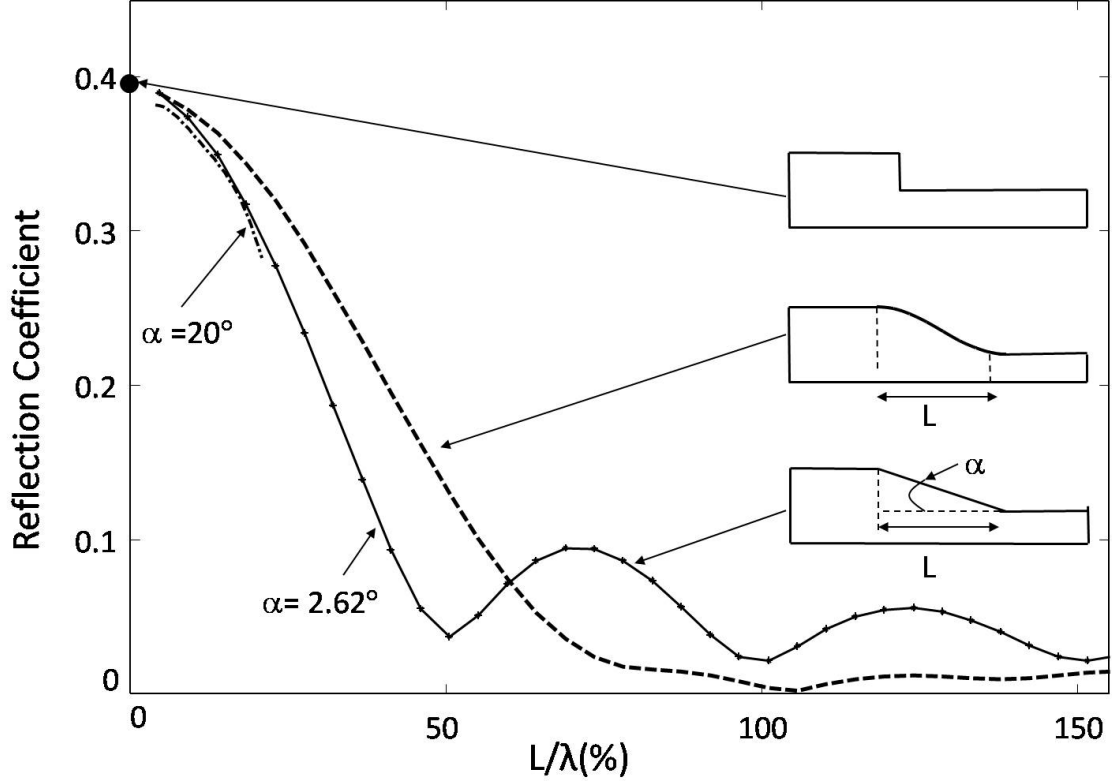
Figure 3.3: *Reflection coefficient for 50% depth sharp, cosine and linear down-steps.*

In the case of the tapered step, the reflection behaviour varies periodically with the ratio L/λ. At very low values of L/λ, the RC from the tapered step tends to the RC from the sharp step. As L/λ increases, the RC oscillates periodically due to the interaction between the waves reflected from the two ends of the taper. The RC of the tapered step can be approximately expressed as

$$RC(f) = R_1(f) + R_2(f) \cdot e^{i(\Delta\phi)} \tag{3.2}$$

where R_1 and R_2 are the ratio of the modulus of the first (R_1) and the second (R_2) reflections from the step to the amplitude of the incident wave. Their frequency dependence is shown in Fig. 3.4. Equation (3.2) ignores all the reverberations from the two ends of the taper which are are very small. $\Delta\phi$ is the phase difference between the waves reflected from the two ends of the taper and is given by

$$\Delta\phi = 2kL + \pi = \pi \cdot (\frac{4L}{\lambda} + 1) \tag{3.3}$$
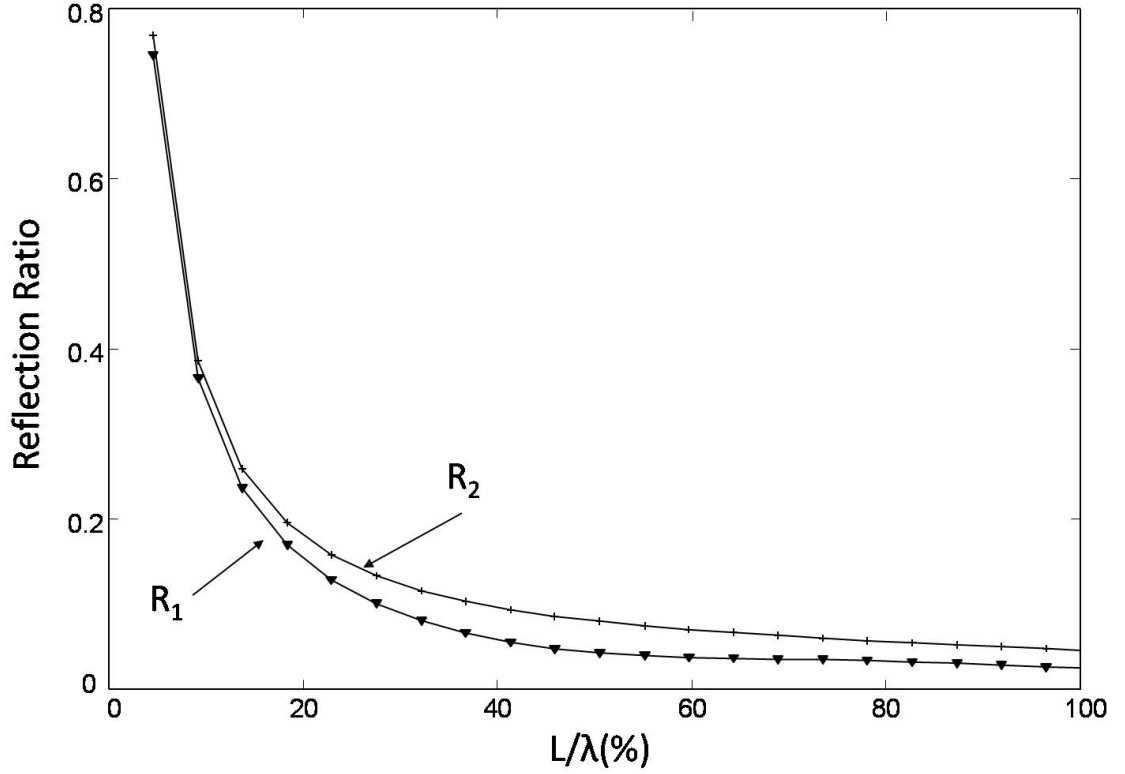
Figure 3.4: *Ratio of the modulus of the first (R_1) and the second (R_2) reflections to the amplitude of the incident wave.*

The addition of π is due to the fact that the reflection from the two ends of the taper are out of phase, as discussed above. The two waves interact destructively if $\Delta\phi = (2n + 1)\pi$ and constructively if $\Delta\phi = 2m\pi$, where n and m are integers. Figure 3.3 shows that at $L/\lambda = 50\%$ (n=1), 100% (n=2) and 150% (n =3), minima of the RC occur, and at $L/\lambda = 75\%$ (m =2), 125% (m =3) maxima are seen. However, no maximum can be seen at $L/\lambda = 25\%$ (m=1). This is because, as shown in Fig. 3.4, the amplitudes of the reflections from the two ends of the taper increase rapidly as the frequency decreases, when the value of L/λ drops below 25%. In this range, the behaviour of the overall reflection coefficient is dominated by the frequency dependence of the magnitudes of the reflections from the two ends of the taper, rather than the interference phenomenon. Therefore the overall reflection coefficient continues to increase, even though the interference between the reflections is not perfectly constructive.

A tapered step with a taper slope of 20° was then modelled and analyzed in order to understand the effect of taper angle on the reflection behaviour. The pipe had a total length of 0.41m and a taper was located 0.2m from the left hand end, the length of the taper being 7.55mm; both up- and down- steps were simulated. Figure 3.3 shows that the reflection coefficient curves from the 20° tapered down-step superposes that for a 2.62° tapered down-step within the range of comparison; therefore for a given maximum depth, the reflection from tapered steps is only a function of the ratio of the step length to the wavelength, whatever their slope. Figure 3.3 shows also that the reflection coefficient spectrum from the cosine tapered step initially decreases more gradually with frequency than that from the linear step, but subsequent maxima are very small and the reflection is below 2.5% for $L/\lambda > 75\%$.

In order to study the mode shapes in the taper region through the thickness of the pipe, the tangential displacements at different radial positions were monitored at three different locations inside the taper (points 3, 4 and 5 in Fig. 3.1a). Figure 3.5 shows the variation of the amplitude of the signals recorded at these points inside the taper with radial position (r) at a frequency of 50 kHz for the down-step case. The mode shapes at points 1 and 2 outside the taper are also plotted for comparison. It is evident that the mode shape of the T(0,1) wave packet travelling in the taper region preserves the linear relationship with radial position seen in the constant thickness region. The time-averaged axial energy flow (EF) of the T(0,1) mode was also calculated at the three locations in the taper. It can be expressed as [67]

$$EF(\omega) = \frac{\pi \mu \omega^2}{V} \int_{R_I}^{R_O} (|U_r(\omega)|^2 \cdot r) dr \tag{3.4}$$

where V is the phase velocity, μ is the second Lamé constant and ω is the angular frequency. The quantity $U_r(\omega)$ is the amplitude of the signal at the radial position (r) at each frequency (ω); R_I and R_O are the inner and outer radii of the pipe. The phase velocity (V) is constant in the taper since the T(0,1) mode is non dispersive. The calculated EF at the three monitoring points (shown in figure 3.5 in arbitrary units because only the relative values are of interest) are constant to within numerical
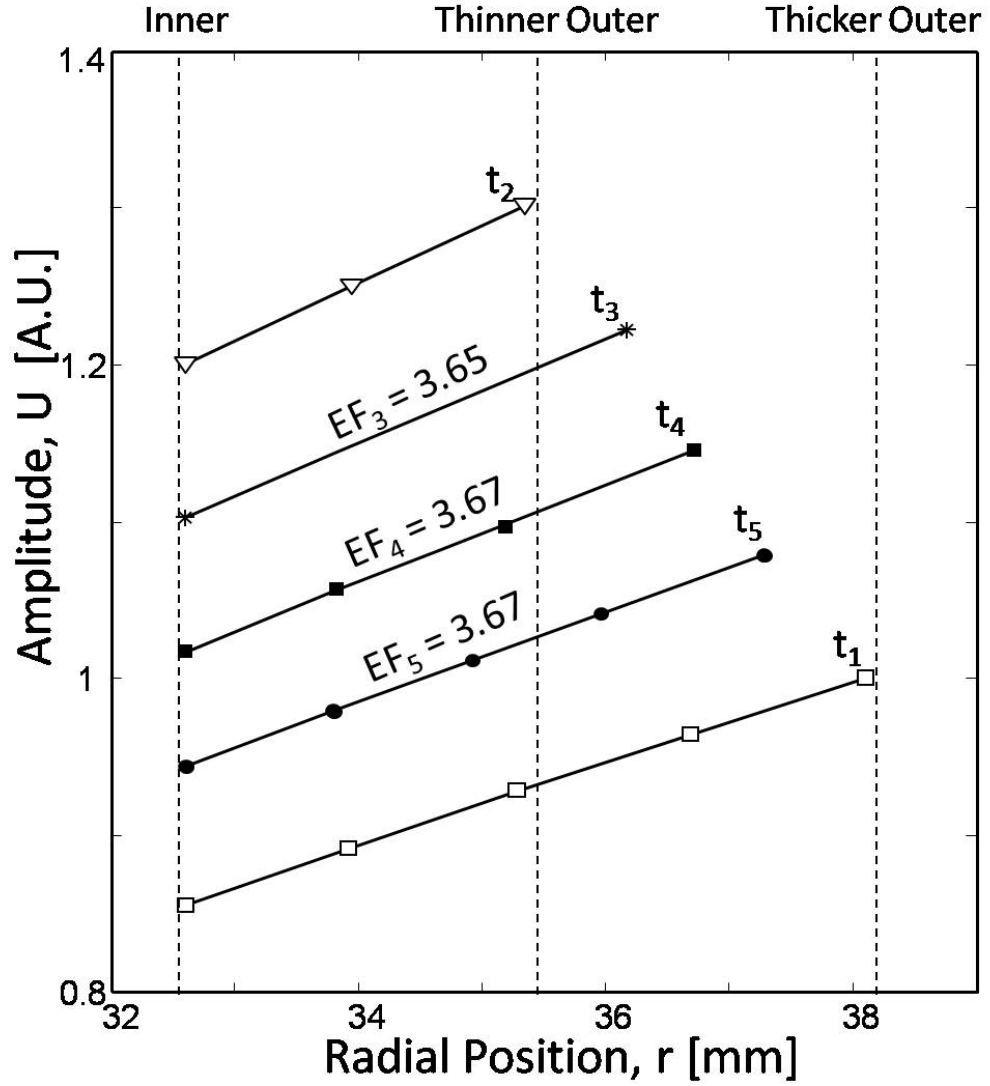
Figure 3.5: *Mode shapes through the thickness of the 50% depth tapered step at frequency of 50kHz. As reference, the Energy flow (EF) at point 1 and 2 are respectively 3.70 and 3.63. The values of the EF at each location of the taper are displayed in arbitrary units.*

rounding errors, confirming that there is no reflection of energy within the tapered section.

3.2.2 Tapered notches

The modelling of both tapered defects (Fig. 3.1c) and V-notches (Fig 3.1d) was conducted on a 0.5m long steel pipe model. In both cases the discontinuities were

introduced at 0.3m from the excitation end of the pipe. The scattering behaviour from tapered defects with 20% and 50% depths was analyzed. For each of these depths, several configurations of the defect were studied by changing the slope angles of the tapered regions; table 3.1 summarises the FE simulations performed.

The reflection coefficient (RC) spectra of the T(0,1) mode from tapered defects with 20% and 50% maximum depths are shown respectively in Figs 3.6a and 3.6b. In each case, tapered notches with different slopes were studied. The periodic behaviour seen in Fig. 3.6 has previously been studied in the rectangular ($\alpha = 90°$) notch case [25, 30] and is due to the interference of the reflections from the front and back of the notch. Maxima of the reflection coefficient occur at frequencies when the length of the notch is an odd multiple of a quarter wavelength, while minima occur at frequencies when the length of the notch is multiples of a half wavelength.

Figures 3.6a and 3.6b show that when the length at the midpoint of the tapered defect is taken as the characteristic length (L_e), the reflection coefficient from tapered notches follows the same form as that from a rectangular notch. The exact frequency location of the maxima, and particularly the minima, is slightly affected by the slope of the taper, especially for the deeper defect (Fig. 3.6b). As expected, the reflection coefficient from the deeper defect (Fig. 3.6b) is greater than that from the shallower defect (Fig. 3.6a). The amplitude of the first maximum of the reflection coefficient is only slightly affected by the slope of the taper, but the amplitude of the second peak is greatly reduced as the taper becomes gradual. This mirrors the reflection behaviour from a tapered step discussed earlier and has important implications for practical inspection; it suggests that tapered defects will be more difficult to detect at higher inspection frequencies, so indicating that increasing the inspection frequency does not necessarily give better sensitivity to defects.

A V-notch (Fig. 3.1d) can be considered to be a tapered defect with no flat-bottomed region. Two V-notches with different slopes (10° and 20°) were modelled, the maximum depth being 50% in each case. Figure 3.7 shows the reflection coefficient spectra for the V-notches, together with those for tapered defects with the same slopes. The predictions for V-notches are shown over a limited range of L_e/λ. This

	Depth = 20%thickness	Depth = 50%thickness
$\alpha(°)$	a[mm]	a[mm]
11	46	54
20	43	48
30	42	45
45	41	43
90	40	40

Table 3.1: *Summary of the FE models for tapered defects in pipe wall thickness 5.5mm, L_e is 40mm.*

is because by increasing the slope of the taper (α), the axial extent (L_e) of the V-notch decreases at a fixed depth of the defect. In order to predict the reflection behaviour at high values of L_e/λ, a high excitation frequency is required. The predictions for V-notches are therefore limited by the cut-off frequency of the T(0,2) mode. The peak reflection coefficient for the V-notches is consistently lower than that for the tapered defects with the same slope. This is probably because in the tapered defect case the inhomogeneous waves generated at the bottom of the down-taper die away over the flat-bottomed region and so do not interact with the start of the up-taper, whereas in the V-notch case the up-taper starts at the end of the down-taper so interaction of inhomogeneous waves is significant. Demma *et al* [25] observed a similar phenomenon as a rectangular notch evolves to a crack. The crack case was also predicted by FE analysis and is shown in Fig. 3.7; the result is consistent with the crack case presented in [25]. It is interesting that the peak reflection coefficient from the V-notches modelled here is intermediate between the crack case and the tapered defects considered earlier.
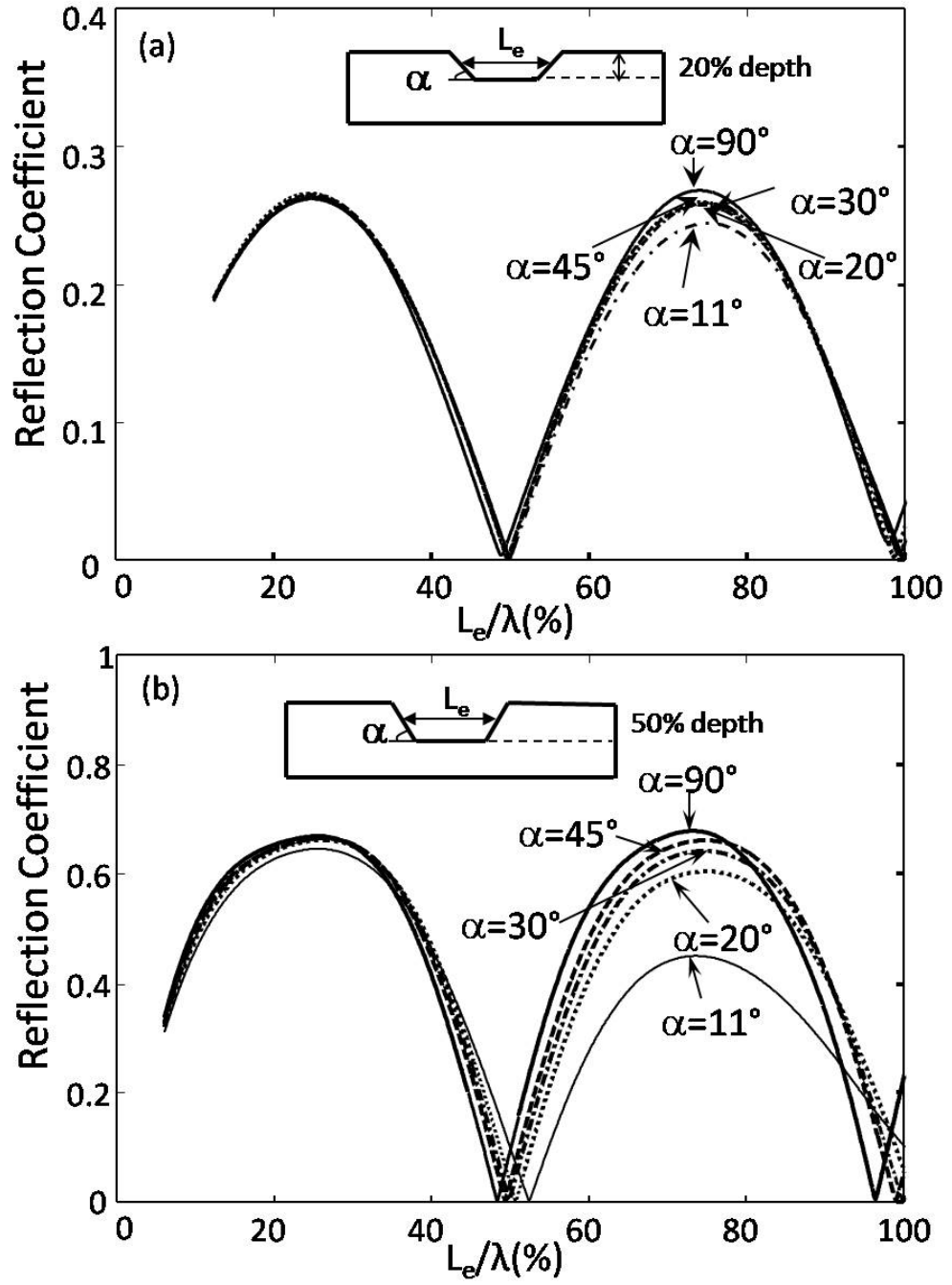
Figure 3.6: *Variation of the T(0,1) mode reflection coefficient with the ratio of the axial extent of tapered defects to the wavelength. Results are for a 3 inch steel pipe with notches (a) 20% and (b) 50% maximum depth.*
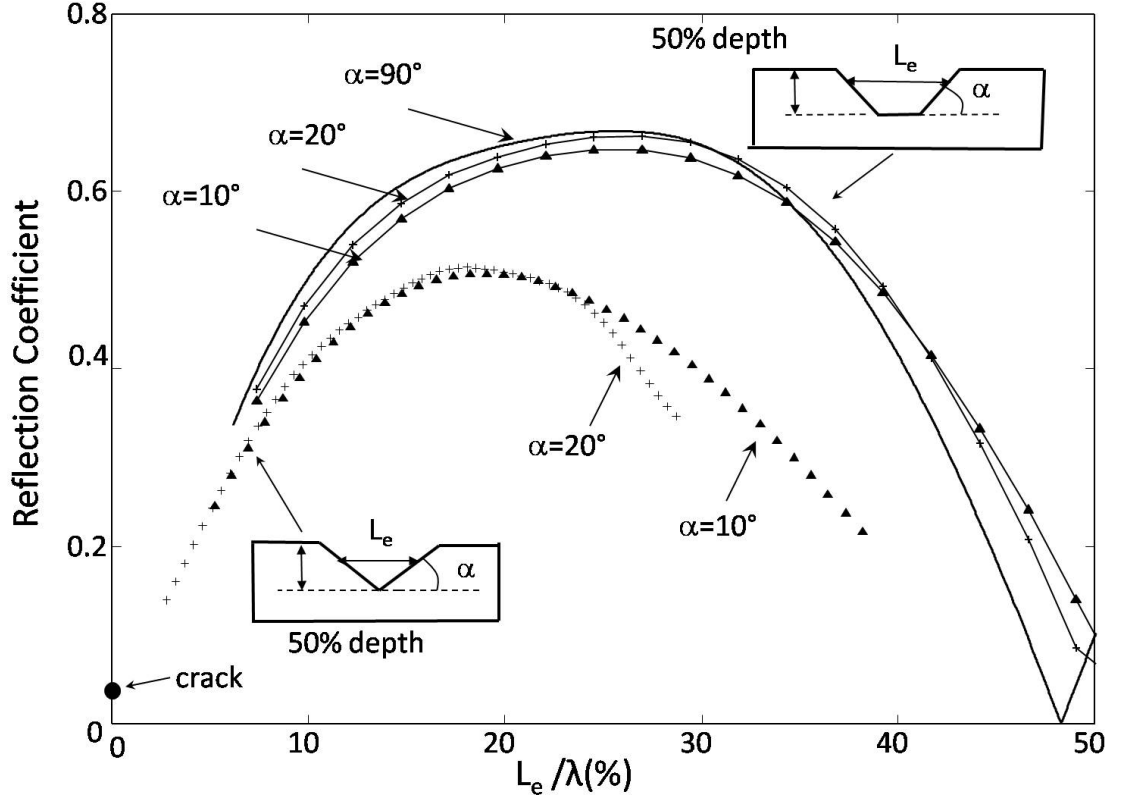
Figure 3.7: *Comparisons of the reflection coefficient spectrum from V-notch and tapered defects with different slopes of the tapered regions.*

3.3 Semi-Analytical prediction of reflection coefficient from tapered defect (Superposition Approach)

The FE predictions of the scattering characteristics of the T(0,1) mode from tapered steps presented in section 3.2.1 are used in this section to reproduce analytically the reflection from a tapered defect (see Fig. 3.1c). As a wave interacts with this defect, a series of reflections is produced, decreasing in magnitude with the number of times the wave traverses the defect region. The analytical method adopted in this section assumes that T(0,1) is the only mode propagating along the pipe and neglects the effect of non propagating modes. The RC behavior from a tapered defect is reconstructed by adding together the consecutive reflections from the two
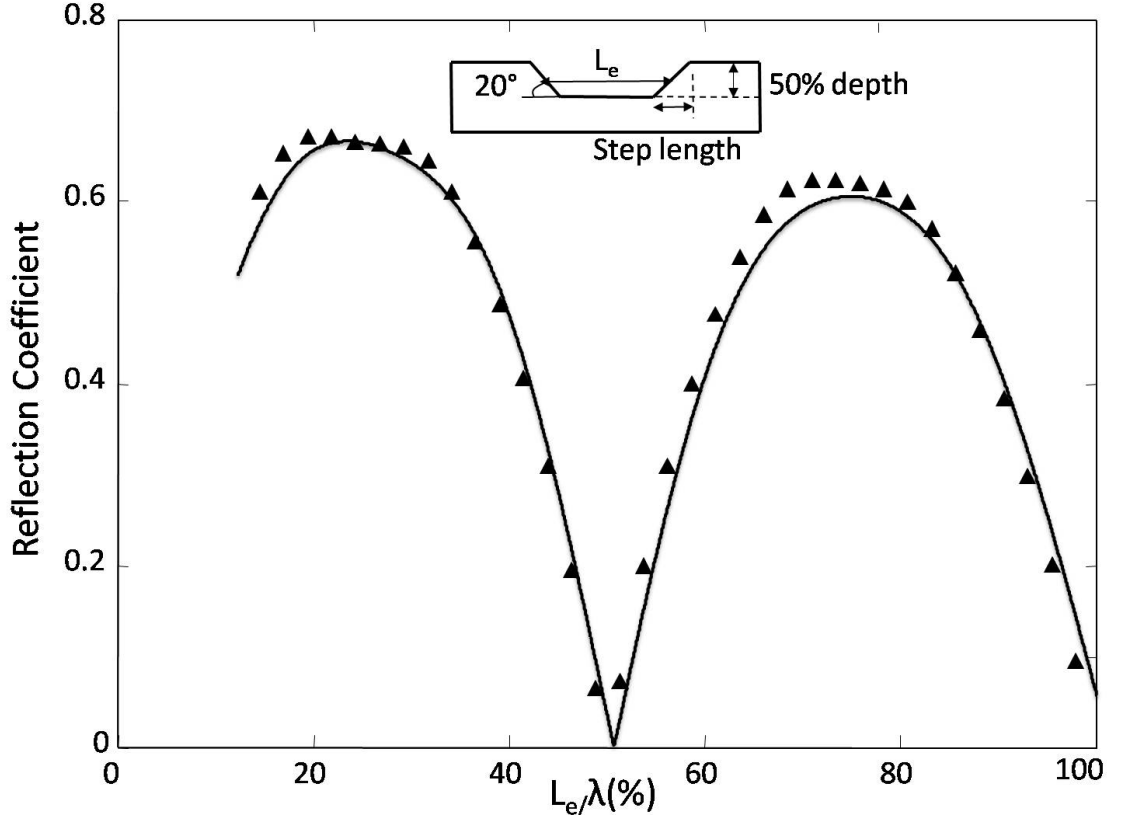
Figure 3.8: *Comparison of reflection coefficient for tapered defect from FE modeling (continuous line) and semi-analytical superposition model (triangular points). The slope of the taper regions is 20°.*

ends of the discontinuity. This methodology has already been applied successfully to reproduce the RC from rectangular notches in both plates [25] and pipes [30]; in both cases the defect was seen as a sharp down-step and up-step separated by a flat-bottomed zone. The basis of this approach is to consider the defect as composed of three different regions, each of them with its own reflection and transmission characteristics. In the case of the tapered defect in Fig. 3.1c, part A is a tapered step-down and its reflection and transmission coefficients are respectively R_A and T_A; part B is a flat bottomed region. The third part (C) is a tapered step-up and its reflection and transmission coefficients are R_C and T_C as shown in Fig. 3.1c. The modulus of the reflection and transmission coefficient from tapered down- and up-steps has been obtained in section 3.2.1. As the tapered step has a finite length and the T(0,1) wave packet is only reflected at two ends of the taper, the midpoint

along the length of a taper is taken as the effective centre of the step (E_A and E_C). Considering the T(0,1) mode is incident from the left end of the pipe (Fig. 3.1c) the reflection and transmission at part C is time delayed compared to part A; the delay can be approximed by the time for the wave to travel between the effective centres of the two tapers (L_e in Fig. 3.1c).

As the input signal travels from one end of the pipe, it meets the first discontinuity (part A) and is partly reflected back (R_A) and partly transmitted (T_A). After that the transmitted signal (T_A) passes through the second region and interacts with the third region, the tapered up-step, where the wave is part reflected back (R_C) and the remaining part is transmitted (T_C). The reflection R_C then partially transmitted at the front of the defect and partially reflected to produce a series of reverberations. Thus, by assuming that the two ends of the defect have the same dimensions, the modulus and phase of the second reflection are

$$|R_2| = |T_A \cdot R_C \cdot T_C| \qquad (3.5)$$

$$\phi_2 = 2L_e k + \pi = \pi \cdot \left(\frac{4L_e}{\lambda} + 1\right) \qquad (3.6)$$

The additional π takes into account the sign reversal between the reflection coefficients from the step-down and step-up caused by the different changes in impedance in the two cases. Applying the same procedure for successive reflections, it is found that the amplitude and the phase of the jth reflections from the tapered defects are

$$|R_j| = |T_A \cdot (R_C)^{2j-3} \cdot T_C| \qquad (3.7)$$

$$\phi_j = 2jkL_e + \pi = \pi \cdot \left(\frac{4jL_e}{\lambda} + 1\right) \qquad (3.8)$$

Thus, the total reflection coefficient from a tapered defect is expressed as

$$R_{tot} = \sum_j R_j = R_1 + R_2 + R_3 + \ldots + R_i \qquad (3.9)$$

where the components R_j are defined through their amplitude and phase,

$$R_j = |R_j| e^{i(\phi_j)} \qquad (3.10)$$

Figure 3.8 shows the comparison between the RC obtained from the FE simulations and the RC obtained from the superposition approach for a tapered defect with a taper slope of 20°. The two curves show very good agreement.

3.4   Experimental Validations

In order to validate the FE predictions, laboratory experiments were performed on a set of nominal 3 inch steel pipes (outer diameter 76.2 mm, wall thickness 5.5 mm) to determine the sensitivity of the torsional T(0,1) mode to a series of tapered defects (see Fig. 3.1c). These tapered defects were machined with different slopes of the tapers, the maximum depth of the defect being 50% of the thickness. In order to cover the L_e/λ range 0.1-1 on the reflection spectrum, three different maximum axial extents (a in Fig. 3.1c) of tapered defect were selected: 15, 28 and 45 mm. This was necessary because the instrumentation used was limited to a relatively narrow frequency range (25-90 kHz) so it was not possible to cover the full range of defect axial extent/wavelength simply by changing the frequency at a single length. Three pipes were therefore used for these experiments; in each pipe the first cut was the one with lowest slope angle, then the slopes of the tapers, and consequently the equivalent axial extent, were increased. Table 3.2 summarizes the dimensions of the defects tested in the three pipes, A B and C.

The experimental setup is shown schematically in Fig. 3.9. The pipes were 2 m long and defects were machined at 0.8 m from the right end using a milling machine. The cutter axis was inclined with respect to the radial axis of the pipe in order to create the tapered regions, and rotating the pipe about its own axis created axi-symmetric defects. The pipe was tested horizontally; it was rested on two steel supports, which produced a negligible reflection of the ultrasonic signal. The T(0,1) mode was excited at the left end of the pipe by using a standard Guided Ultrasonics Ltd. transducer ring consisting of equally spaced piezoelectric transducers which applied alternating forces to the external wall of the pipe in the circumferential direction. The ring was removed after every test in order to machine a new defect.

A Guided Ultrasonics Ltd. [7] G3 Wavemaker instrument was used to generate a 5 cycle Hanning windowed tonebust at several frequency values from 25 to 70 kHz. The propagating waves were detected by a fibre optic vibrometer (Polytec FV 2700) focused on the pipe at 0.6m from the left end; the in-plane displacements were monitored by focussing the two beams at 30° to the pipe axis [118]. The received signal was amplified and transferred to a digital oscilloscope (Le Croy 9400), and then to a PC for processing and display. For each frequency the signal was recorded at four points symmetrically located around the circumference of the pipe, these signals were summed in order to remove the non-symmetric modes. In order to improve the signal-to-noise ratio, 20 successive response signals were captured by the digital oscilloscope and averaged.
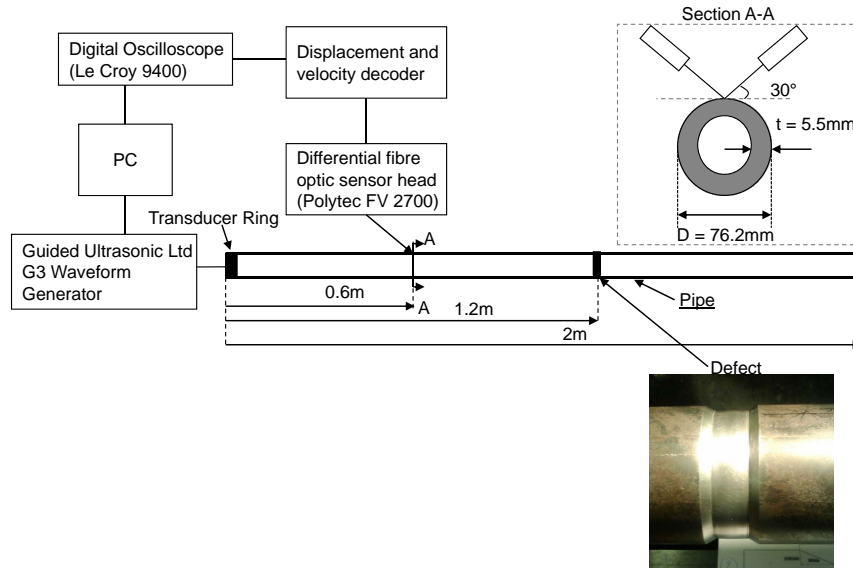
Figure 3.9: *Schematic representation of the test set-up.*

Figure 3.10 shows the comparison between Finite Element (FE) predictions and experiments for 50% depth tapered defects and a V-notch, the taper slopes being 11°. Good agreement between the FE predictions and tests results is shown; the
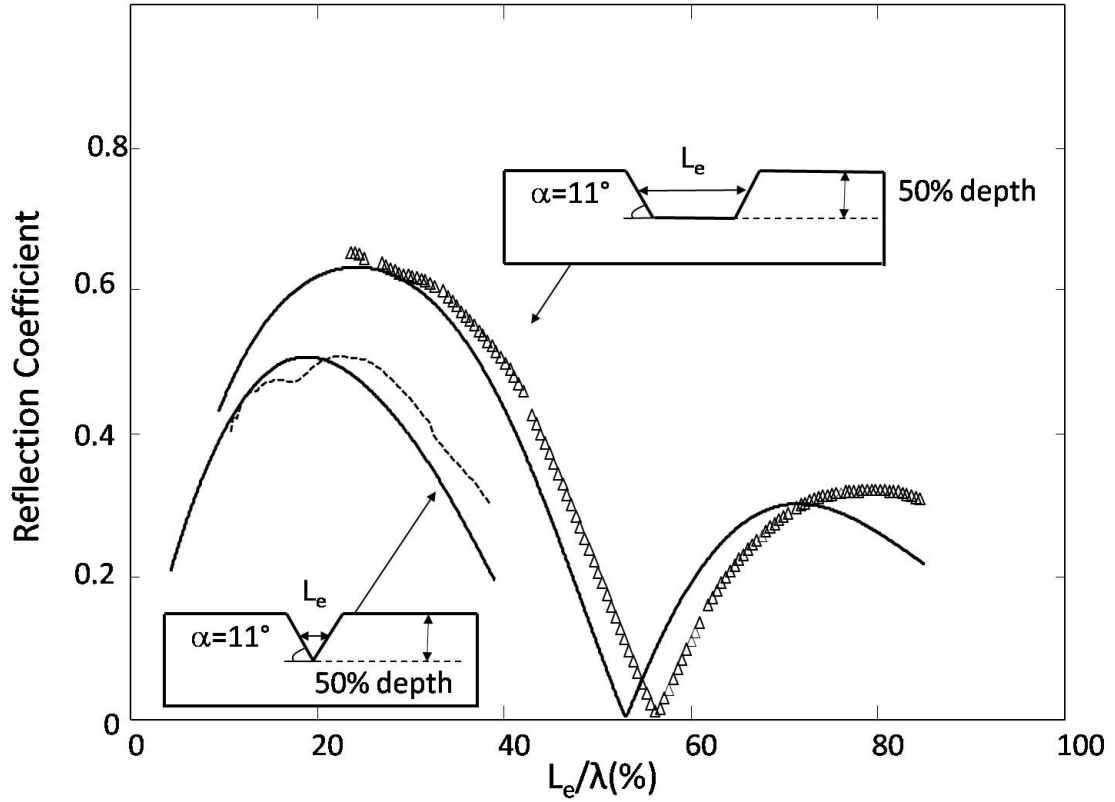
Figure 3.10: *Finite Element predictions (solid line) and measurements (points) of the reflection coefficient from tapered defects with taper slope angles of 11°.*

small shift in the position of the minimum is due to an error lower than 5% in the axial extent of the machined defect. This error consequently affects the location of the second peak of the reflection, which occurs at frequencies higher than predicted. It is particularly interesting to note the experimental confirmation of the lower RC peak at $L_e/\lambda = 75\%$ compared with that at $L_e/\lambda = 25\%$; this confirms the predictions of Fig. 3.6b. The lower peak value of the RC from the V-notch compared to that from the tapered defect shown in Fig. 3.8 is also validated.

Figures 3.11a and 3.11b show the comparisons of the reflection coefficients from tapered defects, with respectively 30° and 45° taper angles, obtained from FE predictions and tests. In both figures the letters A, B and C refer to the pipes of table 3.2. Some values of the abscissa L_e/λ are obtained in tests on more than one of the pipes of table 3.2. There is generally quite good agreement between the measurements and the predictions, particularly for pipe C. The reflections from pipe B in
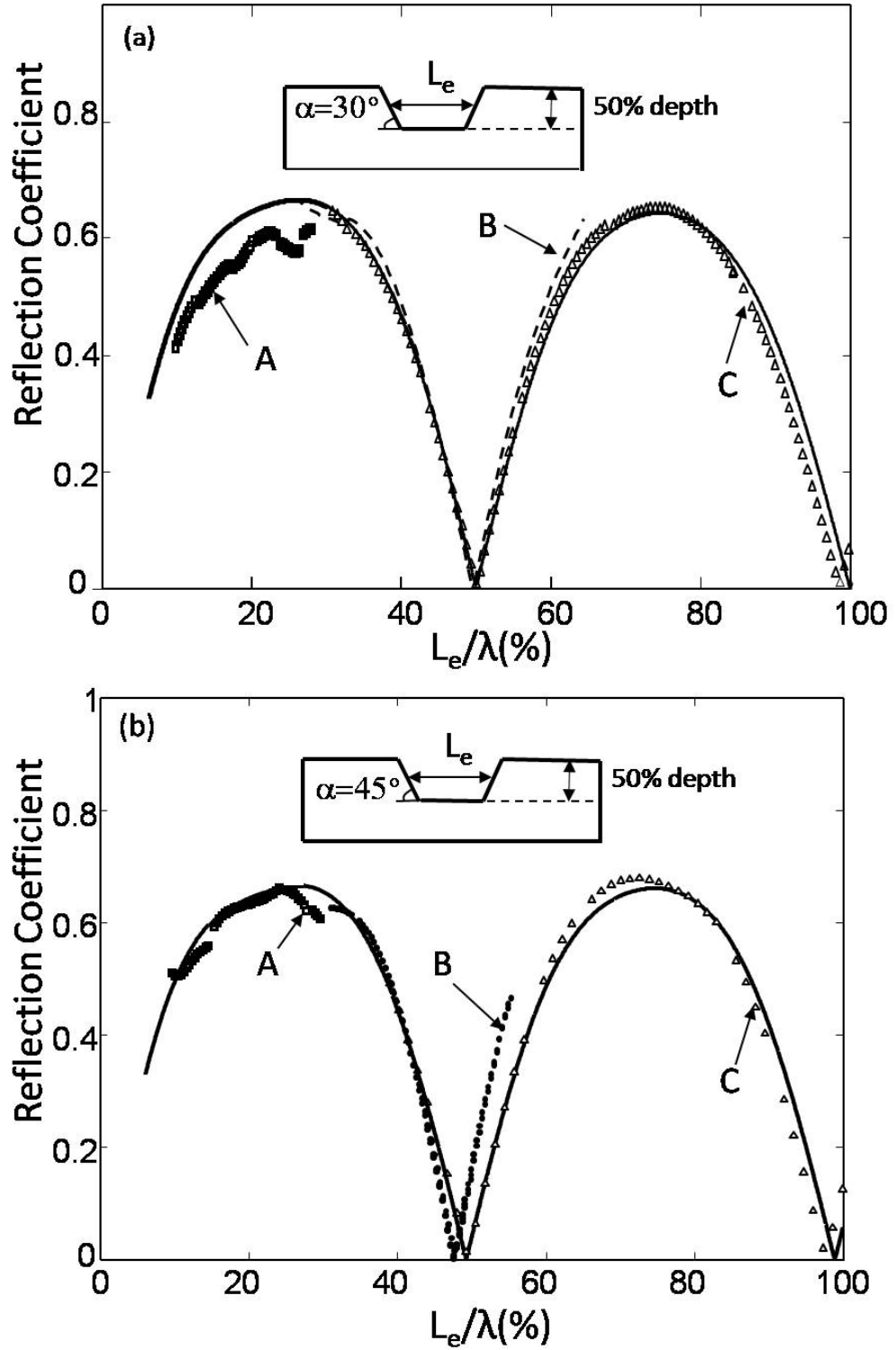
Figure 3.11: *Predictions (continuous line) and measurements with pipes A, B and C of the reflection coefficient from tapered defects with taper slope angles of (a) 30°, (b) 45°.*

Fig. 3.11b are larger than the predictions; this was found to be due to the intended defect depth being exceeded. The results on the different pipes follow the same

Pipe	a[mm]	$\alpha(°)$	L_e[mm]
A	15	30	10.2
		45	12.3
B	28	11.1	14.0
		30	23.2
		45	25.3
C	45	11	30.8
		30	40.2
		45	42.3

Table 3.2: *Summary of dimensions of the defects tested in 3 inch pipes. The depth of the defect was 50% of the thickness in all cases.*

curve as a function of L_e/λ, so confirming that this is the controlling parameter.

3.5 Conclusions of the scattering analysis from 2D defects with varying depth profile

In this chapter a study of the reflection of the fundamental torsional mode T(0,1) from an axi-symmetric notch with varying depth profile has been carried out via finite element (FE) modelling and experimental validation. A study of the reflection from a tapered step showed that reflections are generated at the two ends of the taper; there was no evidence of reflections from inside the tapered region. These two reflected waves are out of phase, the phase shift always occurring at the lower thickness end of the taper. The overall reflection coefficient from a tapered step varies periodically as a function of the ratio of the step length to the wavelength. The largest reflection is seen at low values of the ratio, corresponding to a sharp step at low frequencies. The mode shape inside the tapered region is similar to that in a uniform pipe. The reflection behaviour from a cosine tapered step is similar to that

from a linear taper, the main reflection being seen at low frequencies; subsequent maxima due to interference effects are much less evident than in the case of a linear taper.

A semi-analytical method (superposition approach) was successfully applied to reconstruct the reflection coefficient of a tapered defect by using the reflection and transmission characteristics of tapered up- and down- steps. A study of tapered defects with different depths and slopes of the tapered zones was carried out. These predictions showed that the reflection coefficient from tapered notches follows the same form as that from a rectangular notch if the characteristic length of the tapered notch is taken as its average length. At a given taper angle, the amplitude of successive reflection coefficient peaks decreases as the frequency increases. Therefore tapered defects are expected to be more difficult to detect at higher inspection frequencies. This effect is more evident for shallower tapers. This study has considered defects in which the up- and down- steps have the same slope. More complex geometries are reported in the next chapter.

A comparison between the reflection from a defect with a flat bottomed region between the tapers (tapered defect) and a defect with the two steps directly connected (V-notches) showed that the reflection from a V-notch is consistently lower than that from a tapered defect of the same depth. This is probably due to inhomogeneous modes generated by the down-step of the V-notch interacting with those from the up-step. A similar effect has previously been seen as a rectangular notch degenerates to a crack.

Chapter 4

Scattering from complex defects in pipes

4.1 Introduction

In this chapter a numerical study of the reflection of the fundamental torsional mode T(0, 1) from three dimensional (3D) defects in pipes with different shapes is carried out. In section 4.2, simple flat-bottomed defects with different surface profiles are analyzed, and then the reflection from 3D defects with varying depth profile is studied. The influence of the depth profile of a more complex defect in the axial and circumferential directions on the reflection coefficient is also analyzed. The results from the above analyses are then used in section 4.2.1 to propose a practical approach to determine the maximum depth of a complex discontinuity from the reflection coefficient behaviour. In the following section the method is applied to real corrosion patches and the limitations of the method are determined. An experimental validation of the numerical simulations is presented in section 4.4 of this chapter.

4.2   Simple defects in pipes

The main purpose of this analysis is to find the key parameters that influence the reflection coefficient spectrum from simple shaped defects. 3 inch schedule 40 steel pipes (5.5 mm wall thickness) are considered in the frequency range below the cut-off frequency of the T(0,2) mode. As mentioned in section 2.7.1, a 3D solid FE model was adopted in Abaqus to study the interaction between the T(0,1) mode and both axi-symmetric and 3D defects. Linear elements with Δx of 1.8 mm were used for these simulations, which converged with a time step Δt between 0.01-0.05 μsec depending on the complexity of the geometry of the defect. Figure 4.1 shows the variation of the reflection coefficient (RC) from axi-symmetric rectangular defects as a function of the ratio of the axial extent of the defect (L) to the wavelength (λ). The periodic variation of the RC is governed by the axial extent of the defect while the peak value of the RC is dependent on the maximum depth of this 2D discontinuity. These results agree with past work [22, 34, 38]. Figure 4.2 shows the variation of the first peak in the reflection coefficient spectrum as a function of the maximum depth of axi-symmetric defects expressed as a percentage of the wall thickness of the pipe. It is interesting to note that the peak reflection coefficient is a linear function of defect depth up to a depth of around 75% of the wall thickness.

The interaction of the input T(0, 1) mode with defects with different surface and depth profiles with a maximum depth of 25, 50 and 75% of the thickness was then simulated and the RC spectrum for each of them was determined. Figure 4.3 shows depth profiles in the circumferential plane and surface configurations of the discontinuities analyzed in this section. As mentioned above, the goal of these simulations is to understand the effect of different shaped defects on the RC spectrum. This study starts with the simulation of six simple flat-bottomed defects with rectangular and circular surface profiles and different axial extents (L) (see defects a.1 and a.2 in Fig. 4.3). FE models of defects with more complex depth profiles such as ellipsoidal or tapered shapes (defects b and c respectively in Fig. 4.3) were then created with different surface configurations. In order to analyze discontinuities more similar to real corrosion patches, random multilayered defects with a predominant dimension
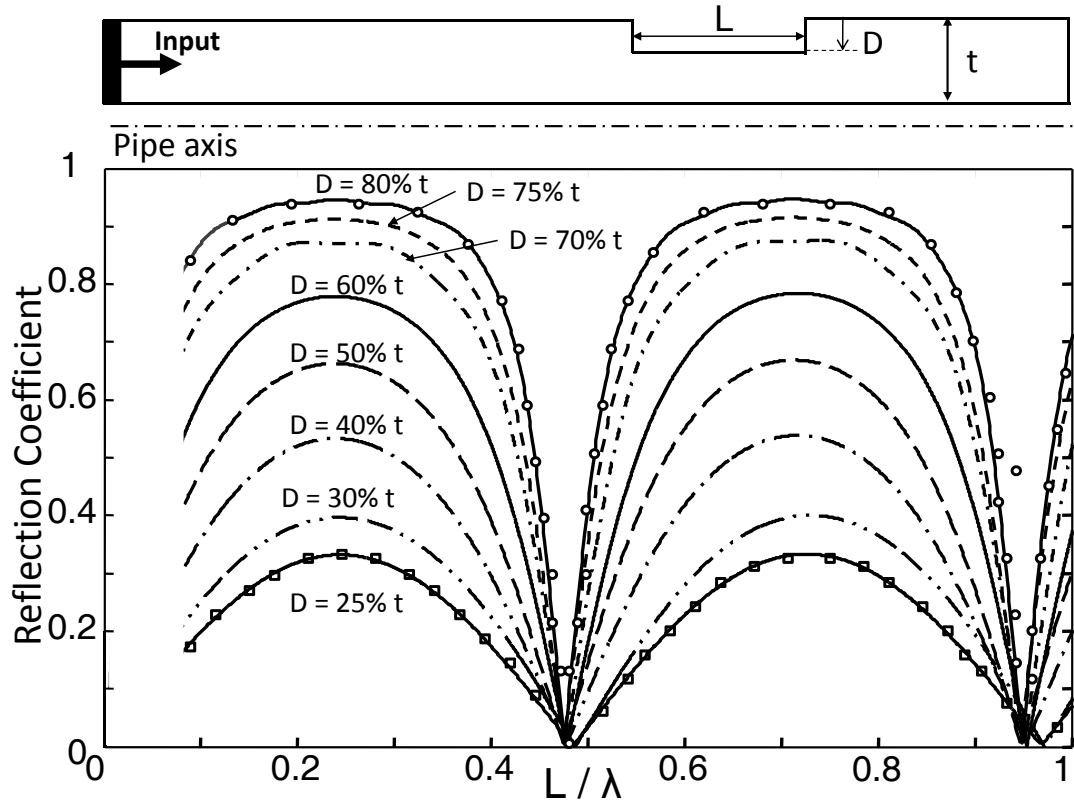
Figure 4.1: *Variation of the modulus of the T(0,1) mode reflection coefficient from axi-symmetric defects in pipes with the axial extent (L) of defect divided by the wavelength (λ) for different depths of the defect.*

in the axial direction of the pipe (see defects d.1 and e.1 in Fig. 4.3) and in the circumferential direction (see defect d.2 and e.2 in Fig. 4.3) were created in Solidworks and simulated in Abaqus. The effect of the location of the maximum depth of the defect on the RC spectrum was also analyzed by simulating random multilayered defects with their maximum depth profile located at different positions along the axial and circumferential direction (see defects d and e in Fig. 4.3).

Figure 4.4 shows the variation of the value of the maximum peak of the reflection coefficient spectrum from defects of Fig. 4.3 (their maximum depth (D) being 50% of the thickness) with the ratio of their circumferential extent to the outer circumference of the pipe (πOD, where OD stands for outer diameter); this ratio is unity when the defect is axi-symmetric. When the defect depth was non-uniform in the circumferential direction (i.e. all cases where the defect was not flat-bottomed), the
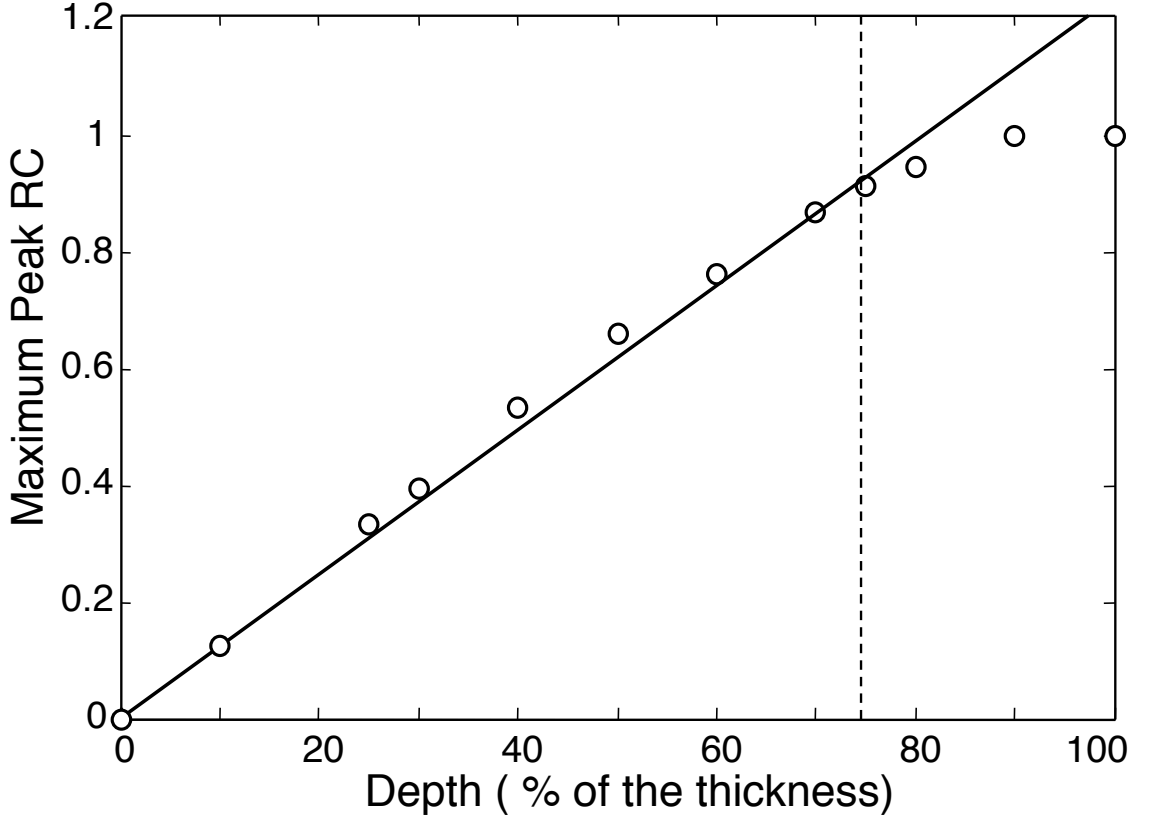
Figure 4.2: *Variation of the maximum peak of the reflection coefficient from axisymmetric rectangular defects with the maximum depth of the defect expressed as a percentage of the wall thickness of the pipe.*

profile in the circumferential direction was approximated as a V-notch. Therefore the equivalent circumferential extent (C_{eq}) shown on the x-axis in Fig. 4.4, defined as the geometric average circumferential extent of the defect [30], is half of the surface circumferential extent of the feature. It interesting to see that a linear approximation fits reasonably well with the simulated results; this means that at a fixed depth of the defect, the maximum of the RC is directly proportional to the ratio of the equivalent circumferential extent of the defect to the outer circumference of the pipe, and is independent of the shape of the defect. In addition, different markers are used in Fig. 4.4 to represent defects with the same shape but different axial extents; therefore it is evident that variation of the axial extent of the defect has only a small effect on the magnitude of the maximum peak of the reflection coefficient in the frequency domain, the error range being ±9%. (The frequency at which the peak

	Section profile of the defect	Surface profile of the defect		
a	t; C; $D = n*t$ — 1	C; L — 1	L = 16mm △ L = 32mm ○ L = 64mm □	A; C — 2	L = 16mm ▲ L = 32mm ● L = 64mm ■
b	t; C; $D = n*t$	L; C	L= 28mm C = 23mm ◇ L = 16.5mm C =21.75mm ◆		
c	t; α; $D = n*t$	C; L — 1	α= 30º 16x16mm +	L; C — 2	32x32mm α= 30º ▽ 32x32mm α= 40º ▼ 32x16mm α= 30º ▷ 32x16mm α= 40º ▶ 16x32mm α= 30º ◁ 16x32mm α= 40º ◀
d	t; D/2; $D = n*t$	C; L — 1 ◇ L = 46mm C = 28mm	C; L — 2 ☆ L = 38mm C = 70mm		
e	D/2; t; $D = n*t$	L = 46mm C = 28mm C; L — 1 ◆	L; C — 2 ★ L = 38mm C = 70mm		
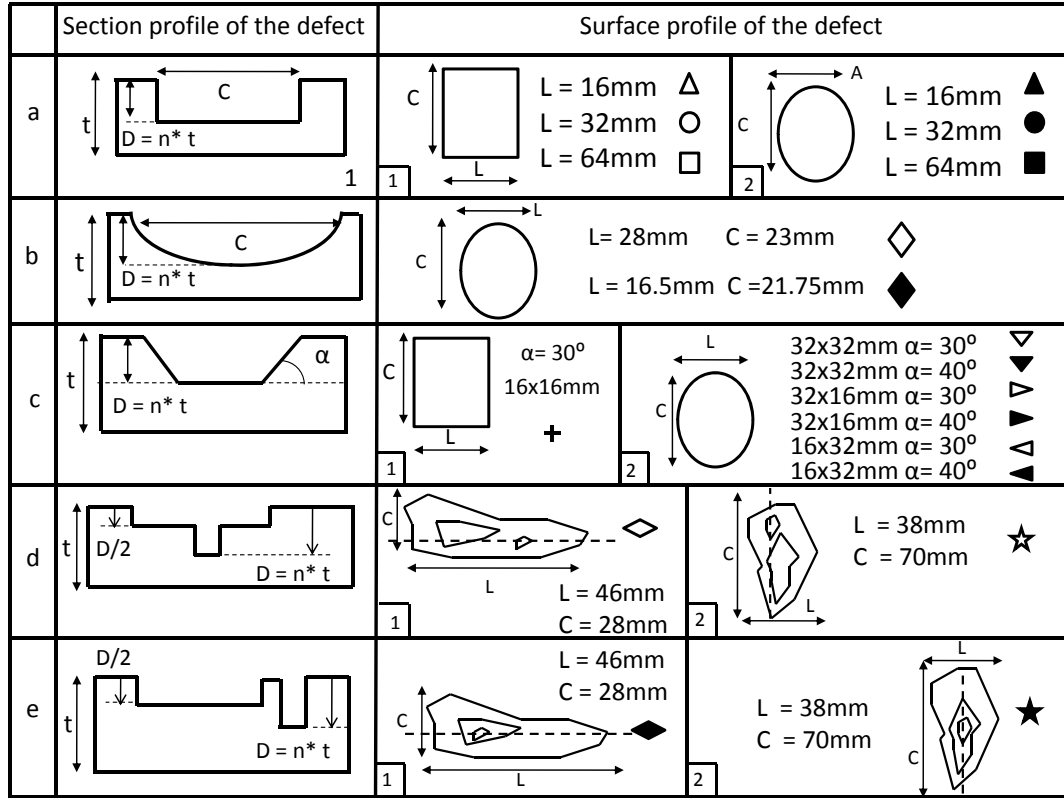
Figure 4.3: *Schematic of simulated 3D defects showing the depth profiles in the circumferential-radial plane and the surface profiles. Symbols are used in Fig. 4.4 and Fig. 4.5 to show the results for the different profiles.*

occurs does vary with axial extent). The results of the scattering from multilayered defects (d and e in Fig. 4.3) are highlighted in the inset of Fig. 4.4. It is evident that variation in the position of the maximum depth of the defect in the circumferential and axial directions has little effect on the magnitude of the maximum peak of the RC.

4.2.1 Numerical depth estimation

The goal of this work is to determine a method for sizing corroded areas remotely, especially those with low external circumferential extent (C_{eq} <25% of total circumference), as these smaller defects are the main practical interest; the main concern is the accurate estimation of the maximum defect depth. In the previous section
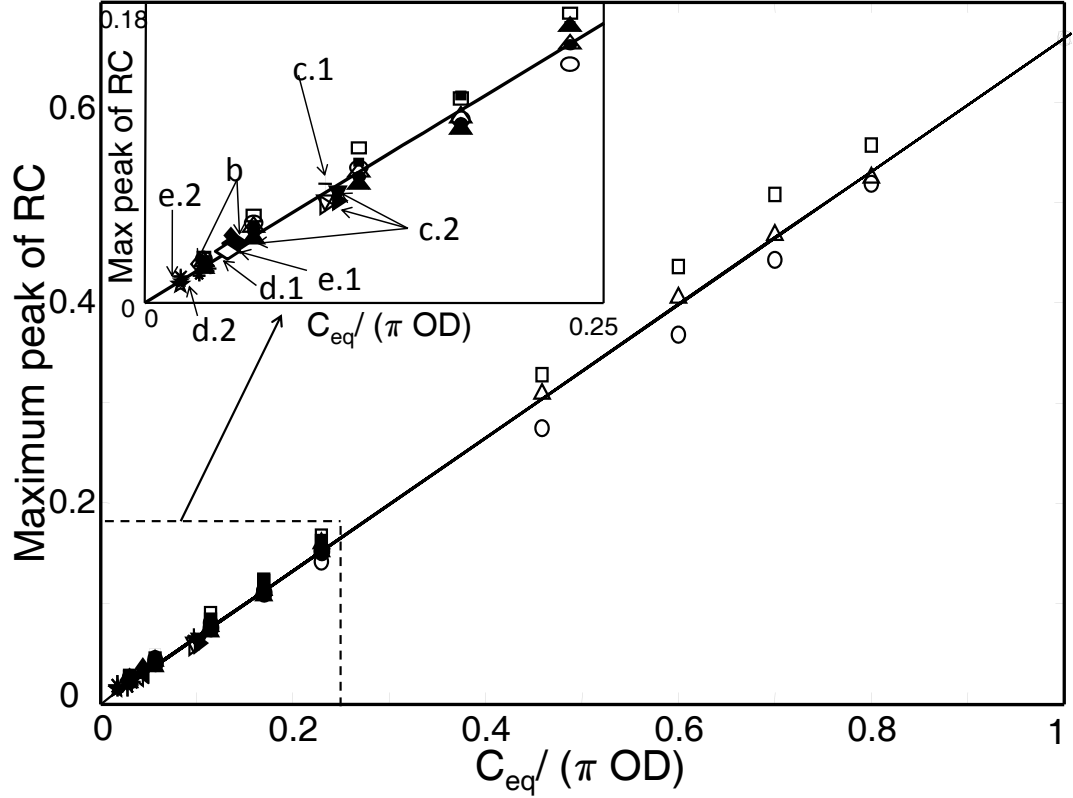
Figure 4.4: *Variation of the maximum peak of the RC from 3D defects with maximum depth (D) of 50% of the thickness, with the ratio of their equivalent circumferential extent (C_{eq}) to the outer circumference of the pipe (π OD). Symbols defined in Fig. 4.3.*

a study of the effect of axi-symmetric and simple 3D defects on the reflection co-efficient was presented. The results of this analysis can be used to estimate the maximum depth of a random defect in pipes. Figure 4.5 shows the variation of the maximum peak of the reflection coefficient with the ratio of the equivalent defect circumferential extent to the pipe circumference for defects with maximum depth of 25, 50 and 75% of the thickness. The markers shown in this figure are defined in Fig. 4.3. The circumferential extent is unity for axi-symmetric defects; for these defects the linear dependence between the first peak of the RC and the maximum depth of the defect shown in Fig. 4.2 can be used to draw a second y-axis on the plot (the scale is linear for depths < 75% of the thickness). The lines plotted in Fig. 4.5 represent the linear approximation at different depths between the maximum peak of the RC and the fractional circumferential extent for the 3D defects already shown in Fig. 4.4 . Figure 4.5 therefore shows that it is possible to estimate the maximum
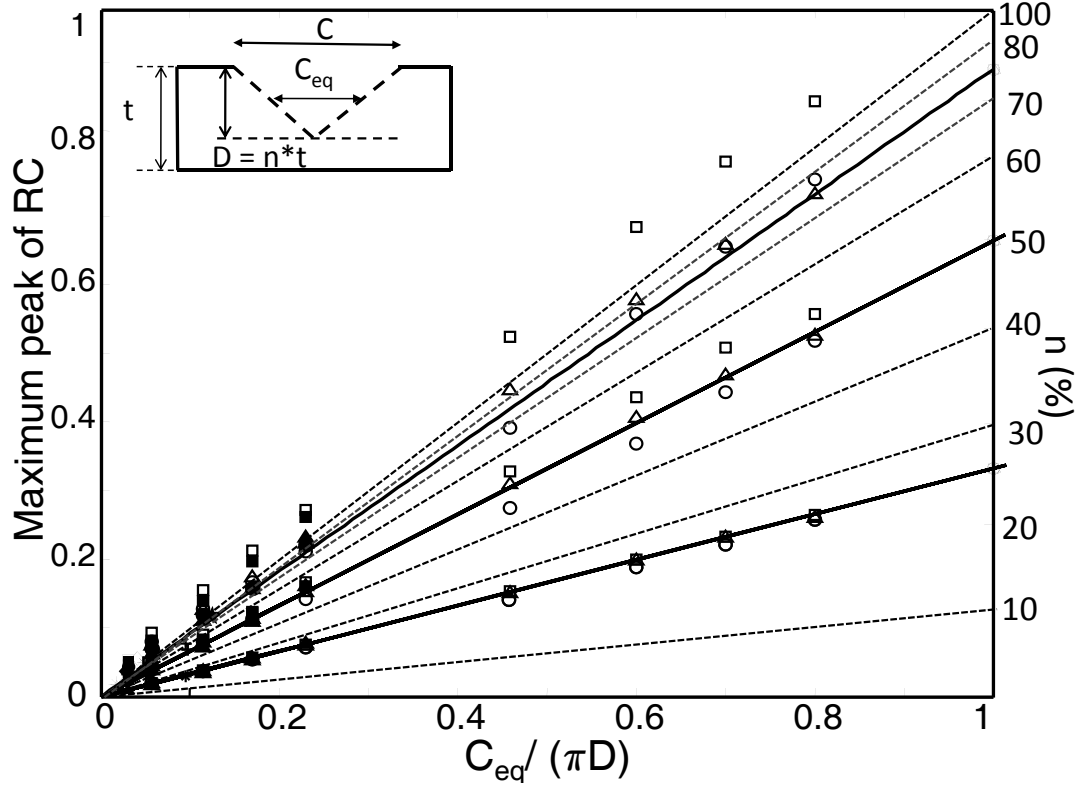
Figure 4.5: *Numerical depth estimation approach on simple 3D defects. Markers defined in Fig. 4.3.*

depth of a discontinuity by knowing the value of the first peak of the RC spectrum and its equivalent circumferential extent. It is then useful to plot the values of the estimated depths versus the values of the real depths of the simulated defects as a percentage of the thickness in order to validate this sizing method (see Fig. 4.6). The solid line in Fig. 4.6 represents the ideal case when the estimated depths match the real depth values. The region above that line is a safe zone, where the method is conservative. The dangerous area is below the solid line, where the maximum depth is underestimated by this approach. Figure 4.6 shows that this method estimates the maximum depth of the majority of the defects within an error range of about $\pm$ 20%. It is also interesting to note that the majority of the points in the safe region above the +20% line are small defects with $C_{eq} < 4\%$ of the outer circumference of the pipe.
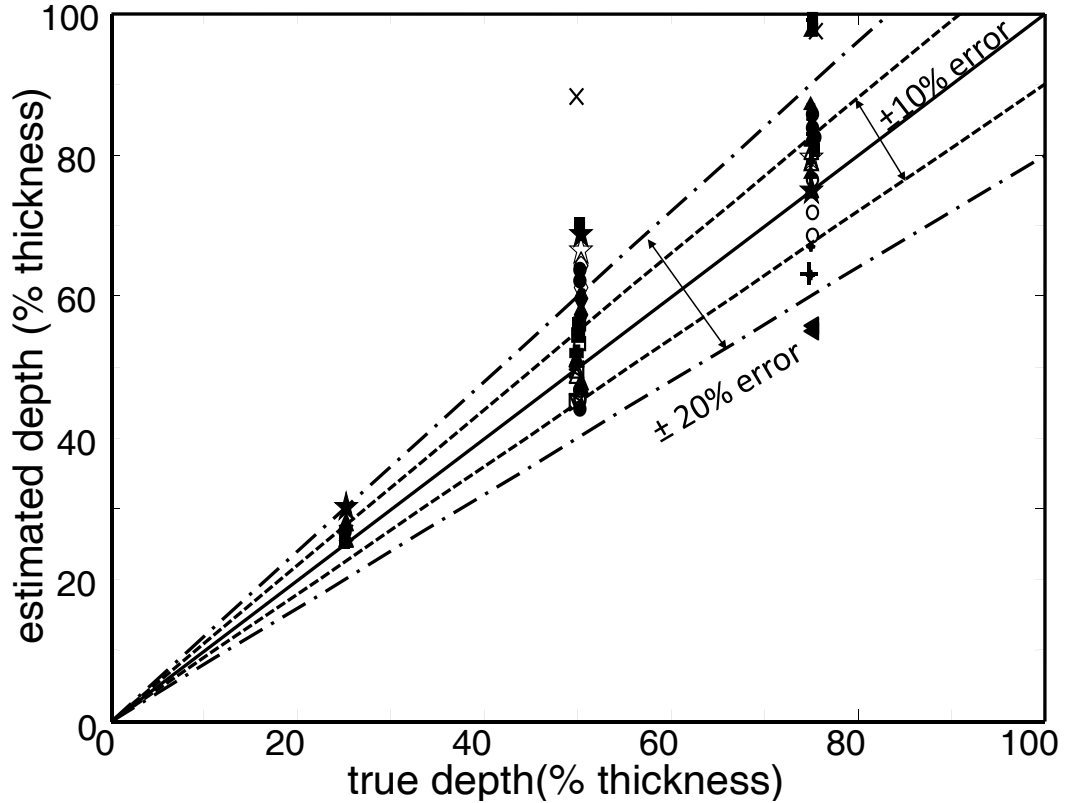
Figure 4.6: *Validation of the depth estimation method for simple shaped 3D defects.*

4.3 Real defect profiles

Detailed profiles of real corrosion patches were obtained from carbon steel pipes in operation. These discontinuities were found in topside oil rig steel pipelines; the pipes were standard 10 inch, schedule 160 (outer diameter 273 mm, wall thickness 28.6 mm). As mentioned in chapter 1, the mechanism behind the development of different forms of corrosion is not fully explained so defects are usually classified by appearance [9] and rate of growth [8, 119]. It has been observed that the morphology of corrosion attack in steel pipes ranges from uniform corrosion, which is a discontinuity with a gradual change of the depth through the thickness [9], to localized corrosion that occurs at discrete sites (such as pitting, crevice corrosion, mesa corrosion and stress corrosion cracking) [8, 60, 119–121]. Figure 4.7 shows six real depth profiles scanned with ultrasonically by Sonomatic Ltd. [122] and drawn as a flat plate. Defects X1 and X2 are examples of relatively uniform corrosion patches, whereas defects X4 and X5 are examples of complex defects with a gradual corrosion
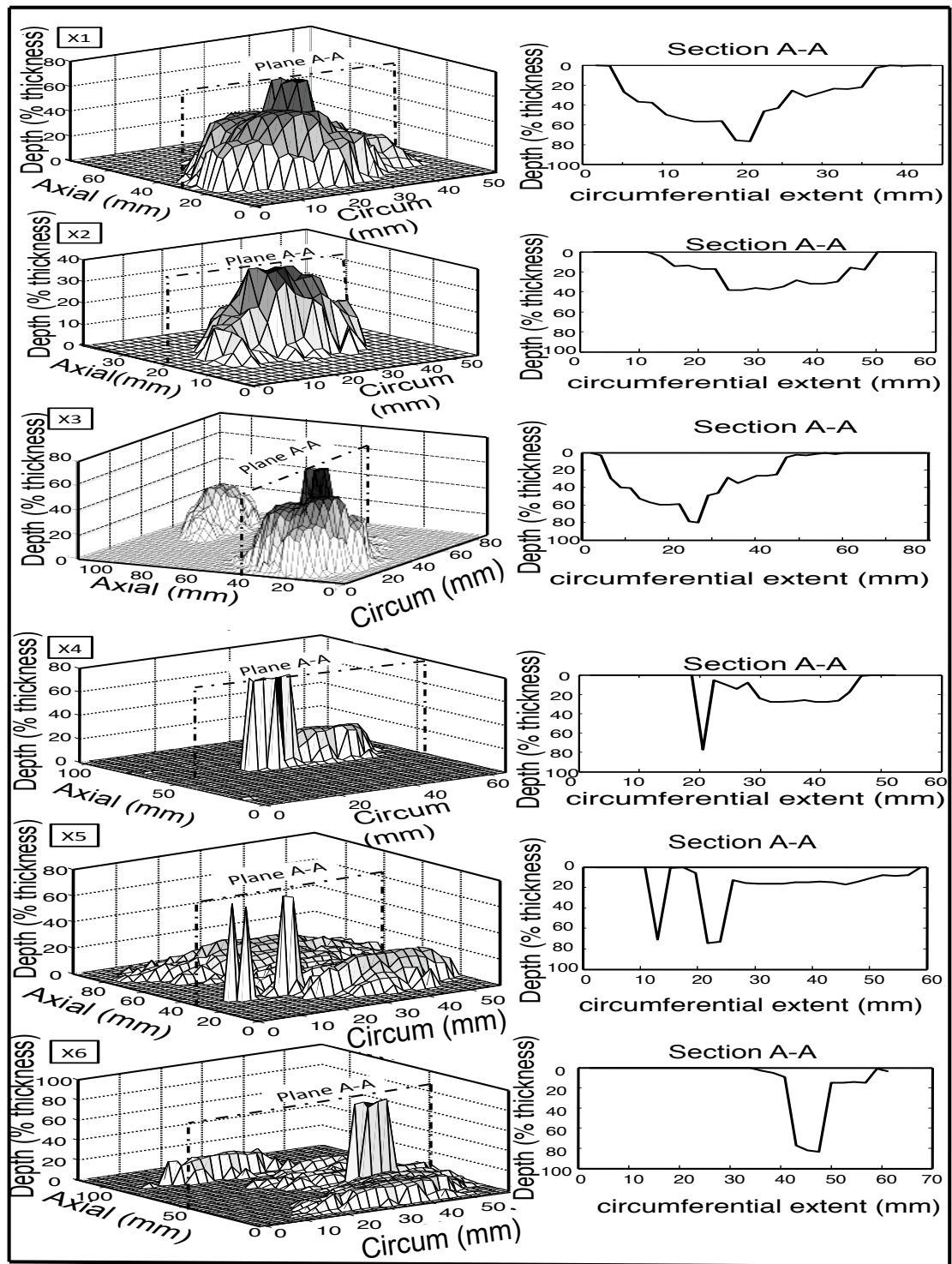
Figure 4.7: *3D representations of six real corrosion patches obtained from pipes in operation and drawn as a flat plate. The dimensions of the defects were scaled to a 4 inch pipe from the original 10 inch pipe.*
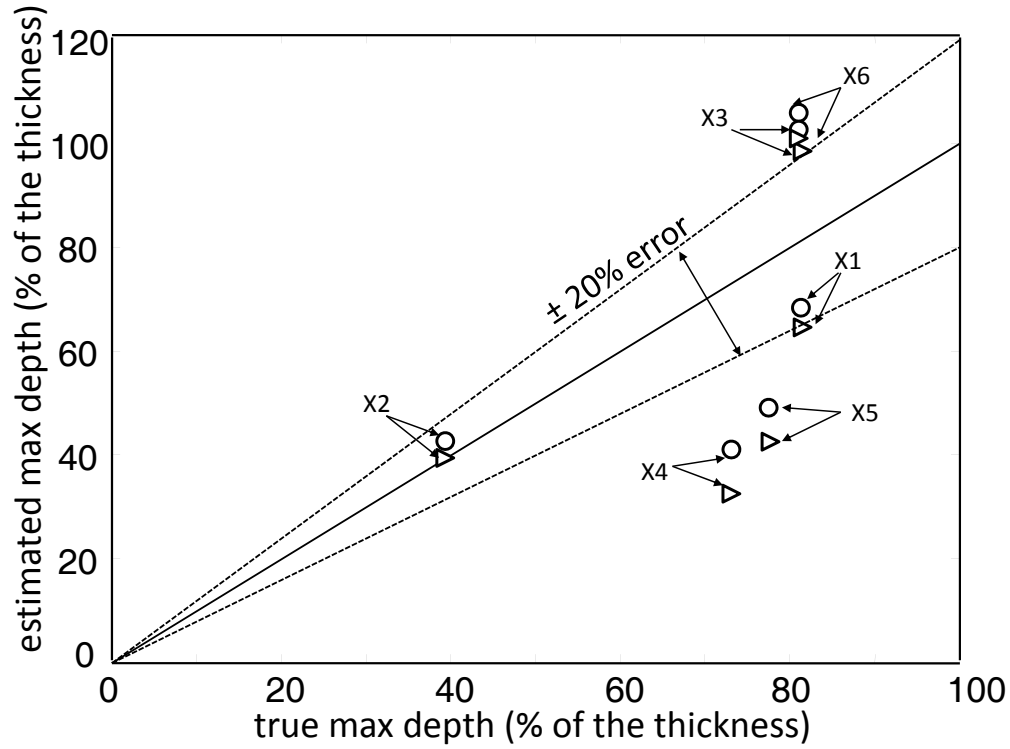
Figure 4.8: *Validation of the depth estimation method for real complex corrosion patches. Different markers represent the results from the same defect shape reproduced in 4 inch (triangles) and 10 inch (circles) pipes. Dimensions defined in Fig. 4.7.*

section profile but with a sudden change of the depth over a small circumferential region. Sharp pits like this often occur in regions of general corrosion, rather than as isolated features, especially in mild steel [123,124]. Defect X6 is also relatively sharp but with less general corrosion than in defects X4 and X5. Defects X1 and X2 were found close together on a pipe and would not be resolved at the frequencies typically used in guided wave pipe screening. Defect X3 is the two defects combined at their original relative positions; the reflection from defect X3 is therefore the superposition of the reflected signals from the two single entities [60]. Plane A-A in each of the defects of Fig. 4.7 is the plane parallel to the circumferential direction that intersects the defect at the axial location of its maximum depth; the section A-A therefore represents the most severe 2D profile of the defect in the circumferential direction.

The real defects were in 10 inch pipes but it was not feasible to reproduce them in this sized pipe for laboratory tests. Therefore the defect dimensions were scaled to a 4 inch schedule 40 pipe (outer diameter 114.3 mm, wall thickness 6.02 mm). This was done by keeping the maximum defect depth the same fraction of the wall thickness and scaling the plan dimensions by the pipe external diameter. Since the pipe wall thickness is not proportional to the pipe diameter, the defect geometries are not strictly similar so some change in reflection behaviour might be expected. It was therefore necessary to model both geometries. Full 3D models of 4 and 10 inch- schedule 40 steel pipes with these defects were created in the Solid Works CAD package and then imported into Abaqus for FE analysis. The excitation used was similar to that employed with the simpler defects discussed above, but the mesh was more refined due to the complexity of the geometries; Δx was 1.5 mm and the simulations converged with a time step Δt between 0.001-0.03 μsec. The reflection coefficient spectra were then numerically determined. Knowledge of the maximum circumferential extent of the corroded areas from the scanned data (if the technique is to be used in practice this will have to be determined from guided wave or other measurements, and this is the subject of current research done at University of Bristol and funded by the same overall project), together with the maximum peak of the RC in the frequency domain from the FE analysis, enables the estimation of the maximum depth of these features with the method explained in the last section. The equivalent circumferential extent is assumed to be half the maximum surface circumferential extent i.e. the profile is modelled as a V-notch. The results from the simulations of the six defect profiles of Fig. 4.7 created in 4 and 10 inch pipes are plotted in Fig. 4.8 in the same way as shown in Fig. 4.6 . It can be seen that the results from similar defect profiles in different sized pipes are very close together. It is evident that four of the six real corrosion patch results are within the $\pm$ 20% error range; two defects are in the dangerous area below the -20% line, where the depth is severely underestimated. The cause of this failure can be attributed to the particular section profile in the circumferential direction of these defects (see defects X4 and X5 of Fig 4.7). This means that approximating the circumferential profile at the maximum depth location as a V-notch is not valid in these cases; further work
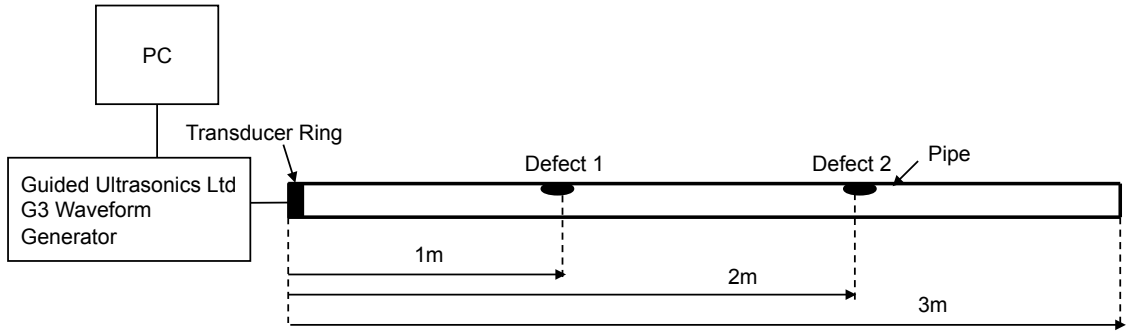
Figure 4.9: *Schematic representation of the experimental set up.*

is therefore required to adapt the method for this type of defect.

4.4 Experimental validation

In order to validate the FE predictions, laboratory experiments were performed on a set of 4inch steel pipes schedule 40 (outer diameter 114.3mm,wall thickness 6.02mm) to determine the effect of simple and complex shaped profiles on the T(0,1) mode. The experimental setup is shown in Fig. 4.9. Two pipes were tested horizontally in the laboratory supported by wooden supports which give negligible reflections of the ultrasonic signal. The pipes were 3m long and in each of them two defects were machined with a computer-aided manufacturing (CAM) tool, which is able to manufacture a computer-aided design (CAD) model of a defect with accuracy ±0.4mm respect to the expected model by using a 1mm ball nose cutter. The T(0,1) mode was excited at the left end of the pipe in Fig. 4.1; the first defect was manufactured at 1 meter from the excitation end in order to avoid the dead zone of the equipment; the second discontinuity was also machined one meter apart from the first in order to separate their reflected signals. A Guided Ultrasonics Ltd. [7] 4 inch ring, consisting of two rows of equally spaced piezoelectric transducers which applied alternating forces to the external wall of the pipe in the circumferential direction, was employed to input T(0, 1) mode in the structure. A Guided Ultrasonics Ltd. G3 Wavemaker instrument was used to generate successive 8 cycle Hanning windowed tonebusts at different centre frequencies, which together gave results over the frequency range
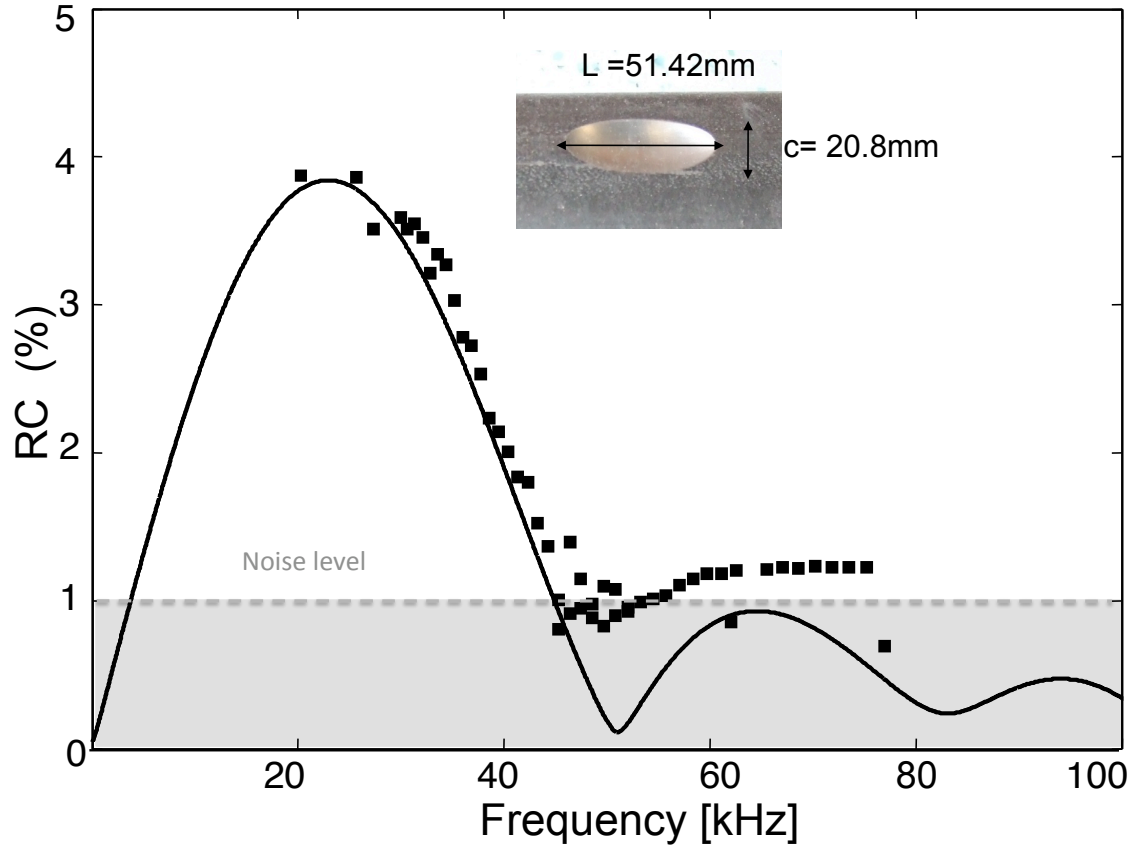
Figure 4.10: *Finite element predictions (solid line) and measurements (rectangular points) of a half ellipsoidal 75% maximum depth defect with a circumferential extent of 20.8 mm and axial extent of 51.42 mm.*

20-80 kHz. The ring acted also as a receiver, so the reflection coefficient spectra were calculated from the peak-to-peak ratio of the reflected and reference signals from these discontinuities in the time domain. The reflection from the right hand end of the pipe of Fig. 4.9 acted as the amplitude reference. This was not ideal as the reference was affected by the reduction in transmission due to the two defects. However, an FE model of the pipe layout of Fig. 4.9 was simulated in Abaqus; each of the two defects has a cross section area lost of a maximum of 3.8%. The results showed a modest change in transmitted amplitude, the maximum reduction compared to the input signal being less than 8% over the frequency range of interest, with the largest error towards the highest frequencies. The first defect was a simple ellipsoid, the maximum depth being 75% of the thickness; the comparison between the FE prediction (solid line) carried out in Abaqus and experiments (markers) are
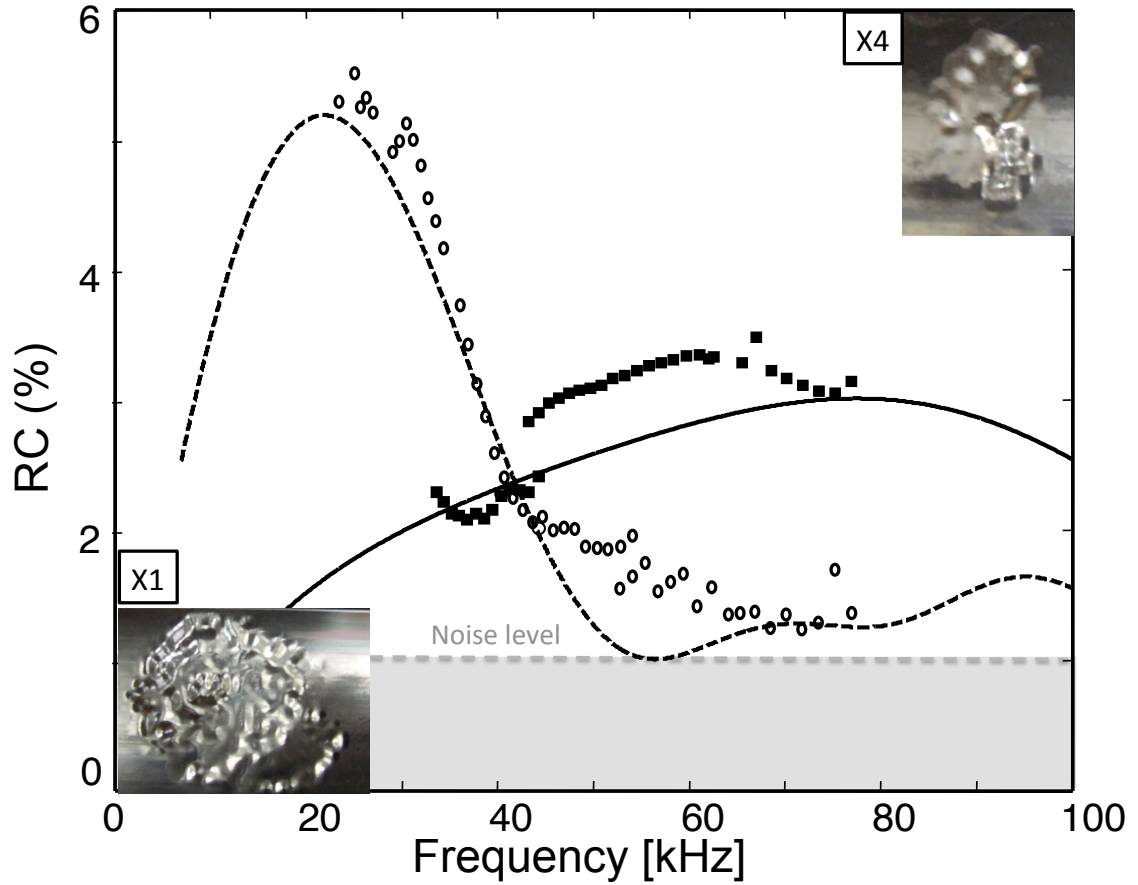
Figure 4.11: *Finite element predictions (solid and dotted line) and measurements (full rectangular and circular markers) of the defects X4 and X1 respectively. Details of defects given in Fig. 4.7.*

shown in Fig. 4.10. There is good agreement between the FE predictions and the measurements; the small difference between them at high frequency is due to the decrease of the SNR since the RC is approaching 1%, so the magnitude of the reflection coefficient from the defect is affected by the background noise. It is particularly interesting to note that the second peak of the reflection coefficient at high frequency is much lower than the first peak at low frequency, confirming the importance of testing at low frequencies to detect defects with gradually varying depth presented in chapter 3 of this thesis and in [125]. Figure 4.11 shows the comparison between the FE predictions of the intended model and the measurements for the two complex patches X1 and X4 of Fig. 4.7 machined with an accuracy of ±0.4mm respect to the intended model as mentioned above. Quite good agreement between the FE results

and the tests is shown, particularly considering the complexity of the defects and the small reflection coefficients being measured. The use of the machined defect profile for the numerical simulations would have decreased the small mismatch between the measured and the numerically simulated results.

4.5 Conclusions of the scattering analysis from complex defects

In this chapter a study of the reflection of the fundamental torsional mode T(0, 1) from 3D defects in pipes with different shapes has been carried out. An initial study of the reflection from axi-symmetric defects in pipes showed a linear dependence between the first peak of the RC and the maximum depth of the defect. The analysis of simple 3D shaped defects showed a linear dependence between the maximum peak of the RC in the frequency domain and the ratio of its equivalent circumferential extent to the total outer circumference of the pipe, at a fixed depth of the discontinuity. This means that the maximum peak of the RC is independent of the shape of the defect. In addition it has been found that the magnitude of the maximum peak of the RC will not be significantly affected by variation of either the axial extent of the discontinuity or the location of the maximum depth of the defect in the axial and circumferential directions (though the frequency at which the peak occurs will vary).

It has been shown that by knowing the maximum defect circumferential extent and by measuring the maximum of the RC it is possible to estimate the maximum depth of a random corrosion defect. The majority of the simulated defects were estimated to within a range of ± 20% depth error. This method has also been applied to real complex corrosion patches obtained from pipes in operation; some of these defects were reproduced in the laboratory with a CAM machine and validated with experiments. It has been shown that the main limitation of the method is on defects whose profile includes a sharp change in an otherwise gradually varying

shape. In order to complete this analysis it is then required to define a practical method to estimate accurately the circumferential extent of corrosion patches; this is simple when the circumferential extent is large but becomes progressively more difficult when the circumferential extent drops towards the wavelength used [98]. It is necessary to adapt the method to deal with the problematic patches. The first step is to diagnose the existence of sharp changes in profile and this is the subject of chapter 5.

Chapter 5

The diagnosis of problematic defects

5.1 Introduction

The depth estimation approach discussed in chapter 4 breaks down if a sharp change in depth is present within a small region around the circumference of the pipe surrounded by a general corrosion area. In order to adapt this method to these problematic cases, the first step is to diagnose the presence of such shaped defects. The idea here is to determine whether a defect is problematic from analysis of the reflection coefficient spectrum. In this chapter an investigation of whether the spatial frequency content of the defect correlates with the temporal frequency content of the reflection coefficient is presented (see Fig. 5.1). This approach is outlined in the sec. 5.2 and applied to different types of defect. The analysis starts with the decomposition of a 2D defect in the spatial frequency domain in sec. 5.2.1. The same decomposition approach is then applied to 3D discontinuities; in sec. 5.2.2 the correlation between the spatial frequency components of a half-ellipsoidal defect and the reflection coefficient spectrum is analyzed with FE simulations. Real corrosion patches are also decomposed in sec. 5.2.3. The results from these FE simulations are discussed in the sec. 5.3 and then numerical results of the ellipsoidal case are
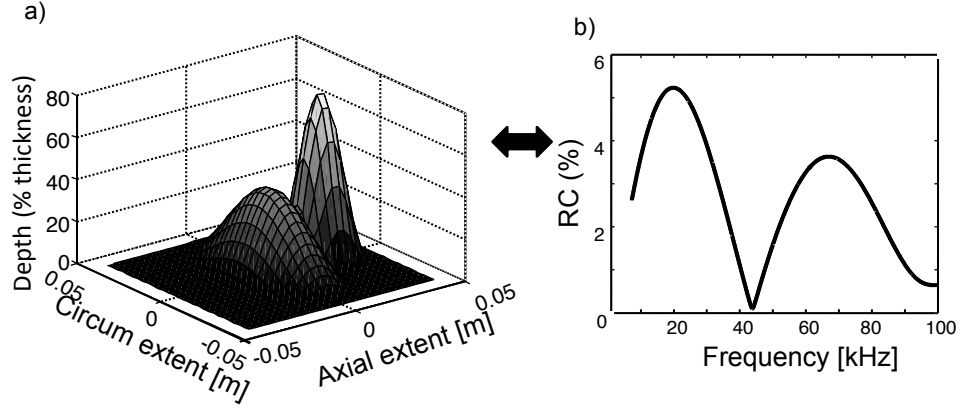
Figure 5.1: *Motivation of the chapter: a study to understand whether the spatial frequency content of a defect (a) correlates with the temporal frequency content of the reflection coefficient spectrum from this defect (b).*

validated with empirical measurements in sec. 5.4.

5.2 Decomposition approach

As mentioned above, the motivation of this chapter is to understand whether the spatial frequency content of a defect correlates with the temporal frequency content of the reflection coefficient spectrum. The approach used in this thesis to solve this problem is to use a Fast Fourier Transform (FFT) algorithm to transform a defect profile from the spatial domain to the corresponding spatial frequency domain. This algorithm is based on the idea that a periodic function can be broken into its harmonic components and it may be synthesized by adding together its harmonic components. The intention here is to employ this method to separate the low/high frequency components of a defect profile and to analyze their effect on the RC spectrum. The FFT algorithm has been well documented in the literature for example [126–128]. A common application of the FFT algorithm is to filter a time trace signal in order to remove its undesired high or low frequency components. In the next section the application of the decomposition approach to axi-symmetric and 3D defects is shown. The general procedure is the following: the FFT algorithm is applied to the full spatial profile defect. Two profiles, high pass and low pass were

respectively obtained by filtering the full profile in the frequency domain with the low/high pass cosine tapered filters at a value of the wave number (k_{lim}) and then applying an inverse FFT algorithm ($iFFT$) to transform both from the spatial frequency domain to the corresponding spatial coordinate system. In order to analyze the effect of the filtered profiles on the reflection coefficient spectrum curve, full 3D models of 4 inch schedule 40 steel pipes (OD = 114 mm, wall thickness = 6.02 mm) with these defects were created with the Rhinoceros 4.0 [129] and SolidWorks CAD package and then imported into Abaqus for the FE analysis. The details of the FE simulations have been shown in sec. 2.7.1 of this thesis. As mentioned for the real complex profile analyzed in sec. 4.3, linear elements with Δx of 1.5 mm were used for these simulations, which converged with a time step Δt between 0.001-0.05 μsec depending on the complexity of the geometry of the defect.

5.2.1 Axi-symmetric defect

Figure 5.2 shows the decomposition of a 2D defect in the frequency domain; this defect was created by adding up two cosine shaped defects with axial extents of $\frac{2\pi OD}{8}$ and $\frac{2\pi OD}{32}$ and with maximum depths of 20 and 40% of the wall thickness respectively (see Fig. 5.2a). Figure 5.2b shows the absolute value of the amplitude of FFT of this profile where the x-axis represents the wave number ($k_{axial} = \frac{2\pi}{\lambda}$) in the axial direction. As mentioned above, the profiles in Figs. 5.2c and 5.2d were respectively obtained by filtering the full profile in the frequency domain with a low/high pass half cosine tapered filter at a value of the wave number k_{lim} of 200 m^{-1}, the filter acting within a range of $\pm$ 20 m^{-1}. A correlation between the value of the k_{lim} and the shape of the defect can be found if more defect profiles are filtered and analyzed. The reflection coefficient spectra from the three axi-symmetric defect profiles of Figs. 5.2a, 5.2c and 5.2d were then numerically determined and plotted in Fig. 5.3. The predicted reflections from the low pass defect and the high pass defect were also superposed in the time domain, resulting in the RC spectrum plotted with a dotted line in Fig. 5.3. In this figure it is interesting to note that the RC spectrum from the low pass defect has a predominant behavoiur at frequencies lower
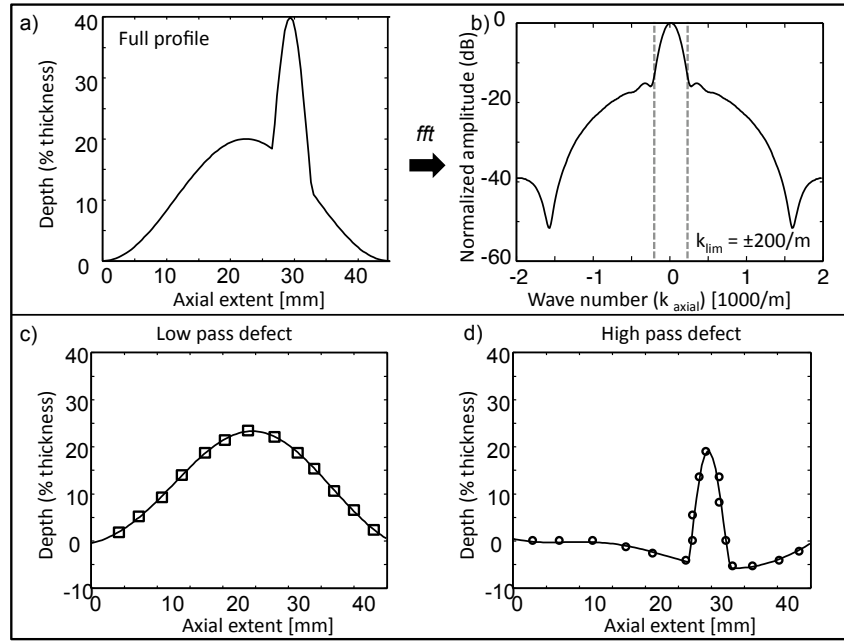
Figure 5.2: *Decomposition of the axi-symmetric defect in the spatial frequency domain. (a) full profile; (b) spatial FFT of (a); (c) low pass filtered defect; (d) high pass filtered defect. Profiles in (c) and (d) are respectively obtained by filtering the FFT of (b) with a low/high pass cosine tapered filter in the spatial frequency domain at a value of the wave number k_{lim} of 200 m^{-1}, shown by a dotted line in (b).*
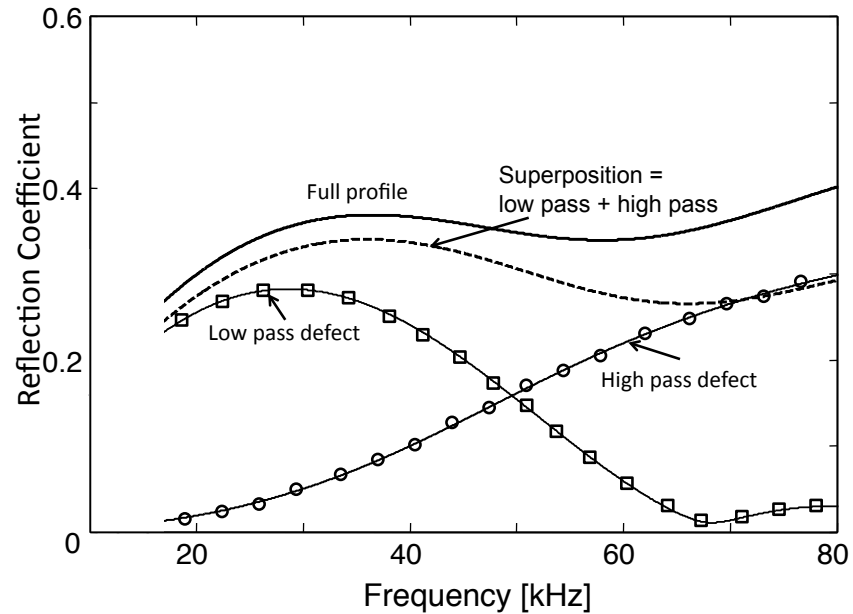
Figure 5.3: *Reflection coefficient spectra from the 2D defect of Fig. 5.2a (solid line), low pass defect of Fig. 5.2c (squares), high pass defect of Fig. 5.2d (circles) and superposition of the low pass and high pass defects (dotted line).*

than about 50 kHz; whereas the RC spectrum from the high pass defect shows a important effect at frequencies higher than 50 kHz. In addition, it is interesting to see that the superposition line shows a behaviour similar to the RC spectrum from the full defect profile. However, the overall RC obtained superposing the RC spectra from the two profiles underestimates the RC spectrum from the full 3D profile defect, the mismatch increasing with the frequency.

5.2.2   Ellipsoid

A three-dimensional (3D) defect shown in Fig 5.1a and plotted in matrix format in Fig 5.4a was then analyzed. This defect represents a simplified example of a discontinuity with a sharp change in depth within a small region around the circumference of the pipe surrounded by a smoother area. It has been created by adding up two half-ellipsoidal shaped defects with axial extents of $\frac{2\pi OD}{16}$ and $\frac{2\pi OD}{20}$ and circumferential extent of $\frac{2\pi OD}{8}$ and $\frac{2\pi OD}{20}$ and with maximum depths of 80% and 40% of the wall thickness respectively (see Fig. 5.4a). In this case the 2D-FFT algorithm is required since both the axial and circumferential profiles of the defect need to be decomposed into the spatial frequency domain. Figure 5.4 shows the 2D-FFT decomposition applied to this ellipsoidal defect; in Fig. 5.4b the absolute value of the 2D-FFT of this profile is shown, where the axes are the wavenumbers in the axial (k_{axial}) and circumferential (k_{circum}) directions. The profiles in Figs. 5.4c and 5.4d were obtained by filtering the full profile with a half cosine filter at a value of the wave number k_{lim} of 200 m^{-1} (as drawn with a dotted line in Fig. 5.4b) and the cosine filtered acted within a range of $\pm 20 m^{-1}$. This value of k_{lim} was chosen *ad hoc* in order to separate the two main components of the defect in the spatial domain. As mentioned above, this is just a first analysis on the relationship between the spatial coordinates of the defect and its effect on the reflection coefficient spectrum; the relationship existing between the spatial coordinates of the defect and the value of k_{lim} needs to be studied by considering more and different defect profiles. Note that the scales of the depth map of the three profiles of Figs. 5.4a, 5.4c and 5.4d are different. The reflection coefficient spectra from the three 3D defects shown in

Figure 5.4: *Decomposition of the ellipsoidal defect in the spatial frequency domain. (a) full profile; (b) spatial 2D FFT of (a); (c) low pass filtered defect; (d) high pass filtered defect. Profiles in (c) and (d) are respectively obtained by filtering the 2d FFT of (b) with a low/high pass cosine tapered filter in the spatial frequency domain at a value of the wave number k_{lim} of 200 m^{-1}. Note that the scales of the depth map of the three profiles (a), (c) and (d) are different.*
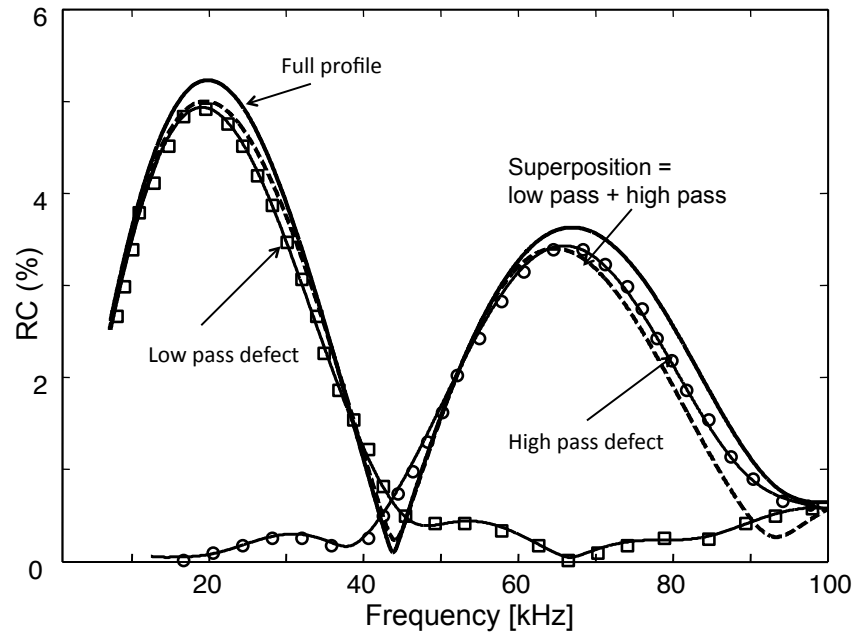
Figure 5.5: *Reflection coefficient spectra from the ellipsoidal defect of Fig. 5.4a (solid line), high pass defect of Fig. 5.4d (circles), low pass defect of Fig. 5.4c (squares) and superposition of the low pass and high pass defects (dotted line).*

Figs. 5.4a, 5.4c and 5.4d were then numerically determined and plotted in Fig. 5.5. The predicted reflections from the low pass defect and the high pass defect were also superposed in the time domain, resulting in the RC spectrum plotted with a dotted line in Fig. 5.5. It is clear again from the Fig. 5.5 that the low pass defect gives predominant values of the RC spectrum at low values of the frequency (lower than about 40 kHz) and the RC spectrum from the high pass defect gives an important effect at higher values of the frequency. In addition, it is interesting to note that in this case the superposition line matches well with the RC spectrum from the full 3D profile defect; small errors are introduced at high frequencies where the superposition curve underestimates the RC curve from the full profile.

5.2.3   Real corrosion patches

In order to complete this qualitative analysis, the decomposition approach is applied to the six corrosion patches obtained from pipes in operation shown in Fig. 4.7 and analyzed in sec. 4.3. Figure 5.6 shows the decomposition analysis applied to a smooth defect, X1. Figure 5.6a is the depth corrosion map of the defect as percentage of the thickness. A two-dimensional Fast Fourier Transform (2D-FFT) algorithm was applied to the full defect matrix resulting in the matrix shown in Fig. 5.6b. Two profiles shown in Figs. 5.6c and 5.6d were again obtained by filtering the full profile at a value of the k_{lim} of 200 m^{-1} (note that the scales of the depth map of the three profiles in Figs. 5.6a, 5.6c, and 5.6d are different). Figure 5.7 shows the FE predictions of the RC spectrum curves from the three defect profiles of Figs. 5.6a, 5.6c, and 5.6d.

It is evident that that the low pass defect obtained by filtering the full profile in the spatial frequency domain gives a significant reflection at frequencies lower than 60 kHz. In contrast, the high pass defect obtained by the same filtering procedure but with a high pass filter, shows high reflection at frequencies higher than 60 kHz. The maximum peak of the RC spectrum from the full defect profile is at about 20 kHz, the axial extent of the whole corrosion patch being about 45 mm. This confirms that the location of the maximum peak of the RC is controlled by the axial extent of

Figure 5.6: *Decomposition of the defect X1 in the spatial frequency domain. (a) full profile; (b) spatial 2D FFT of (a); (c) low pass filtered defect; (d) high pass filtered defect. Profiles in (c) and (d) are respectively obtained by filtering the 2d FFT of (b) with a low/high pass cosine tapered filter in the spatial frequency domain at 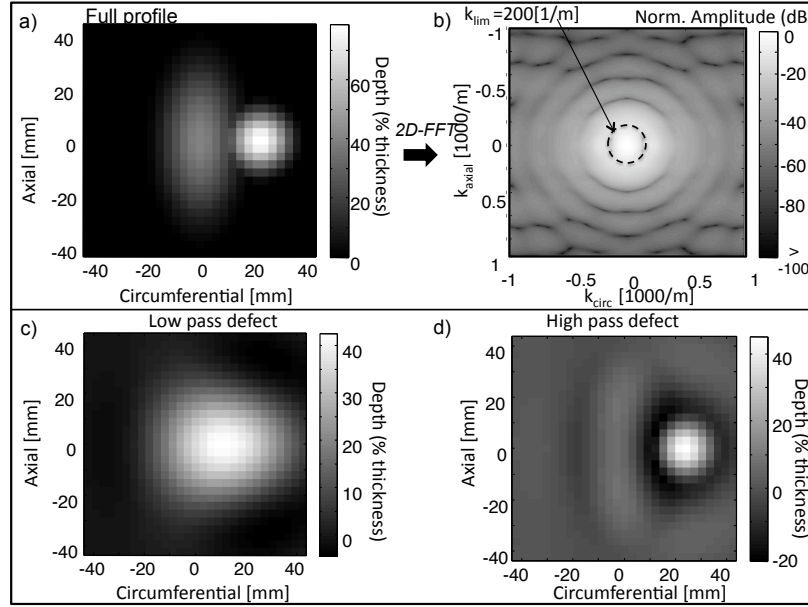a value of the wave number k_{lim} of 200 m^{-1}. Note that the scales of the depth map of the three profiles (a), (c) and (d) are different.*

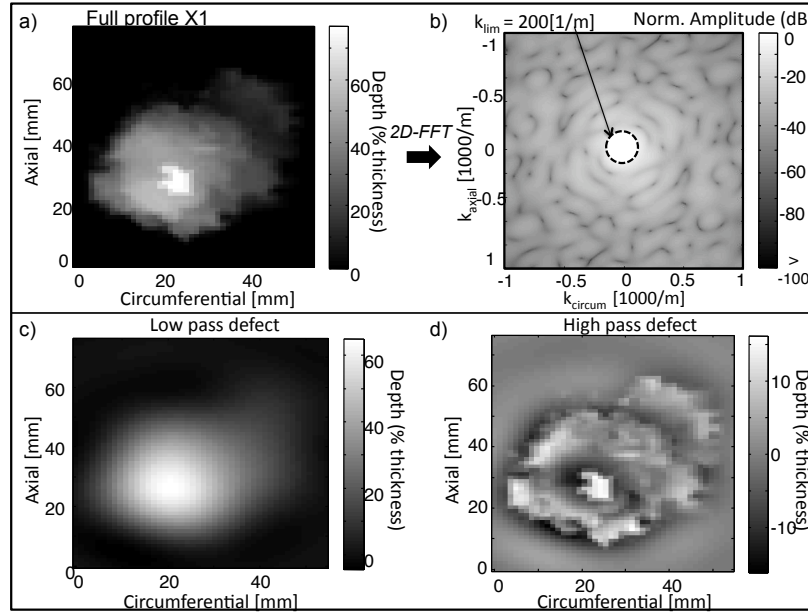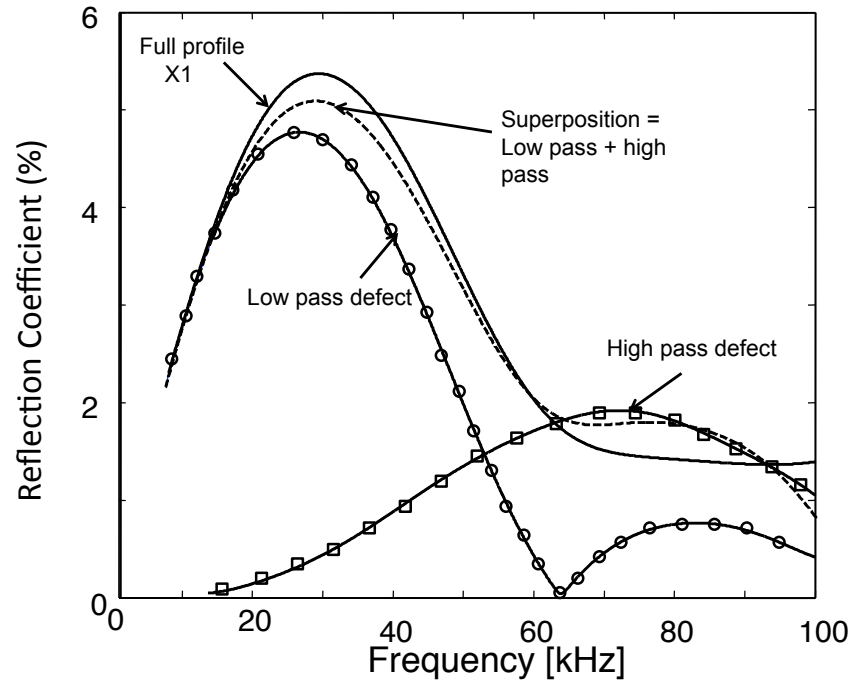**Figure 5.7:** *Reflection coefficient spectra from the defect X1 of Fig. 5.6a (solid line), high pass defect of Fig. 5.6d (circles), low pass defect of Fig. 5.6c (squares) and superposition of the low pass and high pass defects (dotted line).*

the defect so that the peak of the RC happens at values of $\frac{L}{\lambda} = 0.25$, where L is the external axial extent of the defect [30]. At higher frequencies, the RC drops since the reflection is affected by the gradual change in depth of the defect through the thickness of the pipe as shown in chapter 3. It is evident that the superposition of the two filtered defects in the time domain plotted with dotted line in Fig. 5.7 match well with the RC behaviour from the full defect profile; this means that the main contribution to the RC spectrum of the whole profile is given by the low frequency part of the defect. The high frequency component of the defect gives only a very modest contribution to the maximum of the RC spectrum from the full defect profile; its contribution being about 35% of the maximum peak value of the RC from the full defect.

The same decomposition procedure was applied to all the other defects. The decomposition of another smooth profile defect X2 is shown in Fig. 5.8. Two profiles shown in Figs. 5.8c and 5.8d were obtained by the same filtering procedure as described above for defect X1 (note that the scales of the depth map of the three profiles in Figs. 5.8a, 5.8c, and 5.8d are different). Figure 5.9 shows the predicted reflection coefficient spectra from the defects shown in Figs. 5.8a, 5.8c, and 5.8d, the dotted line again being the result of the superposition in the time domain of the reflections from the two filtered defects. Also in this case the maximum peak of the RC spectrum from the full defect profile happens at about $\frac{L}{\lambda} = 0.25$ [30], where L is about 15 mm. It is particularly interesting to note that the defect obtained by filtering the full profile with a low pass cosine tapered filter in the spatial frequency domain corresponds to a RC spectrum curve with significant values only at low frequencies (lower than 60 kHz). In contrast, the high pass defect gives high reflection only at frequencies higher than 60 kHz. The superposition curve again matches well with the reflection from the full profile defect. In addition, it can be noted that the high pass defect contributes 28% to the peak of the RC from the full profile; at high frequency (above 80 kHz) the overall RC is dominated by the high pass defect, its peak here is about 50% of the maximum peak.

The decomposition of the defect profile X3, which is the combination of the defects

Figure 5.8: *Decomposition of the defect X2 in the spatial frequency domain. (a) full profile; (b) spatial 2D FFT of (a); (c) low pass filtered defect; (d) high pass filtered defect. Profiles in (c) and (d) are respectively obtained by filtering the 2d FFT of (b) with a low/high pass cosine tapered filter in the spatial frequency domain at a value of the wave number k_{lim} of 200 m^{-1}. Note that the scales of the depth map of the three profiles (a), (c) and (d) are different.*
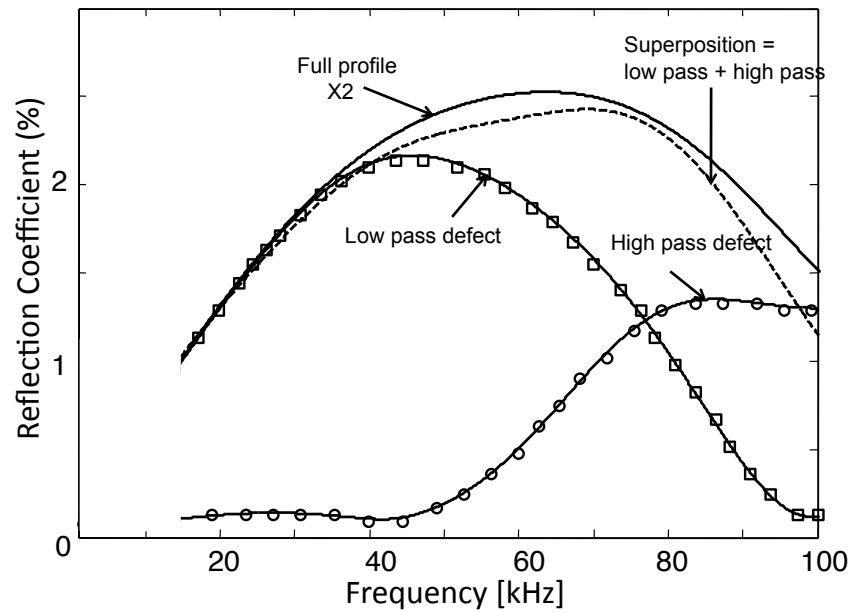
Figure 5.9: *Reflection coefficient spectra from the defect X2 of Fig. 5.8a (solid line), high pass defect of Fig. 5.8d (circles), low pass defect of Fig. 5.8c (squares) and superposition of the low pass and high pass defects (dotted line).*

Figure 5.10: *Decomposition of the defect X3 in the spatial frequency domain. (a) full profile; (b) spatial 2D FFT of (a); (c) low pass filtered defect; (d) high pass filtered defect. Profiles in (c) and (d) are respectively obtained by filtering the 2d FFT of (b) with a low/high pass cosine tapered filter in the spatial frequency domain at a value of the wave number k_{lim} of 200 m^{-1}. Note that the scales of the depth map of the three profiles (a), (c) and (d) are different.*
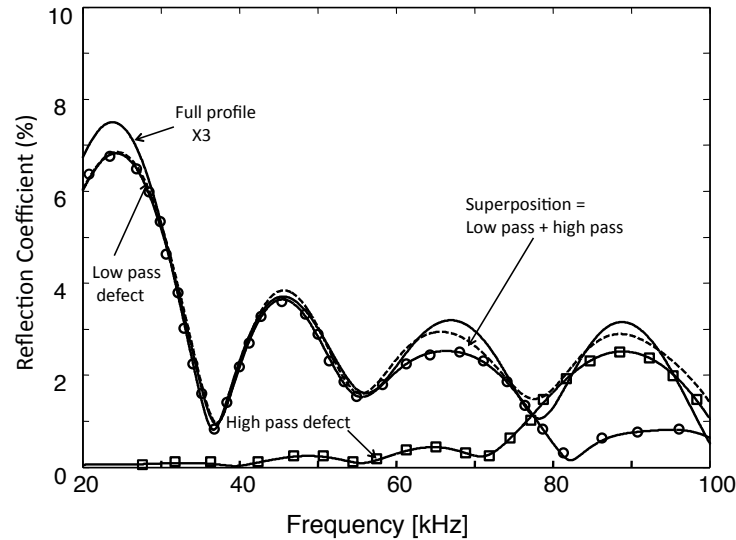
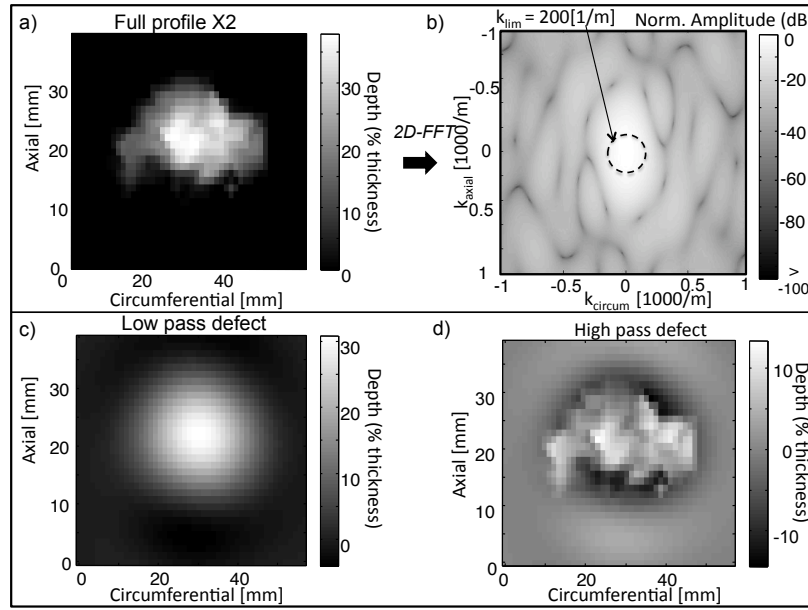**Figure 5.11:** *Reflection coefficient spectra from the defect X3 of Fig. 5.10a (solid line), high pass defect of Fig. 5.10d (circles), low pass defect of Fig. 5.10c (squares) and superposition of the low pass and high pass defects (dotted line).*

X1 and X2 at their original relative positions is shown in Fig. 5.10. Figure 5.11 shows the predicted RC spectra from the full profile defect of Figs. 5.10a and from the defects of Fig. 5.10c, and 5.10d which were obtained by the same filtering procedure as described above for defect X1 (note that the scales of the depth map of the three profiles in Figs. 5.10a, 5.10c, and 5.10d are different). In this case the RC spectrum from the whole corrosion patch is given by the composition of X1 and X2; the maximum peak of the RC happens at $\frac{L}{\lambda} = 0.5$ where L is the centre-centre distance between the two defects [60]. In addition, since the two defects are located at different circumferential positions and their axial extent is similar, their maximum reflection coefficients sum, as already shown in [60]. The periodic variation of the RC from the full defect with frequency is due to the interference of waves traveling between the two scatterers as shown for an axi-symmetric tapered defect in sec. 3.3. Again, the superposition line (dotted line in the figure) matches well with the RC from the full defect and in addition the RC spectrum from the low pass defect (see circles in Fig. 5.11) has significant values only at frequencies lower than about 60 kHz. In contrast, the RC from the high pass defect (see rectangles in Fig. 5.11) gives very low scattering at low frequencies and a more significant reflection (about 2%) only at frequencies higher than 60 kHz. This also means that the RC from the low pass defect profile gives the most significant contribution to the maximum of the RC from the full defect profile, since the maximum of the RC happens at about 20 kHz and also because the RC from the high pass defect has significant values only at higher frequencies.

Figure 5.12 shows the decomposition analysis applied to one problematic defect, X4. Figure 5.12a shows the geometry of the defect in a matrix format; two profiles shown in Figs. 5.12c and 5.12d were then obtained by the same filtering procedure as described above for defect X1 and the predicted RC spectrum curves from these defects are plotted in Fig. 5.13 (note that the scales of the depth map of the three profiles in Figs. 5.12a, 5.12c, and 5.12d are different). The predicted reflections from the low pass defect and high pass defect were also superposed in the time domain, resulting in the RC spectrum plotted with a dotted line in Fig. 5.13. It is evident again that there is a good match between the superposition curve and the

Figure 5.12: *Decomposition of the defect X4 in the spatial frequency domain. (a) full profile; (b) spatial 2D FFT of (a); (c) low pass filtered defect; (d) high pass filtered defect. Profiles in (c) and (d) are respectively obtained by filtering the 2d FFT of (b) with a low/high pass cosine tapered filter in the spatial frequency domain at a value of the wave number k_{lim} of 200 m^{-1}. Note that the scales of the depth map of the three profiles (a), (c) and (d) are different.*
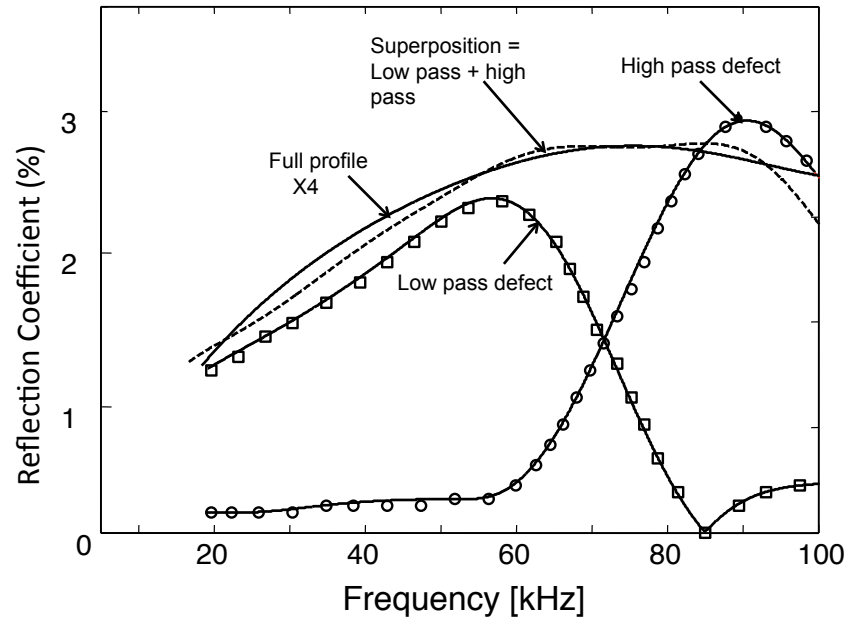
Figure 5.13: *Reflection coefficient spectra from the defect X4 of Fig. 5.12a (solid line), high pass defect of Fig. 5.12d (circles), low pass defect of Fig. 5.12c (squares) and superposition of the low pass and high pass defects (dotted line).*

RC from the full profile. The maximum peak of the RC from the full profile happens at about 70 kHz, again being controlled by the axial extent of the corrosion patch (about 12 mm). It is clear that the low pass defect gives a significant reflection at values of the frequency lower that 70 kHz and very low RC at higher frequencies. In contrast, the high pass defect gives high reflection only at frequencies higher than 70 kHz. It can also be noted from Fig. 5.13 that in contrast with the earlier cases, a significant contribution to the maximum of the reflection coefficient from the full defect is given by the high pass defect.

The other problematic defect X5 has also been decomposed as shown in Fig. 5.14. This corrosion patch shown in Fig. 5.14a presents two pits inside a general corroded area. It is also composed of two separate parts (which are more visible from the low pass defect of Figs. 5.14c); these discontinuities have a centre-centre distance of about 45 mm resulting in a RC peak at about 40 kHz as shown in Fig. 5.15 [60]. In addition from Fig. 5.15 it is not possible to see the influence of the two small pits with a maximum depth of 60% of the thickness of the pipe on the RC spectrum from the full profile. The reason is that these pits are circumferentially separated but located at the same axial position and they also have the same axial extent of about 6 mm, therefore they will affect the RC spectrum significantly only at frequencies of about 135 kHz, out of the frequency range used here. The two profiles shown in Figs. 5.14c and 5.14d were obtained by the same filtering procedure as described above for defect X1 (note that the scales of the depth map of the three profiles in Figs. 5.14a, 5.14c, and 5.14d are different). Figure 5.15 shows the predicted RC spectra from the full profile defect and from low pass and high pass defects of Figs. 5.14c, and 5.14d. Again, the superposition of the RC from the two filtered defects fits well with the RC from the full defect profile; a small error is present at higher frequencies due probably to the decreasing validity of the superposition approach. High values of the RC from the low pass defect again occur at low frequencies; the first peak in this frequency range happens at 40 kHz since it is given by the interference of the low frequency components of the corrosion patch, as mentioned above. The high pass defect gives minimal reflection below about 80 kHz. As explained before, a more significant value of the RC from this defect of Fig. 5.14d is expected to happen at
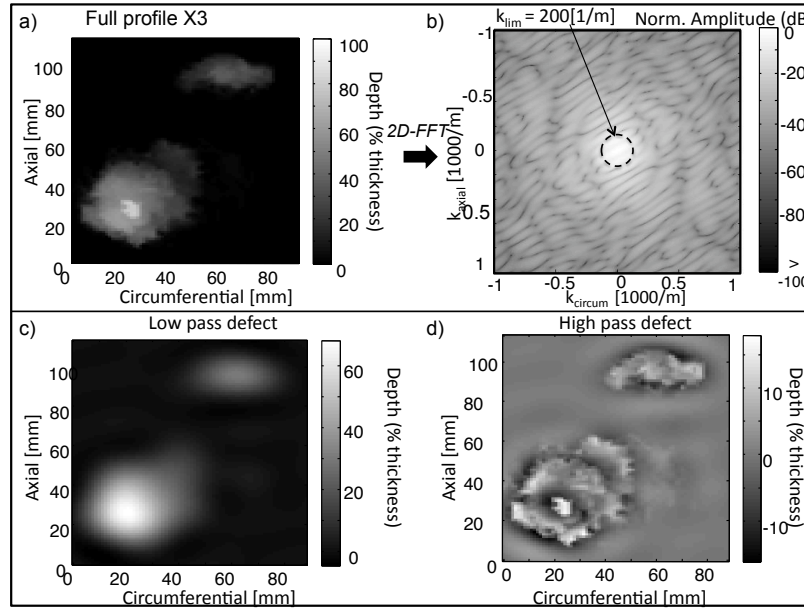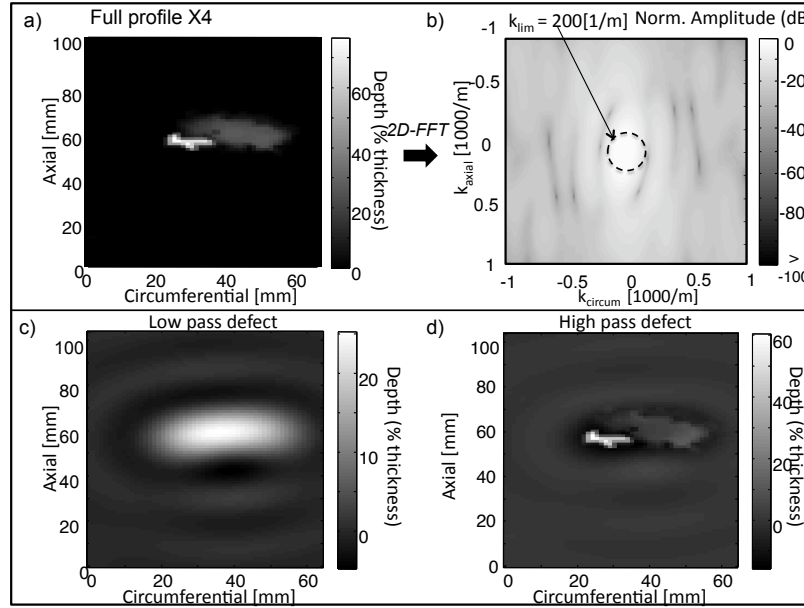
Figure 5.14: *Decomposition of the defect X5 in the spatial frequency domain. (a) full profile; (b) spatial 2D FFT of (a); (c) low pass filtered defect; (d) high pass filtered defect. Profiles in (c) and (d) are respectively obtained by filtering the 2d FFT of (b) with a low/high pass cosine tapered filter in the spatial frequency domain at a value of the wave number k_{lim} of 200 m^{-1}. Note that the scales of the depth map of the three profiles (a), (c) and (d) are different.*
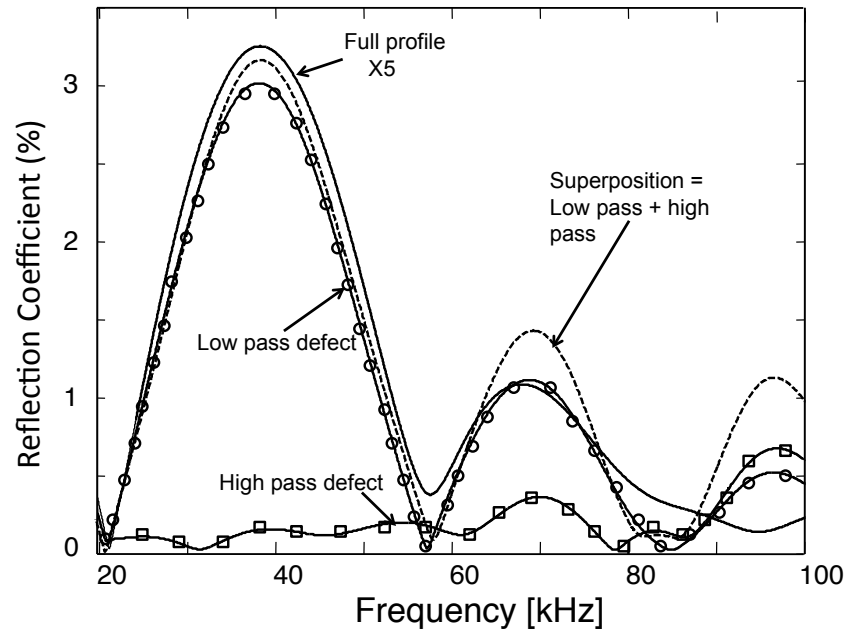
Figure 5.15: *Reflection coefficient spectra from the defect X5 of Fig. 5.14a (solid line), high pass defect of Fig. 5.14d (circles), low pass defect of Fig. 5.14c (squares) and superposition of the low pass and high pass defects (dotted line).*

frequencies higher than 100 kHz driven by the two small pits.

The decomposition analysis applied to the last analyzed defect X6 is shown in Fig. 5.16. Again two profiles shown in Figs. 5.16c and 5.16d were obtained by the same filtering procedure as described above for defect X1 (note that the scales of the depth map of the three profiles in Figs. 5.16a, 5.16c, and 5.16d are different). The predicted RC spectra from the three defects shown in Figs. 5.16a, 5.16c, and 5.16d were plotted in Fig. 5.17. The RC from the low pass defect is again shown with circles and it presents high values only at frequencies lower than 70 kHz. In contrast, the RC spectrum from the high pass defect shows significant values only at frequencies higher than 70 kHz. The superposition line again agrees well with the RC spectrum from the full profile which is plotted with a solid line. This RC spectrum shows a periodic behaviour with frequency, its maximum peaks increasing their value with frequency. This beahaviour is due to the geometry of the defect and to the interference between its components. In particular, the RC spectrum from the defect filtered with a high pass filter (see the square markers in Fig 5.16) shows clearly that the RC values from the full defect profile at frequencies higher than 80 kHz are due to the sharp change in depth within a small area with a circumferential extent of about 10 mm and axial extent of about 8 mm (resulting in a peak of the RC at about 100 kHz). In contrast, the peaks of the RC at lower frequencies are due to the interference between the low pass components of the defects shown in Fig. 5.16c.

5.3   Establishment of criterion for sharp defects

The effect of high and low pass defect profiles on the RC spectra has been analyzed in the previous sections in a frequency range from 20 to 100 kHz. In every defect analyzed (axi-symmetric or 3D), it has been noted that the low pass defect obtained by filtering the full profile in the spatial frequency domain with a low pass filter gives a significant reflection only at low frequencies. In contrast, the high pass defect obtained by the same filtering procedure but with a high pass filter, gives significant
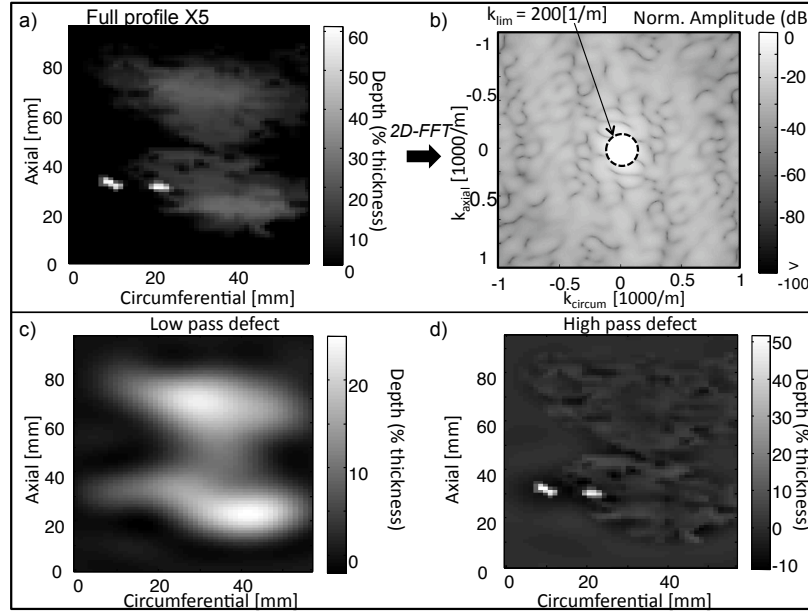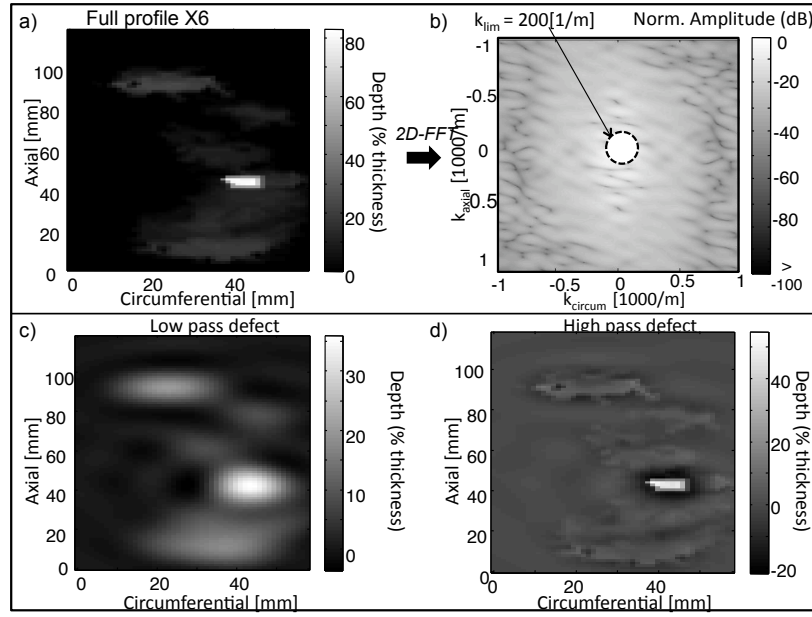
Figure 5.16: *Decomposition of the defect X6 in the spatial frequency domain. (a) full profile; (b) spatial 2D FFT of (a); (c) low pass filtered defect; (d) high pass filtered defect. Profiles in (c) and (d) are respectively obtained by filtering the 2d FFT of (b) with a low/high pass cosine tapered filter in the spatial frequency domain at a value of the wave number k_{lim} of 200 m^{-1}. Note that the scales of the depth map of the three profiles (a), (c) and (d) are different.*
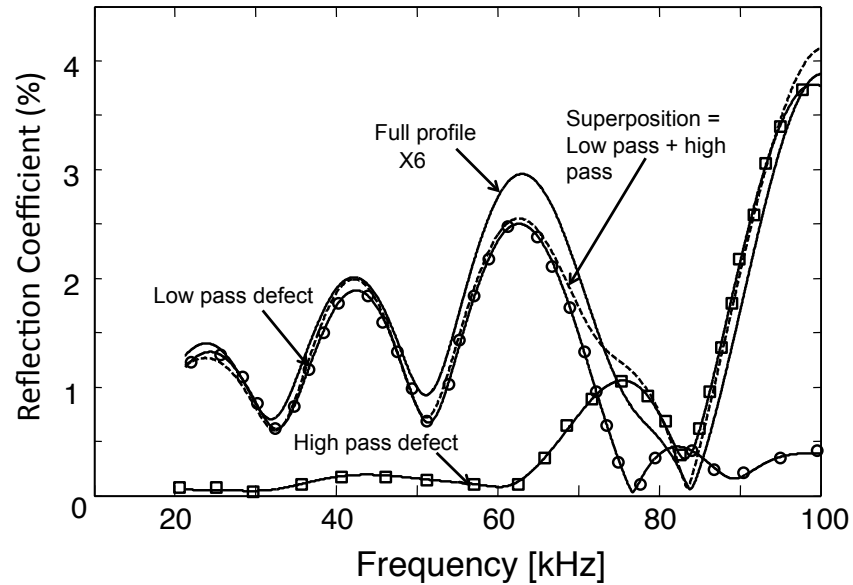
Figure 5.17: *Reflection coefficient spectra from the defect X6 of Fig. 5.16a (solid line), high pass defect of Fig. 5.16d (circles), low pass defect of Fig. 5.16c (squares) and superposition of the low pass and high pass defects (dotted line).*
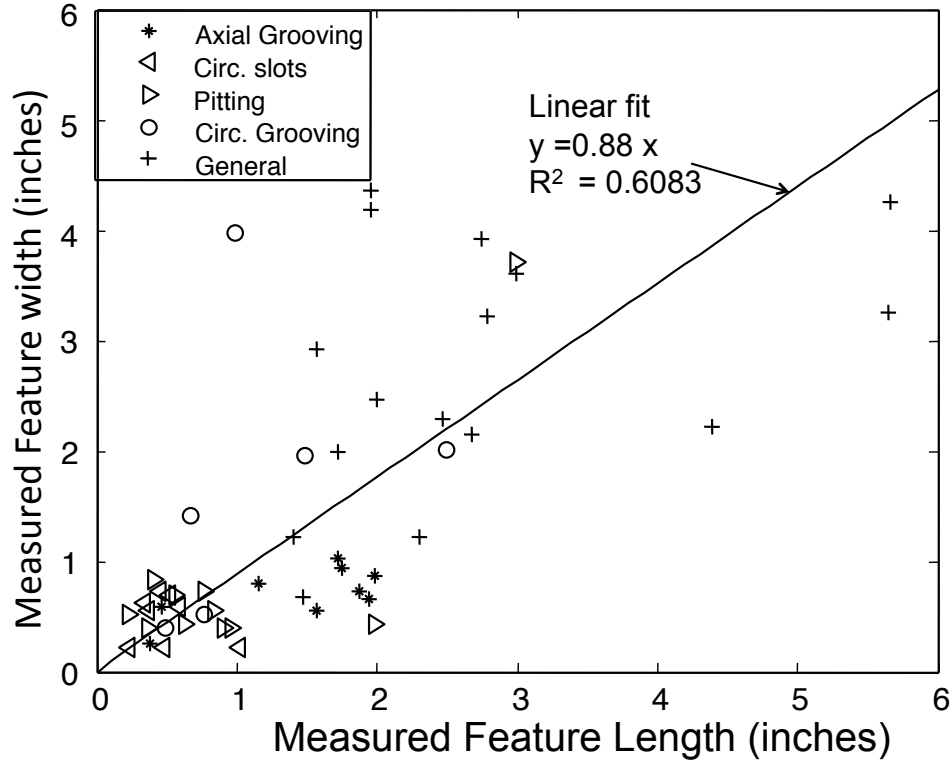
Figure 5.18: *Feature classification from intelligent pig data from [3].*

reflection only at high frequencies. In the case of a defect with a sharp change in depth within a small region around the circumference of the pipe surrounded by a general corrosion area (such as the discontinuities shown in Fig. 5.4a, Fig. 5.12a and Fig. 5.16a), it can be noted that the high pass defect contributes significantly to the maximum peak of the RC, its contribution being bigger than 50% of the peak of the RC. This is not evident for the problematic defect X5 in Fig. 5.15 since, as mentioned above, the sharp change in depth (see Fig. 5.14a) has an axial extent of about 6 mm, so the peak of the RC is expected at a frequency out of the range used. In contrast, in the case of a more gradual corrosion patch such as defect X1 or X2, the high pass defect makes only a very modest contribution to the maximum peak of the reflection coefficient.

As mentioned in the chapter 1 of this thesis, the morphology of the corrosion is difficult to classify since the there are so many parameters that can influence its growth. Valor *et al* in [130], for example, used a stochastic model to describe pitting corrosion growth, since it is considered as a random process which can be affected by

corrosion rate, maximum pit depth, time to perforation and so on. Assumptions on the shape of a corrosion defect are therefore difficult to make. However, an empirical study collected information of features from pipelines in operation; Fig. 5.18 taken from [3], shows the relationship between the measured axial extent versus the circumferential extent of some features found in pipes. It can be noted that the trend of these empirical points can be approximated by a linear fit ($y = 0.88x$) especially for small defects; this means that a linear relationship between the axial and circumferential extent of a discontinuity can be considered with coefficient of determination $R^2 = 0.6$. This observation helps to determine a possible approach to identify the presence of a problematic defect. Firstly, the measurement of the circumferential extent of the corrosion is required. Then, under the assumption that the defect is extended axially as much as circumferentially (since the slope of the linear fit is almost unity), the frequency at which the maximum peak of the reflection coefficient occurs can be calculated [30]. If the RC spectrum has its maximum peak at about the calculated frequency then the interest is to look at the values of the RC at higher frequencies. If the RC at frequencies higher than the one at which the peak occurs is higher than 50% of the peak value, then a sharp change in depth is likely to be present in a generally corroded area. In these circumstances the depth determination method proposed in the chapter 4 is unreliable. More defects need to be analyzed in order to validate the threshold of 50% proposed above. This procedure is limited by the size of the defect, as shown for the defect X5, since if pits smaller than 8 mm are present, higher RC components occur at frequencies out of the range analyzed. In addition, this approach to size a discontinuity is based on the assumption that the axial extent is similar to the circumferential extent which is not always valid (see Fig. 5.18). There are also cases such as the defect X6, where the depth estimation method works even if there a small deep defect inside a generally corroded area. This is because the circumferential extent used for the calculation, which is the one at the axial location of the maximum depth of the corrosion patch, takes into account only the shape of the small pit and is not affected by the general corroded area (see Fig. 4.7). The V-notch approximation therefore fits well the shape of the defect and therefore the method does not break down.

5.3.1   Validity of the superposition approach

As expected from the properties of the algorithm, the use of the FFT to filter a defect has introduced negative depth values to the filtered profiles as for example to the high pass defect profile shown in Fig. 5.4b. This increase of the thickness has been easily modeled in FE. For all the defects , it has been seen that the original profile of the defect can be reconstructed with a maximum error of 0.01% by adding up the two filtered defect matrices. In addition, the superposition in the time domain of the reflections from the high and low pass defects showed a behavior similar to the reflection from the full defect profile. The idea to superpose the individual high/ low pass frequency components of a defect assumes that the wavenumber components can be evaluated independently. In general, when a wave field (u_{inc}) illuminates a defect, this acts as a source which excites a scattered field (u_{scat}) that interacts with the incident wave. The total field then can be then expressed as [131]

$$u^{tot} \quad = \quad u^{inc} + u^{scat}. \tag{5.1}$$

The idea to superpose the individual wavenumber components is based on the Born approximation. This approximation states that the total field (u^{tot}) on the scatterer surface can be estimated by the incident field (u^{inc}) by neglecting the perturbations given by the scatterer (u^{scat}), if the scatterer is weak ($u^{scat} << u^{inc}$) [55, 104, 106, 131–133]. As has been shown in chapter 4 of this thesis, an axi-symmetric defect is usually a stronger scatterer than a 3D defect if both have the same maximum depth, since the maximum peak of the RC increases with the circumferential extent of the discontinuity [30]. Figure 5.19 shows in the first plots the comparison between the RC spectrum from the 2D defect (see Fig. 5.2a) and the corrosion patch X4 (see Fig. 5.12a). It is clear from the figure that the 3D defect is a weaker scatterer, the RC from the 2D defect being more than an order of magnitude bigger than the 3D one (note the different scales in the second plots of Fig.5.19). As mentioned in sec. 2.7, the Born approximation can be used at very low values of the product ka ($ka << 1$), where a is the characteristic dimension of the scattered. However, Gubernatis *et al* [104] in 1977 showed that this condition is only valid for
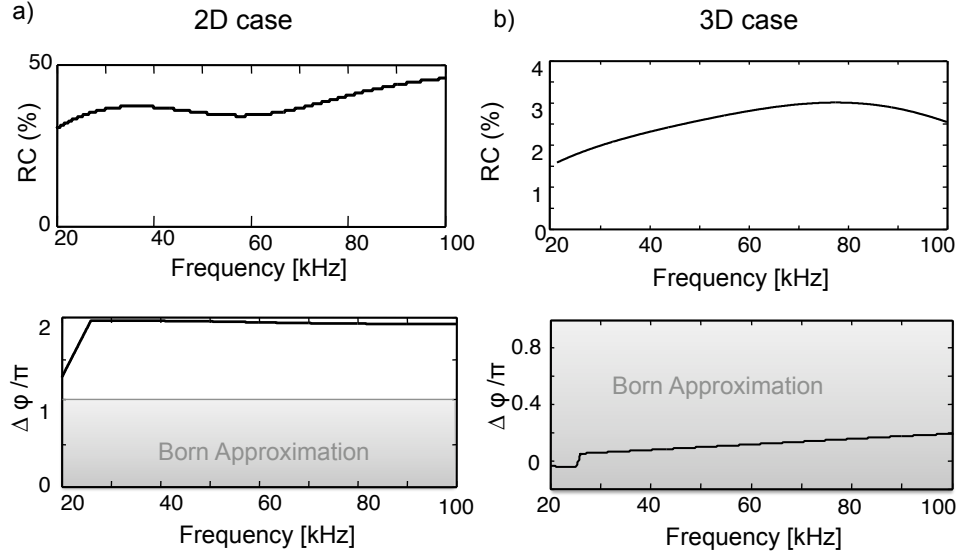
Figure 5.19: *Comparison between the predicted RC spectrum curve and the phase shift between the signal transmitted from the defect and the signal monitored at the same location along the length of the pipe but without any defect in frequency domain of (a) the 2D defect of Fig. 5.2 and (b) 3D corrosion patch X4 of Fig. 5.12a. Note that the scales of both plots from the 2D and 3D defect are different.*

spherical voids and inclusions; a different shape factor is needed for a more complex feature. Slaney *et al* [134] in 1984 analyzed the validity of this approximation for homogeneous cylinders, including in the analysis the deviation from the average refractive index to describe the influence of the scatterer on the surrounding medium. More recently Simonetti [135] questioned the definition of the weak scatterer for which this approximation works. In general, the necessary condition for the Born approximation to be valid is that the change in phase between the incident wave and the wave propagating through the object has to be less than π [131, 134, 135]. In pipes modeled with a defect, the necessary condition to be respected is

$$\Delta\phi \;=\; \phi_{inc} - \phi_{trans} \leq \pi, \tag{5.2}$$

where ϕ_{trans} is the phase of the signal transmitted from the defect and monitored at a fixed distance from the excitation, and ϕ_{inc} is the phase of the signal monitored at the same distance from the excitation but in a pipe without the defect. In the second plots of Fig. 5.19 the phase shift ($\Delta\phi = \phi_{inc} - \phi_{trans}$) for 2D and 3D defects is

plotted in a frequency range from 20 to 100 kHz. It is evident that the condition 5.2 is not respected for the 2D defect in the frequency range of interest. This can be the cause of the mismatch of the superposition line with respect to the RC from the full profile in Fig. 5.3, where the error increases with the frequency. In the 3D cases analyzed such as the half-ellipsoidal defect in Fig. 5.5 and corrosion patches such as in Fig. 5.13, superposition works well since the Born approximation is valid. In addition, Kak and Slaney in [131], showed that for cylinders the Born approximation works well for values of $\Delta\phi$ up to 0.8 π; the small error shown at high frequency in the 3D cases such as Fig. 5.15 can be caused by the superposition approach being less accurate as the frequency increases.

5.4 Experimental validation

In order to validate the FE results shown in the previous sections, laboratory experiments were performed on a set of 4 inch schedule 40 steel pipes (OD = 114.3 mm, wall thickness 6.02mm) to investigate the effect of a sharp change in depth over a small region around the circumference of the pipe surrounded by a general corrosion area. In particular, the half ellipsoidal defect shown in sec. 5.2.2 has been considered for this validation. The experimental setup is shown in Fig. 5.20. Three pipes were tested horizontally in the laboratory supported by wooden supports which give negligible reflections of the ultrasonic signal. The pipes were 3m long and in each of them one defect was machined with a computer-aided manufacturing (CAM) tool, which is able to manufacture a computer-aided design (CAD) model of a defect with accuracy of 0.4mm using a 1 mm ball nose cutter. The T(0,1) mode was excited at 1 meter from the left end of the pipe in Fig. 5.20; the defect was manufactured at 1.2 meters from the excitation in order to avoid the dead zone of the equipment. A Guided Ultrasonics Ltd. [7] 4 inch ring was employed to input T(0, 1) mode in the structure. This ring consists of two rows of equally spaced piezoelectric transducers which applied alternating forces to the external wall of the pipe in the circumferential direction. A Guided Ultrasonics Ltd. G3 Wavemaker instrument was used to generate successive 8 cycle Hanning windowed tonebusts at different centre fre-

quencies, which together gave results over the frequency range 20-80 kHz. The ring also acted as a receiver, so the reflection coefficient spectra were calculated from the peak-to-peak ratio of the reflected and reference signals from these discontinuities in the time domain. The reflection from the left hand end of the pipe of Fig. 5.20 acted as the amplitude reference.
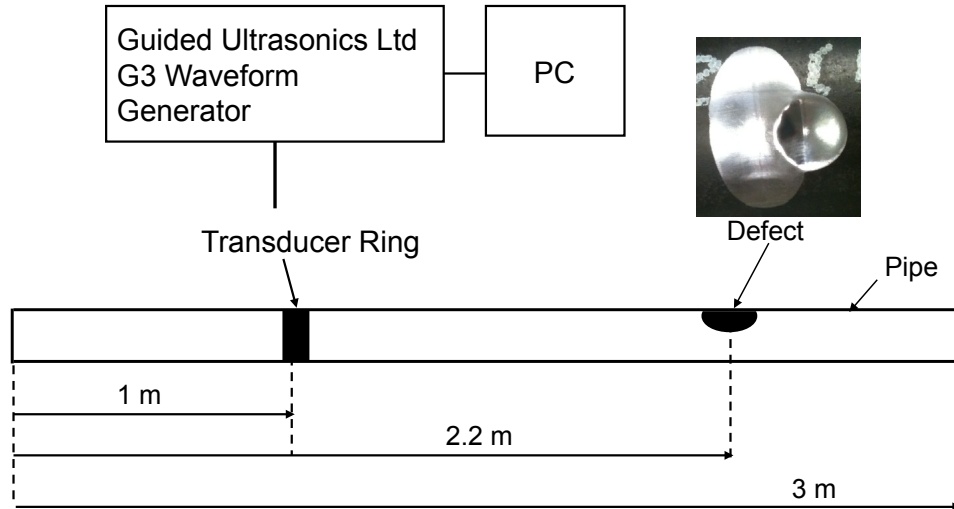
Figure 5.20: *Schematic of the test set up.*

As mentioned above, the half ellipsoidal defect was considered for the validation of the FE simulations. The use of the 2D-FFT algorithm introduced negative depths to the filtered defect as shown in Fig. 5.4d, which were easily represented in the FE model. However, this increase of the thickness can not be reproduced in a real pipe so these profiles were machined with their negative depth values set to zero. Figure 5.21 shows the predicted RC spectra from these ellipsoidal shaped defects with no negative values. The dotted line is again the superposition in the time domain of the numerically predicted reflected signals from the high and low pass defect. As expected, the superposition curve does not match the full profile RC curve since the negative depths present in the filtered profiles were removed; nevertheless these profiles were machined and tested to validate the FE model. Figure 5.22 shows the comparison between the FE predictions of the reflection coefficient spectra from the defects shown in Fig. 5.21 and the experimental results plotted with markers. It is evident that the test results match well with the numerical predictions; values of the RC spectrum lower than 1% cannot be validated experimentally due to the
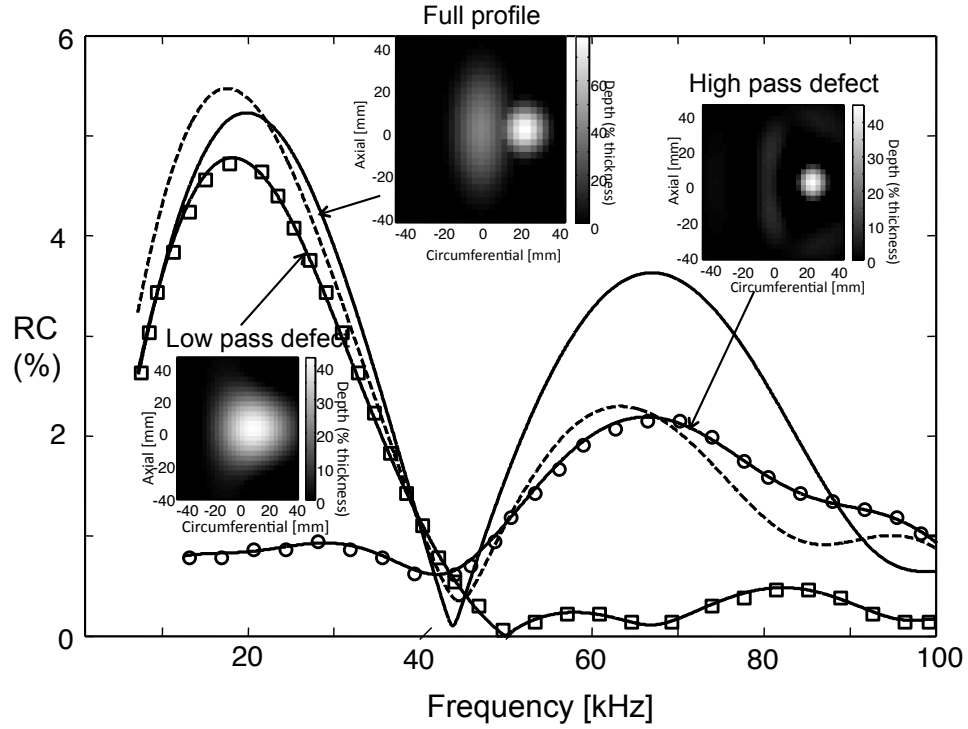
Figure 5.21: *FE predictions of reflection coefficient spectra from the half-ellipsoidal defect of (solid line), high pass defect (circles), low pass defect (squares) with their negative depths set to zero. Superposition of the low pass and high pass defects is shown with a dotted line. Details of defects given in the figure.*
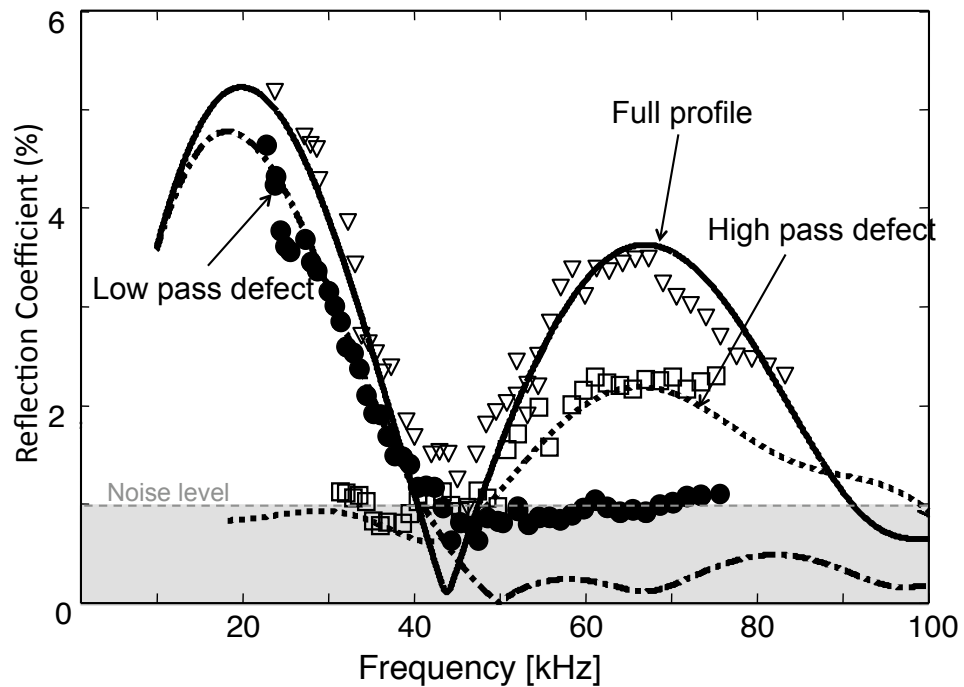
Figure 5.22: *Comparison between the FE predictions of the reflection coefficient spectra from the half ellipsoid defects shown in Fig. 5.21 and experimental results plotted with markers.*

noise level of the experiments.

5.5   Conclusions of a defect diagnosis analysis

In this chapter a qualitative investigation on the correlation between the spatial frequency content of a defect and the temporal frequency content of the reflection coefficient has been presented. This analysis started with the decomposition of a 2D defect in the spatial frequency domain and the effect of its high and low spatial frequency components on the RC spectrum was analyzed in a frequency range from 20 to 100 kHz. The same decomposition approach was then applied to 3D discontinuities such as a half-ellipsoidal defect and real corrosion patches in the same frequency range.

It has been found not only that the superposition of the two matrices reconstructs the original defect profile with a small error, but also that the superposition of the reflections from the two filtered defects gives the reflection spectrum from the full defect profile, within the limit of the validity of the superposition approach. The key finding is that in every defect analyzed (axi-symmetric or 3D), it has been noted that the low pass defect obtained by filtering the full profile in the spatial frequency domain with a low pass filter, gives significant reflection only at low frequencies. In contrast, the high pass defect obtained by the same filtering procedure but with a high pass filter, gives significant reflection only at high frequencies. In the case of a defect with a sharp change in depth within a small region around the circumference of the pipe surrounded by a general corrosion area, it can be noted that the high pass defect contributes significantly to the maximum peak of the RC, its contribution being higher than 50% of the peak value of the RC. In contrast, in the case of a more gradual corrosion patch such as defect X1 or X2, the high pass defect makes only a very modest contribution to the maximum peak of the reflection coefficient.

A possible way to diagnose from the analysis of the RC spectrum the presence of defects that cannot be sized by the method proposed in chapter 4 has then been proposed. This consists in firstly measuring the circumferential extent of the

corrosion; then, under the assumption that the defect is extended axially as much as circumferentially, the frequency at which the maximum peak of the reflection coefficient occurs can be calculated. If the measured RC spectrum has its maximum peak at about the calculated frequency then the interest is to look at the values of the RC at higher frequencies. If the RC at frequencies higher than the one at which the peak occurs is higher than 50% of the peak, then a sharp change in depth is likely to be present in a generally corroded area. In these circumstances the depth determination method proposed in the chapter 4 is unreliable. This method now needs to be validated and refined on more real corrosion profiles.This procedure is limited by the size of the defect, as shown for the defect X5, since if pits smaller than 8 mm are present, higher RC components occur at frequencies out of the range analyzed. In addition, this qualitative approach to size a discontinuity is based on the assumption that the axial extent is similar to the circumferential extent. The FE results for the half-ellipsoidal case were then validated with empirical measurements.
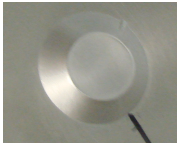
Chapter 6

Conclusions

6.1 Overview of the thesis

In this thesis the effect of the interaction of the fundamental torsional guided wave mode T(0, 1) with complex defects has been analyzed in pipes and a practical method to size remotely the maximum depth of a corrosion patch has been proposed. The motivation for this work comes from the necessity to avoid unscheduled outages in the petrochemical and other industries since the failure of even a minor component can result in the complete shutdown of a facility. Corrosion is a major cause of component failure and its detection and control is a key issue in order to avoid unscheduled downtime in complex industrial systems, the main issue being the estimation of its maximum depth. In Chapter 1 of this thesis a brief overview of the forms of corrosion has been given. The use of ultrasound for the inspection of structures is well established in the NDE field, so a literature review of the past work on the scattering from discontinuities in plates and pipes has been presented. This review showed that very few studies focussed on the analysis of the reflection from real complex shaped scatterers; this thesis aimed therefore to study and understand the effect of a more complex scatterer on the reflection coefficient spectrum in order to identify the main parameters that control it.

It was necessary to understand the way waves propagate in structures before pro-

Figure 6.1: *Summary of the approach used in this thesis to study the effect of complex shaped defects on the reflection of the fundamental torsional mode T(0, 1) in pipes.*

ceeding to analyze more complex scattering phenomena. Chapter 2 introduced the basic principles of ultrasonic wave propagation in media such as plates and pipes. The analogy between guided waves propagating in plates and in pipes has been analyzed and it was applied to a simple case. A brief discussion on the choice of the T(0, 1) guided wave mode and frequency range for inspection has also been given.

The strategy proposed here to understand the influence of a complex feature on the reflection of the T(0, 1) mode is schematically represented in Fig. 6.1. The first step was to consider a complex corrosion defect as a succession of tapered steps with different slopes and lengths, so Chapter 3 of this work focussed on the study of the fundamental torsional guided wave mode T(0, 1) scattering from axi-symmetric tapered up- and down- steps in pipes. The scattering characteristics of these tapers were then used to predict the reflection from tapered notches with different depths and varying slope angles. This preliminary analysis was limited to axi-symmetric defects and therefore addressed the effect of complex profile of the defect in the axial direction.

Both the second and the third steps of Fig. 6.1 were analyzed in Chapter 4, where

the effect of defects with more realistic depth and surface profiles on the reflection of the fundamental torsional mode T(0, 1) in pipes was shown. A numerical study of the reflection of T(0, 1) from three dimensional (3D) defects in pipes with different shapes was carried out. Firstly, simple flat-bottomed defects with different surface profiles were analyzed, and then the reflection from 3D defects with varying depth profile was studied. The influence of the depth profile of a more complex defect in the axial and circumferential directions on the reflection coefficient has also been analyzed.

The results from the above analyses were used to propose a practical approach to determine the maximum depth of a complex discontinuity from the reflection coefficient behaviour. When the defect depth was non-uniform in the circumferential direction (i.e. all cases where the defect was not flat-bottomed), the profile in the circumferential direction was approximated as a V-notch. This method allows the maximum depth of a discontinuity to be estimated from the knowledge of its external circumferential extent and of the peak of the reflection coefficient. It was applied to real corrosion patches and the limitations of the method were determined. It has been found that the presence of a sharp change in depth within a small region around the circumference of the pipe surrounded by a generally corroded area makes this approach unreliable.

This observation led to the development of an approach to diagnose the presence of defects with sharp changes in depth profile in Chapter 5. The idea was to determine whether there is a correlation between the spatial components of a defect and the reflection coefficient spectrum from the defect. This study started with the analysis of a 2D shaped defect decomposed with Fourier transform analysis. This decomposition approach in the spatial frequency domain was then applied to finite 3D defects: firstly ellipsoidal defect and then complex corrosion patches. The results were used to suggest a practical procedure to detect the presence of a problematic defect from the analysis of the RC spectrum.

6.2   Main findings

The main findings of this thesis can be summarized as follows:

- An axi-symmetric step with a linear variation of the depth through the thickness showed that reflections were only generated at the two ends of the taper; there was no evidence of reflections from inside the tapered region. These two reflected waves were out of phase, the phase shift always occurring at the lower thickness end of the taper. The overall reflection coefficient from a tapered step varies periodically as a function of the ratio of the step length to the wavelength.

- Tapered defects are expected to be more difficult to detect at higher inspection frequencies since at a given taper angle, the amplitude of successive reflection coefficient peaks from a tapered defect decreases as the frequency increases. This effect is more evident for shallower tapers.

- There is a linear dependence between the maximum peak of the RC from a simple 3D shaped defect in the frequency domain and the ratio of its equivalent circumferential extent to the total outer circumference of the pipe, at a fixed depth of the discontinuity. This means that the maximum peak of the RC from a 3D scatterer is independent of the shape of the defect.

- The magnitude of the maximum peak of the RC will be not be significantly affected by variation of either the axial extent of the discontinuity or the location of the maximum depth of the defect in the axial and circumferential directions (though the frequency at which the peak occurs will vary).

- The knowledge of the maximum defect circumferential extent and the measurement the maximum of the RC are sufficient to estimate the maximum depth of a random corrosion defect (depth estimation method). The main limitation of the method is on defects whose profile includes a sharp change in an otherwise gradually varying shape.

- A low pass defect obtained by filtering the full profile in the spatial frequency domain with a low pass filter, gives significant reflection only at low frequencies. In contrast, a high pass defect obtained by the same filtering procedure but with a high pass filter, gives significant reflection only at high frequencies.

- It is possible to determine the presence of a problematic defect from the RC spectrum with the following procedure. Firstly, the measurement of the circumferential extent of the defects is required. Then, under the assumption that the defect is extended axially as much as circumferentially, the frequency at which the maximum peak of the reflection coefficient occurs can be calculated. If the measured RC spectrum has its maximum peak at about the calculated frequency then the interest is to look at the values of the RC at higher frequencies. If the RC at frequencies higher than the one at which the peak occurs is higher than about 50% of the peak, then a sharp change in depth is likely to be present in a generally corroded area. In these circumstances the depth determination method is therefore unreliable. This method now needs to be validated and refined on more real corrosion profiles. A limitation of this sizing technique is when small pits are present in a general corroded area as shown for the defect X5 in chapter 5. In this case the presence of the pits is not possible to recognize since the maximum of the RC occurs at frequencies higher than the range analyzed. In addition, this qualitative approach to size a discontinuity is based on the assumption that the axial extent is similar to the circumferential extent which is not always valid.

The whole study presented in this thesis suggests that a range of frequency wider than the one usually applied in long range inspection is required in order to employ guided waves for defect sizing, and in particular to detect the maximum depth of the discontinuity. It is possible to estimate the depth of a scatterer with a gradual variation through the thickness by looking at its peak reflection at low frequencies. As mentioned above, this is because at a given taper angle and especially for shallower tapers, the amplitude of the successive reflections from the tapered part of the defect decreases as the frequency increases. In addition, the sharp edges of a cor-

rosion patch affect the RC significantly only at high frequencies (frequencies higher than 100 kHz if the the axial extent of the defect is smaller than 8 mm).

6.3   Suggestions for future work

As mentioned above, the method proposed to size the maximum depth of a corrosion patch is based on the knowledge of the maximum peak of the reflection coefficient from the scatterer and the measurement of its external circumferential extent. The maximum peak of the reflection from a feature can easily be measured with current commercial equipment [7]; therefore in order to complete this analysis a practical method to estimate accurately the circumferential extent of corrosion patches is required. Davies *et al* [98] proposed a method for circumferential sizing of a defect from the image obtained with focussing techniques. This works if the circumferential extent of the scatterer is bigger than 1.5λ, meaning that the estimation of the external circumferential extent is simple when it is large but becomes progressively more difficult when the circumferential extent drops towards the wavelength used. This is the subject of a current research at University of Bristol and funded by the same overall project [59].

Once the circumferential extent is estimated, the depth estimation method can be employed to size the maximum depth of a gradual corrosion patch. However, it is necessary still to adapt the method to deal with all the problematic corrosion patches. A first step on the diagnosis of these problematic defects has been proposed in the last chapter of this thesis where a sharp change in depth can be detected by looking at the reflection coefficient behaviour at high frequencies, however more work is required to have a full understanding of the phenomenon. This requires the method to be applied to much more real corrosion samples and to be refined accordingly. It will then be necessary to develop a method for sizing the problematic defects.

References

[1] J. M. Galbraith and G. C. Williamson. Practical considerations for users of guided wave ultrasonic testing. *NACE International*, 07164, 2008.

[2] J. R. Davies. *Corrosion: Understanding the basics*. ASM International, 2000.

[3] P. Barham, B. Brown, T. Beuker, and M. Fingerhut. Pipeline integrity analysis based on interdisciplinary cooperation. *Pigging Product and Service Association*, 2005.

[4] S. Cohn. Alaska pipeline problem signals failure oil shortages, http://www.cnbc.com, 11 January 2011.

[5] G. Engelhardt and D. D. Macdonald. Deterministic prediction of pit depth distribution. *Journal of Corrosion NACA*, 54(6):469–479, 1998.

[6] D. N. Alleyne and P. Cawley. The interaction of lamb waves with defects. *IEEE Transactions on Ultrasonics, Ferroelectrics, and Frequency control*, 39(3):381, 1992.

[7] http://www.guided-ultrasonics.com (date last viewed 09/07/2011).

[8] S. D. Henry and W. W. Jr Scoot. *Corrosion in the petrolchemical industry*. ASM International, 1994.

[9] M. G. Fontana and N. D. Greene. *Corrosion Engineering*. McGraw Hill, 1967.

[10] H. H. Uhlig. *Corrosion and corrosion control*. John Wiley & Sons, 1963.

[11] U. R. Evans. *The corrosion and oxidation of metals.* Edward Arnold Ltd., 1960.

[12] J. Britton. Corrosion at pipe supports: Causes and solutions. Technical report, Deepwater Corrosion Services, 2002.

[13] N. G. Thompson. Gas and liquid transmission pipelines. Technical report, CC Technologies, 2006.

[14] Y. Cho. A boundary element solution for a mode conversion study on the edge reflection of lamb waves. *The Journal of the Acoustical Society of America*, 99:2097, 1996.

[15] Y. Cho, D. D. Hongchrholt, and J. L. Rose. Lamb wave scattering analysis for reflector characterization. *IEEE Transactions on Ultrasonics, Ferroelectrics, and Frequency Control*, 44(1):44, 1997.

[16] T. Hayashi and K. Kawashima. Multiple reflections of lamb waves at a delamination. *Ultrasonics*, 40(1-8):193, 2002.

[17] M. Koshiba, S. Karakida, and M. Suzuki. Finite-element analysis of lamb wave scattering in an elastic plate waveguide. *IEEE transactions on sonics and ultrasonics*, 31(1):18, 1984.

[18] E. Le Clézio, M. Castaings, and B. Hosten. The interaction of the S0 lamb mode with vertical cracks in an aluminium plate. *Ultrasonics*, 40(1-8):187, 2002.

[19] S. Rokhlin. Diffraction of lamb waves by a finite crack in an elastic layer. *The Journal of the Acoustical Society of America*, 67:1157, 1980.

[20] S. I. Rokhlin. Resonance phenomena of lamb waves scattering by a finite crack in a solid layer. *The Journal of the Acoustical Society of America*, 69:922, 1981.

[21] O. Diligent, T. Grahn, A. Bostrom, P. Cawley, and M. J. S Lowe. The low-frequency reflection and scattering of the S Lamb mode from a circular through-thickness hole in a plate: Finite element, analytical and experimental studies. *The Journal of the Acoustical Society of America*, 112:2589, 2002.

[22] T. Grahn. Lamb wave scattering from a circular partly through-thickness hole in a plate. *Wave Motion*, 37(1):63, 2003.

[23] O. Diligent and M. J. S Lowe. Reflection of the s lamb mode from a flat bottom circular hole. *The Journal of the Acoustical Society of America*, 118:2869, 2005.

[24] C. M. Fortunko and R. B. King. Nondestructive evaluation of planar defects in plates using low-frequency shear horizontal waves. *Journal of Applied Physics*, 53:3450, 1982.

[25] A. Demma, P. Cawley, and M. J. S Lowe. Scattering of the fundamental shear horizontal mode from steps and notches in plates. *The Journal of the Acoustical Society of America*, 113:1880, 2003.

[26] P. Rajagopal and M. J. S Lowe. Short range scattering of the fundamental shear horizontal guided wave mode normally incident at a through-thickness crack in an isotropic plate. *The Journal of the Acoustical Society of America*, 122:1527, 2007.

[27] X. G. Zhao and J. L. Rose. Boundary element modeling for defect characterization potential in a wave guide. *International Journal of Solids and Structures*, 40(11):2645, 2003.

[28] M. Koshiba, K. Hasegawa, and M. Suzuki. Finite-element solution of horizontally polarized shear wave scattering in an elastic plate. *IEEE Transactions on Ultrasonics, Ferroelectrics, and Frequency Control*, 34(4):461, 1987.

[29] H. E. Engan. Torsional wave scattering from a diameter step in a rod. *The Journal of the Acoustical Society of America*, 104:2015, 1998.

[30] A. Demma, P. Cawley, and M. J. S Lowe. The reflection of the fundamental torsional mode from cracks and notches in pipes. *The Journal of the Acoustical Society of America*, 114:611, 2003.

[31] W. Luo. A guided wave plate experiment for a pipe. *Journal of Pressure Vessel Technology*, 127:345, 2005.

[32] W. Zhu. An FEM simulation for guided elastic wave generation and reflection in hollow cylinders with corrosion defects. *Journal of Pressure Vessel Technology*, 124:108, 2002.

[33] D. N. Alleyne, M. J. S. Lowe, and P. Cawley. The reflection of guided waves from circumferential notches in pipes. *Journal of Applied Mechanics*, 65:635, 1998.

[34] D. N. Alleyne, B. Pavlakovic, M. J. S Lowe, and P. Cawley. Rapid, long range inspection of chemical plant pipework using guided waves. *Insight*, 43:93–96, 101, 2001.

[35] H. Bai, A. H. Shah, N. Popplewell, and S. K. Datta. Scattering of guided waves by circumferential cracks in steel pipes. *Journal of Applied Mechanics*, 68:619, 2001.

[36] P. Cawley, M. J. S Lowe, F. Simonetti, C. Chevalier, and A. G. Roosenbrand. The variation of the reflection coefficient of extensional guided waves in pipes from defects as a function of defect depth, axial extent, circumferential extent and frequency. In *Proceedings of the Institution of Mechanical Engineers; Part B; Journal of Engineering Manufacture*, volume 216, page 1131, 2002.

[37] A. Demma, P. Cawley, M. J. S Lowe, A. G. Roosenbrand, and Pavlakovic B. The reflection of guided waves from notches in pipes: a guide for interpreting corrosion measurements. *NDT & E international*, 37(3):167, 2004.

[38] J. J. Ditri. Utilization of guided elastic waves for the characterization of circumferential cracks in hollow cylinders. *The Journal of the Acoustical Society of America*, 96:3769, 1994.

[39] H. Kwun. Magnetostrictive generation and detection of longitudinal, torsional, and flexural waves in a steel rod. *The Journal of the Acoustical Society of America*, 96:1202, 1994.

[40] Z. Liu, C. He, B. Wu, X. Wang, and S. Yang. Circumferential and longitudinal defect detection using T (0, 1) mode excited by thickness shear mode piezoelectric elements. *Ultrasonics*, 44:1135, 2006.

[41] M. J. S Lowe. Characteristics of the reflection of lamb waves from defects in plates and pipes. In D. Chimenti and D. Thompson, editors, *Review of Progress in Quantitative Nondestructive Evaluation*, volume 17, New York, 1998. Plenum.

[42] M. J. S. Lowe, D. N. Alleyne, and P. Cawley. The mode conversion of a guided wave by a part-circumferential notch in a pipe. *Journal of Applied Mechanics*, 65:649, 1998.

[43] M. J. S. Lowe, D. N. Alleyne, and P. Cawley. Defect detection in pipes using guided waves. *Ultrasonics*, 36(1-5):147, 1998.

[44] W. Mohr and P. Holler. On inspection of thin-walled tubes for transverse and longitudinal flaws by guided ultrasonic waves. *IEEE Transactions on Sonics and Ultrasonics*, 23(5):369, 1976.

[45] J. L. Rose. A baseline and vision of ultrasonic guided wave inspection potential. *Journal of Pressure Vessel Technology*, 124:273, 2002.

[46] M. G. Silk and K. F. Bainton. The propagation in metal tubing of ultrasonics wave modes equivalent to lamb waves. *Ultrasonics*, 71(1):11, 1979. 0041-624X.

[47] W. Zhuang, A. H. Shah, and S. K. Datta. Axisymmetric guided wave scattering by cracks in welded steel pipes. *Journal of Pressure Vessel Technology*, 119:401, 1997.

[48] W. Zhu, J. L. Rose, J. N. Barshinger, and V. S. Agarwala. Ultrasonic guided wave NDT for hidden corrosion detection. *Research in Nondestructive Evaluation*, 10(4):205, 1998.

[49] J. M. Arnold and L. B. Felsen. Intrinsic modes in a nonseparable ocean waveguide. *The Journal of the Acoustical Society of America*, 76:850, 1984.

[50] P. Marical, M. Ech-Cherif El-Kettani, and M. V. Predoi. Experimental and numerical studies on lamb waves conversion in a waveguide with gaussian section variation. In *International Ultrasonics Symposium,*, pages 1185–1188, Vancouver, Canada, 2006. IEEE.

[51] P. Marical. Guided waves in elastic plates with gaussian section variation: Experimental and numerical results. *Ultrasonics*, 47(1-4):1, 2007.

[52] Z. Hamitouche, M. Ech-Cherif El-Kettani, J.-L. Izbicki, and H. Dhelouah. Multi-resonances of the S0 adiabatic mode propagating in a linear varying cross section waveguide, experimental and numerical results. In *IEEE International Symposium*, pages 2303–2306, New York, 2007.

[53] M. Ech-Cherif El-Kettani, P. Marical, and Z. Hamitouche. Inverse problem for the geometry profile determination of waveguides with varying section using adiabatic behaviour of guided waves. *IEEE Transactions on Sonics and Ultrasonics*, 56(9):2023–2026, 2009.

[54] J. Ma and P. Cawley. Low-frequency pulse echo reflection of the fundamental shear horizontal mode from part-thickness elliptical defects in plates. *Journal of the Acoustical Sociey of America*, 127(6):3485–3493, 2010.

[55] P. J. Schafbuch, R. B. Thompson, and F. J. Rizzo. Elastic scatterer interaction via generalized born series and far-field approximations. *Journal of the Acoustical Sociey of America*, 93(295-307), 1993.

[56] M. Grøvlen, E. Bardal, S. Berge, O. Eide, K. Engesvik, P. J. Haagensen, and O. Ørjasaether. Localized corrosion on offshore tubular structures: inspection and repair criteria. In *Proceedings of Offshore Technology Conference, 1-4 May 1989, Houston, Texas*, pages 277–288, 1989.

[57] E. Domany, O. Entin-Wohlman, and L. Mizrachi. Multiple scattering formalism: Application to scattering by two spheres. *Journal of Applied Physics*, 56:132–136, 1984.

[58] J. E. Gubernatis, E. Domany, and J. A. Krumhansl. Formal aspects of the theory of the scattering of ultrasound by flaws in elastic materials. *Journal of Applied Physics*, 48(7):2804–2811, 1977.

[59] L. Moreau, M. Caleap, and A. Velichko. Scattering of guided waves by through-thickness cavities with irregular shapes. *Wave Motion*, 48:586–602, 2011.

[60] A. Løvstad and P. Cawley. The reflection of the fundamental torsional guided wave from multiple circular holes in pipes. *NDT & E international*, 44(7):553–562, 2011.

[61] L. Rayleight. On the free vibrations of an infinite plate of homogeneous isotropic elastic matter. In *Proceedings London Mathematical Society*, volume 20, pages 225–237, 1888-1889.

[62] H. Lamb. On waves in an elastic plate. In *Proceedings Royal Society*, volume 93, pages 114–128, 1916-1917.

[63] K. F. Graff. *Wave motion in elastic solids*. Clerendon Press, Oxford, 1975.

[64] B. A. Auld. *Acoustic Fields and Waves in Solids*, volume 1. Krieger Publishing Company, Malabar, Florida, 1990.

[65] J. L. Rose. *Ultrasonic waves in solid media*. Cambridge University Press, Cambridge, UK, 1999.

[66] J. D. Achenback. *Wave propagation in elastic solids*. North-Holland Publishing Company, Amsterdam, 1984.

[67] B. A. Auld. *Acoustic fields and waves in solids*, volume 2. Krieger Publishing Company, Malabar, Florida, second edition, 1990.

[68] D. N. Alleyne and P. Cawley. Long range propagation of lamb waves in chemical plant pipework. *Materials Evaluation*, 55:504–508, 1997.

[69] B. Pavlakovic, M. J. S. Lowe, D. N. Alleyne, and P. Cawley. Disperse: A general purpose program for creating dispersion curves. In D. Chimenti

and D. Thompson, editors, *Review of Progress in Quantitative Nondestructive Evaluation*, New York, 1997. Plenum.

[70] M. J. S Lowe. Matrix techniques for modelling ultrasonic waves in layered media. *IEEE Transactions on Ferroelectronic Frequency Control*, 2(4):525–542, 1995.

[71] A. Demma. *Interaction of guided waves with discontinuities in structures*. PhD thesis, 2003.

[72] D. C. Gazis. Three dimensional investigation of propagation of waves in hollow circular cylinders. *Journal of the Acoustical Sociey of America*, 31(5):568–578, 1959.

[73] I. Mirsky. Wave propagation in transversely isotropic circular cylinders, part 1: Theory. *Journal of the Acoustical Sociey of America*, 37(6):1016–1021, 1965.

[74] J. Zemanek. An experimenta and theoretical investigation of elastic wave propagation in a cylinder. *Journal of the Acoustical Sociey of America*, 51(1):265–283, 1972.

[75] M.C. Pochhammer. Uber die fortpflanzungsgeschwindigkeiten kleiner schwingungen in einem unbegrenzten isotropen kreiszylinder. *J. ur die reine und angewandte mathematik*, 81:324–336, 1876.

[76] C. Chree. The equations of an isotropic elastic solid in polar and cylindrical coordinates, their solution and applications. *Transactions of the Cambridge Philosophical Society*, 14:250–369, 1889.

[77] A. H. Fitch. Observation of elastic-pulse propagation in axially symmetric and nonaxially symmetric longitudinal modes of hollow cylinders. *Journal of the Acoustical Sociey of America*, 35(5):706–708, 1963.

[78] B. N. Pavlakovic. *Leaky guided ultrasonic waves in NDT*. PhD thesis, 1998.

[79] H. Nishino, S. Takashima, F. Uchida, M. Takemoto, and K. Ono. Modal analysis of hollow cylindrical guided waves and applications. *Japanese Journal of Applied Physics*, 40:364–370, 2001.

[80] J. Li and J. Rose. Natural beam focusing of non-symmetric guided waves in large diameter pipes. *Ultrasonics*, 44:35–45, 2006.

[81] A. Velichko and P. D. Wilcox. Excitation and scattering of guided waves: relationships between solutions for plates and pipes. *Journal of the Acoustical Sociey of America*, 125(6):3623–3631, 2009.

[82] F. B. Cegla, A. Rohde, and M. Veidt. Analytical prediction and experimental measurement for mode conversion and scattering of plate waves at non-symmetric circular blind holes in isotropic plates. *Wave Motion*, 45:168–177, 2007.

[83] P. D. Wilcox, R. P. Dalton, M. J. S Lowe, and P. Cawley. Mode and trasducer selection for long range lamb wave inspection. *Key Engineering Materials Proc. DAMAS*, 34:152–161, 1999.

[84] P. D. Wilcox, M. J. S Lowe, and P. Cawley. A signal processing technique to remove the effect of dispersion from guided wave signals. In D. Chimenti and D. Thompson, editors, *Review of Progress in Quantitative Nondestructive Evaluation*, New York, 2001. Plenum.

[85] R. Sinclair, J. Goyette, and D. Zellouf. A numerical dispersion compensation technique for time recompression of lamb wave signals. *Ultrasonics*, 40:727–732, 2002.

[86] D. N. Alleyne and P. Cawley. The long range detection of corrosion in pipes using lamb waves. In D. Chimenti and D. Thompson, editors, *Review of Progress in Quantitative Nondestructive Evaluation*, volume 14, New York, 1994. Plenum.

[87] P. D. Wilcox, M. J. S Lowe, and P. Cawley. Long range lamb wave inspection: The effect of dispersion and modal sensitivity. In D. Chimenti and D. Thompson, editors, *Review of Progress in Quantitative Nondestructive Evaluation*, volume 18, New York, 1999. Plenum.

[88] P. J. Mudge. Field application of the teletest (r) long-range ultrasonic testing. *Insight*, 43:74–77, 2001.

[89] J. Barshinger, J. L. Rose, and Jr. M. J. Avioli. Guided wave resonance tuning for pipe inspection. *Journal of Pressure Vessel Technology*, 124:303–310, 2002.

[90] Y. Y. Kim, C. I. Park, S. H. Cho, and S. W. Han. Torsional wave experiments with a new magnetostrictive transducer configuration. *Journal of the Acoustical Sociey of America*, 117(6):3459–3468, 2005.

[91] J. Li and J. L. Rose. Excitation and propagation of non-axi-symmetric guided waves in a hollow cylinder. *Journal of the Acoustical Sociey of America*, 109(2):457–464, 2001.

[92] J. Li and J. L. Rose. Angular-profile tuning of guided waves in hollow cylinders using a circumferential pahsed array. *IEEE Transactions on Ferroelectronic Frequency Control*, 49(12):1720–1729, 2002.

[93] J. Li. On circumferential disposition of pipe defects by long-range ultrasonic guided waves. *Journal of Pressure Vessel Technology*, 127:530–537, 2005.

[94] P. D. Corl, P. M. Grant, and G. S. Kino. A digital synthetic focus acoustic imaging system for NDE. In *Proceedings of the 1978 Ultrasonics Symposium*, pages 263–268, 1978.

[95] M. Karaman, P. C. Li, and M. O' Donnell. Synthetic aperture imaging for small scale systems. *IEEE Transactions on Ferroelectronic Frequency Control*, 42(3):429–442, 1995.

[96] J. T. Ylitalo and H. Ermet. Ultrasound synthetic aperture imaging: Monostatic approach. *IEEE Transactions on Ferroelectronic Frequency Control*, 41(3):333–339, 1994.

[97] J. O. Davies. *Inspection of pipes using low frequency focused guided waves*. PhD thesis, 2008.

[98] J. Davies and P. Cawley. The application of the syntethic focussing for imaging crack-like defcts in pipelines using guided waves. *IEEE Transactions on Ultrasonics, Ferroelectrics, and Frequency Control*, 56:759–771, 2009.

[99] F. Simonetti. Lamb wave propagation in elastic plates coated with viscoelastic materials. *Journal of the Acoustical Sociey of America*, 115(5):2041–2053, 2004.

[100] D. N. Alleyne, B. Pavlakovic, M. J. S. Lowe, and P. Cawley. The use of guided waves for rapid screening of chemical plant pipework. *Journal of the Korean Society for Nondestructive Testing*, 22(6):589–598, 2002.

[101] G. Kino. *Acoustic waves: Devices, imaging and analogue signal processing.* Prentice-Hall, 1987.

[102] M. J. S. Lowe. Low-frequency reflection characteristics of the s lamb wave from a rectangular notch in a plate. *The Journal of the Acoustical Society of America*, 111:64, 2002.

[103] M. J. S. Lowe. The low frequency reflection characteristics of the fundamental antisymmetric lamb wave a from a rectangular notch in a plate. *The Journal of the Acoustical Society of America*, 112:2612, 2002.

[104] J. E. Gubernatis, E. Domany, J. A. Krumhansl, and M. Humberman. The born approximation in the theory of the scattering of elastic waves by flaws. *Journal of Applied Physics*, 48:2812–2819, 1977.

[105] P. J. Shcafbuch, R. B. Thompson, and F. J. Rizzo. Elastic scatterer interaction via generalized born series and far-eld approximations. *Journal of the Acoustical Sociey of America*, 93(1):295–307, 1993.

[106] J. H. Rose and J. M. Richardson. Time domain born approximation. *Journal of Nondestructive Evaluation*, 3(1):45–53, 1982.

[107] J. M. Baik and R. B. Thompson. Ultrasonic scattering from imperfect interfaces: A quasi-static model. *Journal of Nondestructive Evaluation*, 4(3/4):177–196, 1984.

[108] F. J. Margetan, R. B. Thompson, and T. A. Gray. Interfacial spring model for ultrasonic interactions with imperfect interfaces: Theory of oblique incidence and application to diffusion-bonded butt joints. *Journal of Nondestructive Evaluation*, 7(3/4):131–152, 1988.

[109] A. Sedov and L. W. Schmerr Jr. The time domain elastodynamic kirchhoff approximation for cracks: The inverse problem. *Wave Motion*, 8:15–26, 1986.

[110] A. Sedov and L. W. Schmerr Jr. Pulse distortion and the elastodynamic kirchhoff approximation for cracks: the direct and inverse problems. *Journal of Applied Mechanics*, 47(6):1201–1215, 1987.

[111] J. D. Achenbach, A. K. Gautesen, and H. McMaken. *Ray methods for waves in elastic solids*. Pitman books Ltd., 1982.

[112] P. Rajagopal. *Towards higher resolution guided wave inspection: Scattering studies*. PhD thesis, 2008.

[113] www.simulia.com. Abaqus version .6.7 user manual, 2008.

[114] www.simulia.com. Abaqus version 6.9 user's manual. 2010.

[115] M. B. Drozdz. *Efficient nite element model ling of ultrasound waves in elastic media*. PhD thesis, 2007.

[116] D. N. Alleyne and P. Cawley. A two-dimensional fourier transform method for the measurement of propagating multimode signals. *Journal of the Acoustical Sociey of America*, 89(3):1168–1168, 1991.

[117] F. Moser, L. J. Jacobs, and J. Qu. Modeling elastic wave propagation in waveguides with the nite element method. *NDT & E international*, 32:225–234, 1999.

[118] A. Demma, P. Cawley, M. J. S Lowe, and B. Pavlakovic. The effect of bends on the propagation of guided waves in pipes. *Journal of pressure vessel technology*, 127:328, 2005. 0094-9930.

[119] S. D. Cramer and B. S. Covino. *ASM Handbook, Volume 13A - Corrosion: Fundamentals, Testing, and Protection.* 2003.

[120] R. Nyborg. Initiation and growth of mesa corrosion attach during CO2 corrosion of carbon steel. *NACE International*, 1998.

[121] J. Kvarekval. Morphology of localized corrosion attacks in sour enviroments. *NACE International*, (paper 07659), 2007.

[122] http://www.vsonomatic.com (date last viewed 09/07/2011).

[123] E. N. Codaro, R. Z. Nakazato, A. L. Horovistiz, L. M. F. Ribeiro, R. B. Ribeiro, and L. R. O. Hein. An image processing method for morphology characterization and pitting corrosion evaluation. *Material Science and Engineering*, 334(1-2):298– 306, 2002.

[124] R. E. Melchers. Pitting corrosion of mild steel in marine immersion enviroment- part 1: Maximum pit depth. *Corrosion*, 60:824–836, 2004.

[125] R. Carandente, J. Ma, and P. Cawley. The scattering of the fundamental torsional mode from axi-symmetric defects with varying depth profile in pipes. *Journal of the Acoustical Sociey of America*, 127(4):3440–3448, 2010.

[126] D. E. Newland. *An introduction to random vibrations, spectral and wavelet analysis.* Dover Publications Inc, Mineola, New York.

[127] R. V. Churcill. *Fourier series and boundary values problems.* McGraw-Hill, New York, 1941.

[128] J. W. Cooley and J. W. Tukey. An algorithm for the machine computation of the complex fourier series. *Mathematics of Computation*, 19:297–301, 1965.

[129] http://http://www.rhino3d.com (date last viewed 28/09/2011).

[130] A. Valor, F. Caleyo, L. Alfonso, D. Rivas, and J. M. Hallen. Stochastic modeling of pitting corrosion: A new model for initiation and growth of multiple corrosion pits. *Corrosion Science*, 49:559–579, 2007.

[131] A. C. Kak and M. Slaney. *Principle of computerized tomographic imaging*, volume 33 of *Classic in Applied Mathematics*. Society for industrial and applied mathematics, Philadelphia, 2001.

[132] M. Yamada, K. Murakami, K. Nakahata, and M. Kitaharata. Three dimensional born and kirchoff inversions for shape reconstruction of defects. In D. Chimenti and D. Thompson, editors, *Review of Progress in Quantitative Nondestructive Evaluation*, volume 22, New York, 2003. Plenum.

[133] D. L. Jain and R. P. Kanwal. The born approximation for the scattering theory of elastic waves by two dimensional flaws. *Journal of Applied Physics*, 53(6):4208–4217, 1982.

[134] M. Slaney, A. C. Kak, and L. E. Larsen. Limitation of imaging with first-order diffraction tomography. *IEEE Transactions on Microwave Theory and Techniques*, 32(8):861–874, 1984.

[135] F. Simonetti. Multiple scattering: The key to unravel the subwavelength world from the far-field pattern of a scattered wave. *Physical Review E*, 73:036619, Mar 2006.

List of Publications

[P1] R. Carandente, J. Ma and P. Cawley, "The reflection of the fundamental torsional mode from axi-symmetric defects with varying profiles in pipes", in *Review of Progress in Quantitative Nondestructive Evaluation*, Kingston, Rhode Island. Edited by D. Chimenti, B. Thompson, 2010.

[P2] R. Carandente, J Ma and P. Cawley, "The scattering of the fundamental torsional mode from axi-symmetric defects with varying profiles in pipes", *Journal of the Acoustical Society of America*, Volume 127, Issue 6, pp.2808–2817, 2010.

[P3] R. Carandente and P. Cawley, "The effect of complex defect profiles on the reflection of guided waves in pipes", in *Review of Progress in Quantitative Nondestructive Evaluation*, San Diego, California, 2011. In press.

[P4] R. Carandente and P. Cawley, "The effect of complex defect profiles on the reflection of the fundamental torsional mode in pipes", *NDT&E International*, Volume 46, pp.4147, 2012.

[P5] R. Carandente, P. Cawley, and M. J. Lowe "Guided wave testing of pipes: the influence of the shape of corrosion defects on the reflected signals", in 5th *Pan American Conference for NDT*, 2-6 October 2011, Cancun, Mexico.

[P6] R. Carandente, and P. Cawley, "A method to estimate the size of corrosion patches with guided waves", in *Review of Progress in Quantitative Nondestructive Evaluation*, Burlington, Vermont, 2011. In press.

[P7] R. Carandente, A. Løvstad and P. Cawley, "The influence of sharp edges in corrosion profiles on the reflection of guided waves.", *NDT&E International*, submitted January 2012.